Dissertation

submitted to the
Combined Faculties for the Natural Sciences and for Mathematics
of the Ruperto-Carola University of Heidelberg, Germany

for the degree of
Doctor of Natural Sciences

Put forward by
M.Sc. Hannes Helmut Bauser
born in Heilbronn-Neckargartach

Oral examination: June 11, 2018

Knowledge Fusion in Soil Hydrology

Referees:

Prof. Dr. Kurt Roth
Prof. Dr. Carsten Rother

Knowledge Fusion in Soil Hydrology: The mathematical representation of soil water movement exhibits uncertainties in all model components. Data assimilation methods, like the ensemble Kalman filter (EnKF), combine models and measurements into an improved representation and can – at least in principle – account for all uncertainties. However, a proper description of the uncertainties is required, which is particularly difficult in soil hydrology, where model errors typically vary rapidly in space and time. Inflation methods can account for unrepresented model errors. To improve the EnKF performance, I designed an inflation method specifically for soil hydrology, that is capable of adjusting inflation factors to spatiotemporally varying model errors. For the application on a real-world case, I assessed the key uncertainties for the specific hydraulic situation of a 1-D soil profile with TDR (time domain reflectometry)-measured water contents. With the EnKF, I directly represented and reduced all key uncertainties (initial condition, soil hydraulic parameters, small-scale heterogeneity, and upper boundary condition), except for an intermittent violation of the local equilibrium assumption by the Richards equation. To bridge this time, I introduced a closed-eye period, which ensures constant parameters and improves the EnKF towards the goal of knowledge fusion – the consistent aggregation of all information pertinent to some observed reality.

Knowledge Fusion in der Bodenhydrologie: Die mathematische Darstellung der Bodenwasserbewegung weist Unsicherheiten in allen Modellkomponenten auf. Datenassimilationsmethoden, wie der Ensemble Kalman Filter (EnKF), verbinden Modelle und Messungen zu einer verbesserten Darstellung und können dabei grundsätzlich alle Unsicherheiten berücksichtigen. Allerdings ist eine korrekte Charakterisierung dieser Unsicherheiten erforderlich, was insbesondere in der Bodenhydrologie herausfordernd ist, da sich Modellfehler in der Regel schnell in Raum und Zeit ändern. *Inflation*-Methoden können nicht dargestellte Modellfehler ausgleichen. Um den EnKF zu verbessern, entwickelte ich speziell für die Bodenhydrologie eine *Inflation*-Methode, welche in der Lage ist, *Inflation*-Faktoren an die in Raum und Zeit variierenden Modellfehler anzupassen. Für die Anwendung in einem realen Fall ermittelte ich die Hauptunsicherheiten für die spezifische hydraulische Situation eines 1-D Bodenprofils mit TDR (Time Domain Reflectometry)-gemessenen Wassergehalten. Mit dem EnKF berücksichtigte und reduzierte ich alle Hauptunsicherheiten (Ausgangszustand, bodenhydraulische Parameter, kleinskalige Heterogenität und obere Randbedingung), außer einer zwischenzeitlichen Verletzung der lokalen Gleichgewichtsannahme der Richards-Gleichung. Um diese Zeit zu überbrücken, führte ich einen closed-eye Zeitraum ein. Dieser sorgt für konstante Parameter und verbessert den EnKF hin zu Knowledge Fusion – der konsistenten Zusammenführung aller für eine beobachtete Realität relevanten Informationen.

Contents

1 Introduction 1

2 Soil water movement 3
- 2.1 Dynamics . . . 3
- 2.2 Subscale physics . . . 6
- 2.3 Superscale physics . . . 8
- 2.4 Response . . . 10

3 Ensemble Kalman filter 11
- 3.1 Conceptual overview . . . 11
- 3.2 Kalman filter . . . 13
- 3.3 Ensemble Kalman filter . . . 15
- 3.4 Localization . . . 18
- 3.5 Inflation . . . 19
- 3.6 EnKF in hydrology . . . 22

4 Inflation for soil hydrology 25
- 4.1 Method . . . 26
- 4.2 Results . . . 29
- 4.3 Summary and discussion . . . 33

5 Application 37
- 5.1 Test site . . . 37
- 5.2 Representation . . . 38
- 5.3 EnKF settings . . . 41
- 5.4 Results . . . 45
- 5.5 Summary and discussion . . . 61

6 Summary and outlook 63

A Derivations and calculations 65
- A.1 Analysis equations in the Kalman filter . . . 65
- A.2 Jacobian matrix in the inflation method . . . 67

Acknowledgments **69**

Bibliography of own publications **71**

References **73**

1 | Introduction

In parts based on *Bauser et al.* [2016] and *Bauser et al.* [2018].

Soils are at the interface of hydrosphere, biosphere, atmosphere, and lithosphere and are a key component to all ecosystem services for humankind (provisioning, regulating, cultural, and supporting services) [*Adhikari and Hartemink*, 2016]. The services provided by soils are controlled by interlinked basic biological, chemical, and physical processes. One of these processes is soil water movement [*Dominati et al.*, 2010; *Vereecken et al.*, 2016]. It is a key process in several provisioning and regulating ecosystem services, such as biomass production, fresh water retention, climate regulation, or water buffering and filtering.

Current research questions concerning these ecosystem services range from more efficient water usage and increased crop yield [e.g., *Silber et al.*, 2015] and the prediction of fertilizer leaching into groundwater [e.g., *Baram et al.*, 2016] in agriculture to the feedback of soil moisture and precipitation in the context of climate change [e.g., *May et al.*, 2017]. They all rely on a proper description of the underlying soil hydrologic processes.

The description of soil water movement with a mathematical model requires knowledge of material properties (typically characterized by soil hydraulic parameters), initial conditions, and boundary conditions. Soil hydraulic parameters are especially difficult to determine, since they can neither be measured directly nor transferred directly from the laboratory to the field.

Soil hydraulic parameters have been estimated inversely based on measurements of the temporal development of the hydraulic state [e.g., *Hopmans et al.*, 2002; *Vrugt et al.*, 2008]. Inverse methods are based on the assumption of a perfect model and incorporate all errors and uncertainties into the estimated parameters, leading to a suboptimal estimation.

In contrast, data assimilation methods are capable of combining information from uncertain measurements and uncertain models into an optimal estimate of the geophysical field of interest, but depend on the correct description of the corresponding uncertainties [*Reichle*, 2008]. Data assimilation methods have applications in all branches of the geosciences, with weather forecasting as the driving force behind many recent advances [*van Leeuwen et al.*, 2015]. Nonlinear data assimilation methods include variational methods, particle filters, and ensemble Kalman filters (EnKF). The EnKF [*Evensen*, 1994; *Burgers et al.*, 1998] is a popular data assimilation method due to its simple conceptional formulation and ease of implementation [*Evensen*, 2003].

In hydrology, the EnKF was used for soil moisture estimation from satellite data [e.g. *Reichle et al.*, 2002; *Crow and Van Loon*, 2006] or from local measurements [e.g. *De Lannoy et al.*, 2007, 2009; *Camporese et al.*, 2009]. However, including material properties into the estimation can be crucial in hydrology. *Liu and Gupta* [2007] called for an integrated assimilation framework including not only states but parameters, and even model structure.

Moradkhani et al. [2005] used a dual EnKF approach, whereas *Vrugt et al.* [2005] combined an EnKF and the shuffled complex evolution metropolis algorithm in an iterative way, to estimate parameters and states in a rainfall–runoff model. The joint assimilation of states and parameters in an augmented state was successfully performed in groundwater research [e.g. *Chen and Zhang*, 2006; *Hendricks Franssen and Kinzelbach*, 2008; *Kurtz et al.*, 2012, 2014; *Erdal and Cirpka*, 2016], but also in soil hydrology for land surface models [e.g. *Bateni and Entekhabi*, 2012; *Han et al.*, 2014; *Zhang et al.*, 2017] and on smaller scales based on the Richards equation [e.g. *Li and Ren*, 2011; *Wu and Margulis*, 2011, 2013; *Song et al.*, 2014; *Erdal et al.*, 2014, 2015; *Shi et al.*, 2015; *Brandhorst et al.*, 2017; *Botto et al.*, 2018].

The studies based on the Richards equation are, except for *Botto et al.* [2018], either purely synthetic cases, or with a focus on synthetic cases. This offers the advantage of a direct control and knowledge about all uncertainties. The characterization of uncertainties is critical for the success of a data assimilation scheme [*Liu et al.*, 2012]. Un- or ill-represented processes are typical in soil hydrology and can cause spatially and temporally varying model errors. Inflation methods can account for unrepresented model errors. However, these methods are developed in an atmospheric sciences context and their transfer to soil hydrology is not trivial. Consequently, data assimilation applications to real-world cases in hydrology remain challenging.

This work focuses on the representation of uncertainties in soil hydrology within an EnKF framework with the goal of knowledge fusion – the consistent aggregation of all information pertinent to some observed reality. Therefore, I developed an inflation method for the specific needs in soil hydrology, where it is able to operate with joint state and parameter estimation and spatiotemporally varying model errors typical for hydrology. Next, I applied the EnKF to a small real-world example. For this specific case, all uncertainties are assessed qualitatively. Whenever it is possible, the relevant uncertainties are represented directly. Otherwise, they are taken into consideration by introducing a closed-eye period to bridge times, when uncertainties cannot be represented. Through this approach a consistent aggregation of information is achieved.

2 | Soil water movement

Soils can be considered as a porous medium partitioned into a solid matrix and the pore space in between. This pore space can be filled by fluids. In the context of this work, only water and air are considered with the sole focus on the representation of soil water movement.

In this work, I call the mathematical description of a physical system a *representation*, which comprises in the most general sense the four components:

- *Dynamics*: the dynamics specifies how the system's state develops in time at the scale of interest.
- *Subscale physics*: the subscale physics is not explicitly described by the dynamics, but with a parameterization comprising one or more functional forms and their parameters, both with possible spatial and temporal distribution.
- *Superscale physics*: the coupling of the system to the superscale physics in space (boundary condition) and time (initial state).
- *Response*: the response of the system given a specific dynamics, sub- and superscale physics. This is primarily the trajectory of states in time, but also includes derived quantities like fluxes.

According to this definition a representation is specific for each system. It is bounded in space, time, and scale. The following sections describe each component specifically as employed in this work. The focus lies on the explanation of the most important uncertainties within each of these components, to enable their informed assessment and representation in the applications. The description of the dynamics (Sect. 2.1) and subscale physics (Sect. 2.2) is based on *Roth* [2017], where a more complete presentation can be found. Section 2.3 and Sect. 2.4 present superscale physics and response, respectively.

2.1 Dynamics

The dynamics describes how the state is propagated in space and time. At the pore scale, which ranges from about 0.001 mm to 1 mm, the state can be described as the distribution of the solid soil matrix and of air and water occupying the pore space in between. Such a detailed description is not feasible at larger scales, however.

To describe the state of the soil at the larger continuum scale relevant for this work of about 0.001 m to 10 m, averaged quantities can be defined on the basis of a Representative Elementary Volume (REV). An REV is the minimum volume, for which the averaged quantity does not change any more with small changes of the averaging volume. This way the porosity ϕ (–) can be defined as the volume fraction of the pore space of the total volume. Accordingly, the water content θ (–) is defined as the volume fraction of water V_w (L^3) in the total volume V (L^3):

$$\theta = \frac{V_w}{V} \,. \tag{2.1}$$

If the complete pore space is filled with water, the soil is at the saturation water content $\theta_s = \phi$. The minimum water content that always remains in the soil (on reasonable time scales) is the residual water content θ_r. With these quantities the saturation Θ (–) can be defined as

$$\Theta := \frac{\theta - \theta_r}{\theta_s - \theta_r} \,. \tag{2.2}$$

To describe the development of the soil water content state, I start with the description at the pore scale and sketch the necessary steps for a description at the continuum scale. The assumptions made during these steps are crucial to understand the limitations of the final formulation. The first assumption, already made above, is that the pore space is only occupied by water and air. No solutes, or additional fluids like oil are considered.

Under the assumption of a small Strouhal and a small Reynolds number, the water flow in a water filled pore can be described with the time-independent Stokes equation:

$$\mu \nabla^2 \mathbf{v}^\mu = \nabla p^\mu - \rho \mathbf{g} \,, \tag{2.3}$$

with dynamic viscosity μ ($\mathrm{M\,L^{-1}\,T^{-1}}$), density ρ ($\mathrm{M\,L^{-3}}$), velocity $\mathbf{v}$ ($\mathrm{L\,T^{-1}}$), pressure p ($\mathrm{M\,L^{-1}\,T^{-2}}$) and acceleration of gravity $\mathbf{g}$ ($\mathrm{L\,T^{-2}}$). The superscript μ additionally indicates small-scale quantities. A small Strouhal number means that changes of the boundary conditions are slow compared to the relaxation time of the internal dynamics. This is also called local equilibrium assumption and can be violated for strong forcing. A small Reynolds number means that viscosity dominates inertia. This assumption will hold in small pores, but is violated in cracks or large macropores. Additionally, Eq. (2.3) assumes water to be a Newtonian fluid. Because ρ and μ are set to constants, it additionally assumes that the fluid is incompressible and at a constant temperature. Particularly, μ has a noteworthy dependency on temperature. The assumption also means that interface effects between soil matrix and fluid on these quantities are negligible. This may get violated for very fine textured soils like clay.

With the above assumptions, $\mathbf{v}^\mu$ is parallel to $\nabla^2 \mathbf{v}^\mu$ and Eq. (2.3) leads to a linear relation between $\mathbf{v}^\mu$ and the driving potential gradient $\nabla p^\mu - \rho \mathbf{g}$ described with

$$\mathbf{v}^\mu = -\frac{\kappa^\mu(\mathbf{x})}{\mu} \left[\nabla p^\mu - \rho \mathbf{g} \right] , \tag{2.4}$$

where $\kappa^\mu(\mathbf{x})$ (L^2) characterizes the local pore geometry. This inherently assumes that the soil matrix is incompressible as $\kappa^\mu(\mathbf{x})$ does not depend on p^μ.

To obtain the flux law at the continuum scale, averaging $\mathbf{v}^\mu$ over a plane REV yields

$$\mathbf{j} = -\theta \frac{1}{\mu} \langle \kappa^\mu \left[\nabla p^\mu - \rho \mathbf{g} \right] \rangle , \tag{2.5}$$

where $\mathbf{j}$ ($\mathrm{L\,T^{-1}}$) is the flux and $\langle\ \rangle$ denotes the average over the microscopic quantities marked by the superscript μ. The covariance between the forcing ∇p^μ and the pore geometry κ^μ does not allow to simply replace the microscopic quantities by their macroscopic averages. However, because of the linearity in Eq. (2.3), the magnitude of ∇p^μ and ∇p are proportional, even though they need not be parallel due to the pore space geometry. Thus, they can be related through a second rank, symmetric tensor $\mathbf{a}(\mathbf{x})$: $\nabla p^\mu = \mathbf{a}(\mathbf{x}) \nabla p$. Since κ is independent of the macroscopic ∇p, it can be factored out of the microscopic average. This leads to Darcy's law,

$$\mathbf{j} = -\frac{\mathbf{k}}{\mu} \left[\nabla p - \rho \mathbf{g} \right] , \tag{2.6}$$

where the permeability $\mathbf{k}$ (L^2) is again a second rank, symmetric tensor. It incorporates the average, $\mathbf{k} = \theta \langle \kappa \mathbf{a} \rangle$. Typically, $\mathbf{k}$ and μ are combined into the hydraulic conductivity $\mathbf{K}_w$ ($\mathrm{L^3\,T\,M^{-1}}$):

$$\mathbf{K}_w := \frac{\mathbf{k}}{\mu} , \tag{2.7}$$

which is specific for each fluid. Note that the local equilibrium assumption required for Eq. (2.3) now has to hold on the averaging volume. This defines a Maximum Averaging Volume (MAV). Equation (2.6) does only hold when the required REV is smaller than the MAV.

For the case of unsaturated soils, the Buckingham-Darcy law extends Eq. (2.6) to

$$\mathbf{j} = -\mathbf{K}_w(\theta) \left[\nabla \psi_m - \rho \mathbf{g} \right] , \tag{2.8}$$

where the hydraulic conductivity $\mathbf{K}_w$ now depends on the water content θ. This assumes that $\mathbf{K}_w$ does not depend on the air content, which means that water transport as water vapor through the air phase is neglected. However, this assumption is violated for small water contents. Furthermore, the pressure p is replaced by the matric potential ψ_m ($\mathrm{M\,L^{-1}\,T^{-2}}$). It describes the pressure jump across the interface between water and air: $\psi_m = p_w - p_a$, which is given by the Young–Laplace equation

$$\psi_m = 2\sigma_{wa} H , \tag{2.9}$$

where σ_{wa} ($\mathrm{M\,T^{-2}}$) is the surface tension between water and air, and H ($\mathrm{L^{-1}}$) is the mean curvature of the interface. Equation (2.8) further assumes, that the air pressure p_a is constant. This means that ∇p_a has to be negligible compared to ∇p_w. This can be violated for water flow at high water contents.

Consequently, Eq. (2.8) only holds for intermediate water contents, the so called degenerate multiphase regime. Note that the assumption of an essentially incompressible soil matrix for the saturated description in Eq. (2.4) now has to hold for unsaturated soils as well. This can be violated, because soils can shrink and swell with changing water content.

Inserting Eq. (2.8) into the conservation of mass,

$$\frac{\partial \theta}{\partial t} + \nabla \cdot \mathbf{j} = 0\,, \tag{2.10}$$

yields the Richards equation,

$$\frac{\partial \theta}{\partial t} - \nabla \cdot \left[\mathbf{K}_w(\theta)\left[\nabla \psi_m - \rho \mathbf{g}\right]\right] = 0\,, \tag{2.11}$$

which describes the change of the water content state in a soil over time. Note that this equation emphasizes the local equilibrium assumption already required for Eq. (2.3), since $\nabla \psi_m$ has to be well-defined and associated with ${\partial\theta}/{\partial t}$. This affects the MAV, which can easily become smaller than an REV, for example, during a strong rain event, and consequently violates the assumptions of the Richards equation.

A more intuitive formulation of the Richards equation is achieved by expressing the potentials per unit weight instead of per unit volume. This leads to

$$\frac{\partial \theta}{\partial t} - \nabla \cdot \left[\mathbf{K}^*_w(\theta)\left[\nabla h_m - 1\right]\right] = 0\,, \tag{2.12}$$

with the matric head $h_m = {\psi_m}/{\rho \mathbf{g}}$ (L), which now corresponds to the height of an equivalent water column, and $\mathbf{K}^*_w$ ($\mathrm{L\,T^{-1}}$), which can be associated with a velocity. From now on this notation is used and the asterisk * is dropped.

2.2 Subscale physics

The Richards equation (Eq. 2.12) requires the description of $\mathbf{K}_w(\theta)$ and a relation between θ and h_m. These dependencies are called material properties and describe the subscale physics not explicitly represented in Eq. (2.12) any more. They are typically parameterized into simplified functions. Again, it is important to note these simplifications.

To motivate the relation between θ and h_m, recall that the pressure jump across the air-water interface is given through the mean curvature (Eq. 2.9). For a completely wettable capillary, with the capillary rise in static equilibrium, the mean curvature equals the inverse of the radius of the capillary. In this case, the matric head is connected to the radius r (L) of the capillary through

$$h_m = -\frac{1}{\rho g}\frac{2\sigma_{wa}}{r}\,. \tag{2.13}$$

A soil comprises a range of different pore sizes, which leads to a decreasing water content for a decreasing matric head. However, because of varying pore sizes and varying pore radii, soils show a hysteretic behavior.

In this work, I use the simplified form of the *van Genuchten* [1980] parameterization for the unsaturated soil water characteristics $h_m(\Theta)$:

$$h_m(\Theta) = \frac{1}{\alpha}\left[\Theta^{-n/[n-1]} - 1\right]^{1/n}\,, \tag{2.14}$$

where Θ is the saturation (Eq. 2.2), which includes the parameters θ_s and θ_r for the saturated and residual water content. The parameter α (L^{-1}) is a scaling factor and can be related to an inverse air entry value. The air entry value gives the matric head when the largest pores begin to be filled with air and consequently the saturation becomes smaller than 1. The parameter n (–) can be associated with the width of the pore size distribution and influences the sharpness of the air entry. However, both parameters do not have a direct physical relation.

The van Genuchten parameterization does not consider hysteresis. It additionally assumes that the wettability does not change over time and does not depend on the temperature.

The hydraulic conductivity is a tensor depending on the water content. However, it is typically simplified to an isotropic hydraulic conductivity function $K(\Theta)$. It is connected to the pore radius and consequently to the soil water characteristics. *Mualem* [1976] assumed capillary elements where radii are proportional to corresponding lengths and arrived at the expression

$$K(\Theta) = K_0\Theta^{\tau}\left[\frac{\int_0^{\Theta}\mathrm{d}\Theta'/h_m(\Theta')}{\int_0^{1}\mathrm{d}\Theta'/h_m(\Theta')}\right]^2\,, \tag{2.15}$$

where K_0 ($\mathrm{L\,T}^{-1}$) is the saturated hydraulic conductivity and τ (–) can be associated with the increasing flow path tortuosity for decreasing saturation. However, there again is no direct physical relation. Inserting Eq. (2.14) into Eq. (2.15) yields

$$K(\Theta) = K_0\Theta^{\tau}\left[1 - \left[1 - \Theta^{n/[n-1]}\right]^{1-1/n}\right]^2\,. \tag{2.16}$$

The Mualem–van Genuchten parameterization comprises Eq. (2.14) and Eq. (2.16). It is possibly the most common parameterization of the material properties in soil hydrology and is also used in this work. It connects the hydraulic conductivity to the soil water characteristics, by assuming geometric similarity and simplifies implications of the complicated pore geometry into two functions, characterized by a set of six soil hydraulic parameters θ_s, θ_r, α, n, K_0, and τ. The assumption of constant wettability, together with the assumptions of constant ρ, μ, and the incompressibility of the soil matrix already made in Sect. 2.1 are often summarized into one strong assumption: that these parameters are constant in time.

The material properties of a soil vary in space. Large structures, like soil layers, are typically directly represented through individual parameter sets for each layer. This is difficult for smaller heterogeneity, the texture, within such a structure. A possibility to describe the texture in a simplified way is Miller scaling. It assumes geometrical similarity and scales the reference material properties of the structure at every point in space with

$$h_\mathrm{m}(\theta) = h^*_\mathrm{m}(\theta) \cdot \frac{1}{\xi}\,, \tag{2.17}$$

$$K(\theta) = K^*(\theta) \cdot \xi^2\,, \tag{2.18}$$

where * denotes the reference material properties and ξ (–) is the Miller scaling parameter at this location. This scaling cannot represent all aspects of small scale heterogeneity, though. Most importantly, it neglects possible variations of ϕ.

The soil hydraulic parameters introduced in this section can neither be measured directly nor transferred directly from the laboratory to the field. Consequently, they are often associated with the largest uncertainties in soil hydrology.

Both material properties are highly nonlinear and encompass a range of several orders of magnitude. They determine characteristic shapes for the soil water movement. This can be seen when transforming the Richards equation (Eq. 2.12) into the θ-form,

$$\frac{\partial\theta}{\partial t} + V(\theta)\cdot\nabla\theta - \nabla\cdot[D(\theta)\nabla\theta] = 0\,, \tag{2.19}$$

where the second term describes an advection with $V(\theta) = {}^{\mathrm{d}K(\theta)}\!/\!{}_{\mathrm{d}\theta}$ and the third term describes a dispersion with $D(\theta) = {}^{\mathrm{d}h_m(\theta)}\!/\!{}_{\mathrm{d}\theta}K(\theta)$. Due to the rapidly increasing hydraulic conductivity with increasing water content, the advection tends to form sharp shock fronts. This is counteracted by the dispersion, smoothing out the water content, which leads to characteristic shapes.

2.3 Superscale physics

The considered system representing soil water movement has to be limited in space and time. The physics outside of this range is the superscale physics. The coupling to the superscale in space is the boundary condition, and the coupling in time is the initial condition.

Boundary conditions can be described as Dirichlet or Neumann boundary conditions, or combinations thereof. A Dirichlet boundary condition gives the state value at the boundary of the system. This means a water content, or more common a matric head (which is linked to the water content through the material properties). A Neumann boundary condition describes the normal derivative of the state at the boundary. For the Richards equation this is the water flux.

Generally, the description of boundary conditions is challenging. In the following I only describe the boundary conditions employed in this work. A water table at the boundary can be represented through a Dirichlet boundary condition with $h_m = 0\,\mathrm{m}$. However, this assumes that the water table is constant and not influenced by fluxes over the boundary. To reduce the effect of an uncertain boundary, the described domain can be extended and the description close to the uncertain boundary disregarded.

The boundary condition at the interface to the atmosphere is possibly the most difficult one. It is typically strongly influenced by plants. However, in this work the role of plants is neglected completely.

The infiltration into the soil during a rain event, can be described by a Neumann boundary condition. The flux can be determined by measuring the precipitation rate. However, if the rain intensity is too strong the infiltration can become limited by the soil, which results in ponding and possibly surface runoff.

Evaporation from the soil into the atmosphere can be limited by (i) available energy, (ii) the atmospheric demand, or (iii) the water content state in the soil. If the evaporation is limited by the soil, the boundary condition should be defined through a Dirichlet boundary condition giving the atmospheric potential. If the evaporation is limited by the atmosphere, the boundary condition should be described through a Neumann boundary condition. This is assumed in this work.

To describe the atmospheric demand based on atmospheric measurements like they are available from weather stations (net radiation, wind speed, temperature and relative humidity), the empiric FAO Penman–Monteith equation [*Allen et al.*, 1998] can be used. It estimates the reference evapotranspiration for a well watered grass, with specific height, albedo, and surface resistance. The equation considers the energy balance at the surface, Bowen ratio between sensible and latent heat, Dalton's law for potential evaporation, and additionally accounts for evaporative cooling and surface resistances [*Foken*, 2006]. For daily mean values the uncertainty is estimated to range from 10 % to 20 % [*Foken*, 2006]. However, for bare soils a multiplicative factor ranging from 0 to 1.2 has to be applied depending on the water content state of the soil.

The initial condition describes the water content state at the beginning of the time interval considered. It can be estimated using measurements, which are discussed in more detail in the next section. However, measurements are typically sparse. Alternatively a spin-up phase can be employed, where a model is used starting at a previous time. Uncertainties from the initial condition of the spin-up phase become smaller over time, but uncertainties from the model itself increase.

2.4 Response

For known dynamics, subscale physics, and superscale physics of a system, the response can be calculated. This is primarily the trajectory of water content states in time, but also includes derived quantities like fluxes. In this work, only the states are considered. A discretized representation of the continuous states can be calculated using a numerical solver. I employ MuPhi [*Ippisch et al.*, 2006], which uses a cell-centered finite-volume scheme with full-upwinding in space and implicit Euler scheme in time and an inexact Newton-Method with line search to linearize the nonlinear equations.

The calculated response based on dynamics, subscale physics, and superscale physics incorporates all uncertainties discussed above and consequently has large uncertainties itself. Additionally, the numerical solver introduces a spatial resolution. The local equilibrium assumption required for the Richards equation (Eq. 2.12) has to hold on this resolution as well. This means it has to be better than the MAV. It is possible to choose the spatial resolution of the solver smaller than the REV. This may actually be required for numeric stability and accuracy. However, the results will not be meaningful on this finer scale, can only be interpreted above the REV scale, and may indicate a violation of the local equilibrium assumption in the physical representation.

The state cannot only be calculated, but also measured. In this work, time domain reflectometry (TDR) sensors are used to determine the water content. The used design consists of three 20 cm long rods inserted into the soil. By measuring the travel time of an electromagnetic wave guided by the rods, the dielectric permittivity of the surrounding soil can be determined [*Robinson et al.*, 2003]. To relate the measured bulk relative permittivity ϵ_r to the soil water content, a petrophysical relationship is required. Following *Roth et al.* [1990], a mixing law, the complex refractive index model (CRIM), for an isotropic bulk medium is used,

$$\sqrt{\epsilon_r} = \theta\sqrt{\epsilon_{r,w}} + (\phi - \theta)\sqrt{\epsilon_{r,a}} + (1 - \phi)\sqrt{\epsilon_{r,s}}\,, \tag{2.20}$$

with relative permittivity of air $\epsilon_{r,a} = 1$, and relative permittivity of the soil matrix $\epsilon_{r,s} = 5$. The relative permittivity of water is determined with the temperature correction by *Kaatze* [1989] and is $\epsilon_{r,w} = 80$ at 20 °C. The porosity is determined from volumetric soil samples taken during the installation of the probes.

The large difference between $\epsilon_{r,w}$ and $\epsilon_{r,a}$ allows the estimation of the water content in the soil with TDRs. However, their evaluation becomes more difficult in situations with high electric conductivity or relaxation losses [*Robinson et al.*, 2003]. The measurement volume of a TDR for the used design extends around the rods with a distance of $\mathcal{O}(1\,\mathrm{cm})$, but varies based on the bulk dielectric permittivity.

This section shows that there is a dual information about the response. On the one hand from modeling based on dynamics, subscale physics, and superscale physics and on the other hand from measurements. This dual information can be used to improve the representation and reduce uncertainties.

3 | Ensemble Kalman filter

This chapter introduces the data assimilation method employed in this work, the ensemble Kalman filter (EnKF). First, Sect. 3.1 positions data assimilation methods conceptually. Sect. 3.2 introduces the Kalman filter under the assumption of Gaussian uncertainty distributions and linear models. It is the basis for the EnKF (Sect. 3.3), the ensemble extension of the Kalman filter for nonlinear models. A limited ensemble size, the assumption of Gaussian distributions, and un- or ill-represented model errors cause a suboptimal performance. Localization (Sect. 3.4) and inflation (Sect. 3.5) are standard extensions to the EnKF to account for these issues. Extensions for the specific use of the EnKF in hydrology, namely augmented state, damping factor, and iterative filters are described in Sect. 3.6.

Within this work, the EnKF and its extensions were implemented into the *Knowledge Fusion* (KnoFu) software developed in a parallel doctoral study by *Berg* [2018]. KnoFu provides a framework for the coupling of data assimilation methods with models.

3.1 Conceptual overview

Forward model: In forward modeling, measurements and knowledge about dynamics, subscale physics, and superscale physics are used to calculate the response of a system. Measurements of the response are not used (or only used as a control for the forward model).

However, in most geophysical systems dynamics, subscale physics, and superscale physics come with large uncertainties. This is also true for soil hydrology (see chapter 2). Particularly, parameters describing the subscale physics are highly uncertain since they can neither be measured directly nor transferred from the laboratory to the field. This strongly limits the predictive capabilities of forward modeling in soil hydrology.

Inverse modeling: In contrast to forward modeling, inverse modeling uses a measured response to determine its causes. Typically, this means the estimation of parameters in the subscale and superscale physics. However, this limits the consideration of errors to the parameters. Errors in the other components are not considered and consequently incorporated into the parameters.

Since subscale parameters are considered to have the largest uncertainties in soil hydrology, inverse modeling has been applied intensively with reviews, e.g., by *Hopmans et al.* [2002] and *Vrugt et al.* [2008]. Errors in the other components limit its applicability.

Data assimilation: Data assimilation combines information from forward models and measurements into an optimal state estimate. Errors in all components of the representation can – at least in principle – be considered through the state estimation. However, the estimation depends on the correct description of these uncertainties.

In soil hydrology, the estimation of states alone is insufficient. However, data assimilation methods can be extended to estimate parameters along with the states. This offers the possibility to consider model errors in the estimation. Nevertheless, un- or ill-represented uncertainties lead to suboptimal parameter estimation.

Knowledge fusion: Knowledge fusion is the consistent aggregation of all information pertinent to some observed reality [*Bauser et al.*, 2016]. This means that not only measurements but any other relevant information, even expert knowledge, should be incorporated into a representation. Furthermore, uncertainties of all components have to be represented correctly and should even be reduced. Data assimilation methods are promising methods for knowledge fusion but can only partly comply with the requirements. Particularly, the reduction of uncertainties in the dynamics remains an open challenge.

In soil hydrology where uncertainties are present in all representation components, it is necessary to come closer to the goal of knowledge fusion in order to reach a consistent representation of soil water movement end eventually well-founded predictions that include sound uncertainties.

The transition between inverse modeling, data assimilation, and knowledge fusion is continuous. Consequently, there is no consistent differentiation in the literature. For example, *Vrugt et al.* [2008] see data assimilation as a special method for inverse modeling, while *van Leeuwen et al.* [2015] describe how inverse modeling can be seen as a specific branch of data assimilation. In this work, the two are distinguished, whether the method includes state estimation (data assimilation) or not (inverse modeling), since the state estimation provides the means for the consideration of model errors.

Data assimilation methods themselves can be classified either as *filter* or *smoother*. Filters sequentially combine model information with measurement information at a single point in time. Information from previous measurements is already incorporated in the model. Future measurements are not considered for the current estimation. Examples are 3D-Var, Kalman filters, and particle filters. Smoothers on the other hand incorporate measurements from several points in time simultaneously. This allows the consideration of 'future' measurements within the assimilation interval as well. An example is 4D-Var, but also ensemble Kalman smoothers and particle smoothers exist.

While smoothers have the advantage of incorporating several measurements at a time, this reduces the possibilities to update the state estimate and consequently lowers the ability to consider model errors. An application in hydrology showed the superiority of the EnKF over the ensemble smoother [*Crestani et al.*, 2013].

At the basis of all data assimilation methods is Bayes' theorem to combine measurements and models into an optimal state estimation [*van Leeuwen et al.*, 2015]. It relates the conditional probability density function (pdf) of the state given the measurements $p(\boldsymbol{u}|\boldsymbol{d})$ (posterior) to the conditional pdf of the measurements given the state $p(\boldsymbol{d}|\boldsymbol{u})$ (likelihood) and the pdf of the state $p(\boldsymbol{d})$ (prior):

$$p(\boldsymbol{u}|\boldsymbol{d}) = \frac{p(\boldsymbol{d}|\boldsymbol{u})p(\boldsymbol{u})}{p(\boldsymbol{d})} . \tag{3.1}$$

In this case of measurements and state, the state $\boldsymbol{u}$ is the variable, while a realization of the measurements $\boldsymbol{d}$ is already given.

The pdf $p(\boldsymbol{d})$ is not the pdf of the measurements as such, but the pdf of the measurements before they are actually made [*van Leeuwen et al.*, 2015]. This is typically hard to determine. Since the measurements are given, $p(\boldsymbol{d})$ can be calculated as

$$p(\boldsymbol{d}) = \int p(\boldsymbol{d}, \boldsymbol{u}) d\boldsymbol{u} = \int p(\boldsymbol{d}|\boldsymbol{u}) p(\boldsymbol{u}) d\boldsymbol{u} \tag{3.2}$$

and becomes a normalization constant, but requires $p(\boldsymbol{d}) \neq 0$.

3.2 Kalman filter

This section follows *van Leeuwen* [2015] and *Welch and Bishop* [2006]. The Kalman filter is based on the assumption of a linear model of a Markov process and a Gaussian error distribution. It is a sequential algorithm iterating between a forecast step, which propagates a state including its uncertainty forward in time, and an analysis step, which combines the uncertain model information with uncertain measurements at this time into an optimal estimate of the state. Below, these two steps are explained in more detail.

Forecast: The spatially discretized representation of the true state $\boldsymbol{u}_{\text{true}}$ at time $k-1$ is linked to the true state at time k through the forward model M and the model error $\boldsymbol{\eta}$,

$$\boldsymbol{u}_{\text{true},k} = M\left(\boldsymbol{u}_{\text{true},k-1}\right) + \boldsymbol{\eta}_{k-1} = \mathbf{M}_{k-1}\boldsymbol{u}_{\text{true},k-1} + \boldsymbol{\eta}_{k-1} , \tag{3.3}$$

where, due to the linear model, the forward propagation can also be represented through a matrix multiplication. The model error (or process noise) $\boldsymbol{\eta}$ is assumed to be Gaussian noise with zero mean and error covariance $\mathbf{Q}$:

$$\boldsymbol{\eta} \sim \mathcal{N}\left(0, \mathbf{Q}\right) , \tag{3.4}$$

$$\mathbf{Q} = \overline{\boldsymbol{\eta}\boldsymbol{\eta}^T} . \tag{3.5}$$

Through the Gaussian assumption, a state at a specific time including its uncertainty is characterized by its best guess $\boldsymbol{u}_k$ and error covariance matrix $\mathbf{P}_k$,

$$\mathbf{P}_k = \overline{\left[\boldsymbol{u}_k - \boldsymbol{u}_{\text{true},k}\right]\left[\boldsymbol{u}_k - \boldsymbol{u}_{\text{true},k}\right]^T} \,. \tag{3.6}$$

To propagate a state from a previous analysis at time $k-1$ forward to time k, the model is applied to it,

$$\boldsymbol{u}_{\text{f},k} = \mathbf{M}_{k-1}\boldsymbol{u}_{\text{a},k-1} \,, \tag{3.7}$$

where the subscript "f" denotes forecast and the subscript "a" denotes analysis. The state error covariance matrix is propagated through the linear model as well and it additionally increases due to the model error with

$$\mathbf{P}_{\text{f},k} = \mathbf{M}_{k-1}\mathbf{P}_{\text{a},k-1}\mathbf{M}_{k-1}^T + \mathbf{Q}_{k-1} \,. \tag{3.8}$$

This way, the state, including its uncertainties, is propagated in time.

Analysis: The analysis combines model information, given through the forecast state $\boldsymbol{u}_{\text{f},k}$ and its error covariance matrix $\mathbf{P}_{\text{f},k}$, with measurement information at this time k into an analysis state $\boldsymbol{u}_{\text{a},k}$. For clarity, the subscript k is dropped in this paragraph, since the complete analysis step is performed at this time.

The measurement vector $\boldsymbol{d}$ is linked to the true state through the measurement operator $\mathbf{H}$ and the measurement error $\boldsymbol{\epsilon}$,

$$\boldsymbol{d} = \mathbf{H}\boldsymbol{u}_{\text{true}} + \boldsymbol{\epsilon} \,, \tag{3.9}$$

where the measurement error is assumed to be Gaussian noise with zero mean and error covariance $\mathbf{R}$:

$$\boldsymbol{\epsilon} \sim \mathcal{N}\left(0, \mathbf{R}\right) \,, \tag{3.10}$$

$$\mathbf{R} = \overline{\boldsymbol{\epsilon}\boldsymbol{\epsilon}^T} \,. \tag{3.11}$$

The measurement operator maps from the state space to the measurement space. The errors in both are assumed to be Gaussian. Consequently, the measurement operator has to be linear.

To combine the measurement information with the model information, Bayes' theorem is applied. It is simplified through the Gaussian assumption of model (prior) and measurements (likelihood) and the posterior yields

$$p(\boldsymbol{u}|\boldsymbol{d}) \propto \exp\left[-\frac{1}{2}\left[\boldsymbol{u} - \boldsymbol{u}_{\text{f}}\right]^T \mathbf{P}_{\text{f}}^{-1}\left[\boldsymbol{u} - \boldsymbol{u}_{\text{f}}\right] - \frac{1}{2}\left[\boldsymbol{d} - \mathbf{H}\boldsymbol{u}\right]^T \mathbf{R}^{-1}\left[\boldsymbol{d} - \mathbf{H}\boldsymbol{u}\right]\right] \tag{3.12}$$

$$\propto \exp\left[-\frac{1}{2}\left[\boldsymbol{u} - \boldsymbol{u}_{\text{a}}\right]^T \mathbf{P}_{\text{a}}^{-1}\left[\boldsymbol{u} - \boldsymbol{u}_{\text{a}}\right]\right] \,, \tag{3.13}$$

where Eq. (3.13) is reached through some calculations (see Appendix A.1). The posterior is a Gaussian distribution with the analysis state $\boldsymbol{u}_\mathrm{a}$ as the best guess and the error covariance $\mathbf{P}_\mathrm{a}$. They are derived as

$$\boldsymbol{u}_\mathrm{a} = \boldsymbol{u}_\mathrm{f} + \mathbf{K}\left[\boldsymbol{d} - \mathbf{H}\boldsymbol{u}_\mathrm{f}\right] , \tag{3.14}$$

$$\mathbf{P}_\mathrm{a} = \left[\mathbf{1} - \mathbf{K}\mathbf{H}\right]\mathbf{P}_\mathrm{f} , \tag{3.15}$$

where $\mathbf{K}$ is the Kalman gain,

$$\mathbf{K} = \mathbf{P}_\mathrm{f}\mathbf{H}^T\left[\mathbf{H}\mathbf{P}_\mathrm{f}\mathbf{H}^T + \mathbf{R}\right]^{-1} . \tag{3.16}$$

The Kalman gain weights the forecast error covariance matrix with the total error of forecast error covariance matrix and measurement error covariance matrix in the measurement space. It maps back from the measurement space to the state space based on the covariances in the forecast error covariance matrix. Thus, in Eq. (3.14) the Kalman gain weights the differences between measurements and forecast state in the measurement space and transfers them to the state space. The forecast state is then updated with this weighted difference to the analysis state. Through combining the information, the uncertainty is decreased. It minimizes the analysis error covariance matrix given in Eq. (3.15).

By iterating between forecast and analysis, the state is improved sequentially. The complete Kalman filter cycle is summarized in Fig. 3.1. It requires a description of a linear forward model and its error covariance matrix, measurements and their error covariance matrix, and a measurement operator mapping from the state space to the measurement space. Additionally, an initial guess for the state and its error covariance matrix are required. The limitations are the assumptions of a linear model and Gaussian error distributions, which also leads to a linear measurement operator and linear corrections in the analysis. Through the iterative application, it is also necessary to assume errors to be uncorrelated in time.

3.3 Ensemble Kalman filter

The EnKF [*Evensen*, 1994; *Burgers et al.*, 1998] is the Monte Carlo extension of the Kalman filter for nonlinear models. The propagation of the state error covariance matrix in Eq. (3.8) is not directly transferable to nonlinear models. The EnKF resolves this issue by approximating the state uncertainty through an ensemble of states, which propagates the uncertainty. However, it retains the assumption of Gaussian distributions in the analysis, even though this assumption does not hold strictly any more for nonlinear models.

Through the Gaussian assumption, an ensemble of states $\boldsymbol{u}^n$ represents a state and

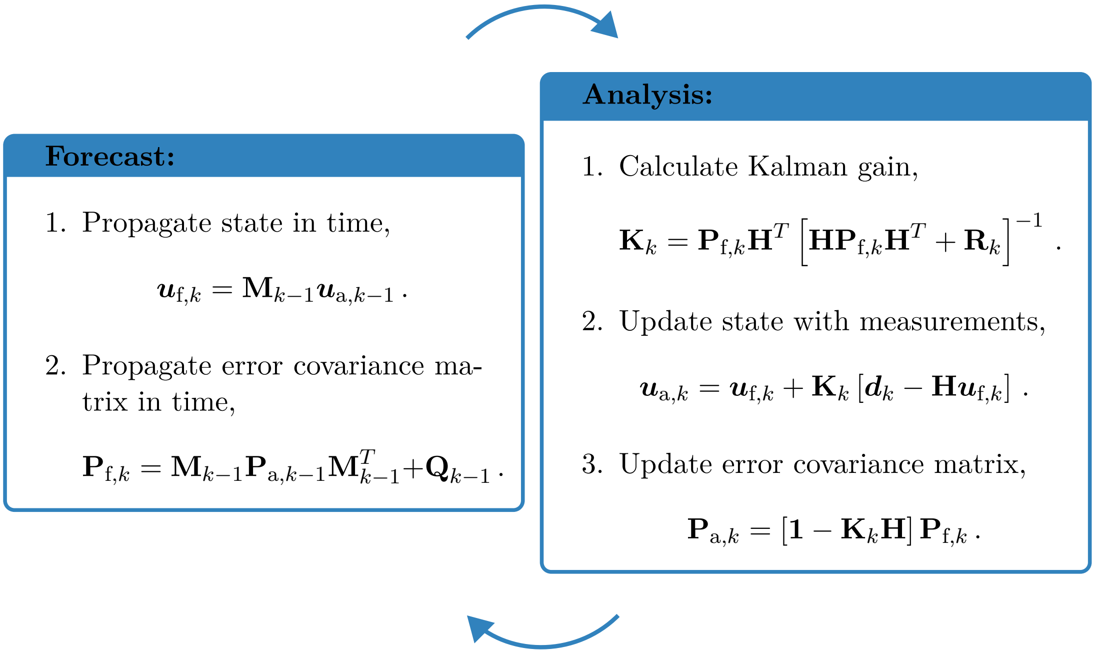

Forecast:

1. Propagate state in time,
$$\boldsymbol{u}_{\mathrm{f},k} = \mathbf{M}_{k-1}\boldsymbol{u}_{\mathrm{a},k-1}\,.$$
2. Propagate error covariance matrix in time,
$$\mathbf{P}_{\mathrm{f},k} = \mathbf{M}_{k-1}\mathbf{P}_{\mathrm{a},k-1}\mathbf{M}_{k-1}^{T}+\mathbf{Q}_{k-1}\,.$$

Analysis:

1. Calculate Kalman gain,
$$\mathbf{K}_k = \mathbf{P}_{\mathrm{f},k}\mathbf{H}^T\left[\mathbf{H}\mathbf{P}_{\mathrm{f},k}\mathbf{H}^T+\mathbf{R}_k\right]^{-1}\,.$$
2. Update state with measurements,
$$\boldsymbol{u}_{\mathrm{a},k} = \boldsymbol{u}_{\mathrm{f},k} + \mathbf{K}_k\left[\boldsymbol{d}_k - \mathbf{H}\boldsymbol{u}_{\mathrm{f},k}\right]\,.$$
3. Update error covariance matrix,
$$\mathbf{P}_{\mathrm{a},k} = \left[\mathbf{1} - \mathbf{K}_k\mathbf{H}\right]\mathbf{P}_{\mathrm{f},k}\,.$$

Figure 3.1: The Kalman filter cycle. It consists of Eq. (3.7), (3.8), (3.14), (3.15), and (3.16). Modified from *Welch and Bishop* [2006].

its error covariance with

$$\boldsymbol{u} \simeq \boldsymbol{u}_{\mathrm{ens}} = \overline{\boldsymbol{u}^n}\,, \tag{3.17}$$

$$\mathbf{P} \simeq \mathbf{P}_{\mathrm{ens}} = \overline{\left[\boldsymbol{u}^n - \overline{\boldsymbol{u}^n}\right]\left[\boldsymbol{u}^n - \overline{\boldsymbol{u}^n}\right]^T}\,, \tag{3.18}$$

where n denotes the ensemble members with $n = 1, \ldots, N$ for the ensemble size N. Below, forecast and analysis are described in more detail.

Forecast: In the forecast each ensemble member is propagated forward in time with the nonlinear model M, to represent the propagation of the uncertainties in the analysis state. To each ensemble member, a realization of the model error is added to represent the model uncertainty directly:

$$\boldsymbol{u}_{\mathrm{f},k}^n = M\left(\boldsymbol{u}_{\mathrm{a},k-1}^n\right) + \boldsymbol{\eta}^n\,. \tag{3.19}$$

Under the assumption of Gaussian distributions, the uncertainty is characterized through the error covariance matrix around the mean $\overline{\boldsymbol{u}_{\mathrm{f},k}^n}$:

$$\mathbf{P}_{\mathrm{f},k,\mathrm{ens}} = \overline{\left[\boldsymbol{u}_{\mathrm{f},k}^n - \overline{\boldsymbol{u}_{\mathrm{f},k}^n}\right]\left[\boldsymbol{u}_{\mathrm{f},k}^n - \overline{\boldsymbol{u}_{\mathrm{f},k}^n}\right]^T}\,. \tag{3.20}$$

Analysis: In the analysis, the measurement information is incorporated. Like for the state, its uncertainty can be represented through an ensemble

$$\boldsymbol{d}^n = \boldsymbol{d} + \boldsymbol{\epsilon}^n \,, \tag{3.21}$$

with the measurement error covariance

$$\mathbf{R}_{\text{ens}} = \overline{[\boldsymbol{\epsilon}^n]\,[\boldsymbol{\epsilon}^n]^T} \,. \tag{3.22}$$

Again, the subscript k is dropped for clarity. Instead of the approximated covariance matrix, the exact one can be used as well [*Evensen*, 2003], which is actually done in this work.

With the approximated error covariance matrices, the Kalman gain can be calculated as before,

$$\mathbf{K}_{\text{ens}} = \mathbf{P}_{\text{f,ens}}\mathbf{H}^T \left[\mathbf{H}\mathbf{P}_{\text{f,ens}}\mathbf{H}^T + \mathbf{R}_{\text{ens}}\right]^{-1} \,. \tag{3.23}$$

Instead of just updating the mean, each ensemble member is updated individually, leading to the analysis ensemble $\boldsymbol{u}_{\text{a}}^n$,

$$\boldsymbol{u}_{\text{a}}^n = \boldsymbol{u}_{\text{f}}^n + \mathbf{K}_{\text{ens}}\left[\boldsymbol{d}^n - \mathbf{H}\boldsymbol{u}_{\text{f}}^n\right] \,. \tag{3.24}$$

Each ensemble member is updated with $\boldsymbol{d}^n$, which includes for each member a realization of the measurement error, added to the actual measurement. This is necessary, so that the analysis ensemble directly resembles the correct analysis error covariance matrix [*Burgers et al.*, 1998],

$$\mathbf{P}_{\text{a,ens}} = \left[\mathbf{1} - \mathbf{K}_{\text{ens}}\mathbf{H}\right]\mathbf{P}_{\text{f,ens}} \,. \tag{3.25}$$

However, adding noise to a measurement may seem uncalled-for. A more intuitive explanation by *van Leeuwen* [2015] is that the measurement noise is not added to measurements but to the artificial measurements on the ensemble member $\mathbf{H}\boldsymbol{u}_{\text{f}}^n$, since the actual measurements $\boldsymbol{d}$ already includes a measurement error. This way, equals are compared: measurements including a measurement error.

The complete EnKF scheme is summarized in Fig. 3.2. Note that from now on the subscript “ens” is dropped for clarity.

The additional noise from the measurement ensemble in Eq. (3.24) can be eliminated by employing square root filters. They perform a deterministic transformation from the forecast to the analysis ensemble. This is achieved by requiring Eq. (3.25) to hold. Since the transformation is not unique, several square root filters exist. The resulting analysis ensembles from these different filters have the same error covariances, but differ in higher moments [*Tippett et al.*, 2003].

Examples for square root filters are the ensemble square root filter (EnSRF), which uses a modified Kalman gain on the differences to the mean to fulfill Eq. (3.25) [*Whitaker and Hamill*, 2002]; the ensemble adjustment Kalman filter (EAKF), which performs the analysis in the space where the forecast error covariance is $\mathbf{1}$ and the

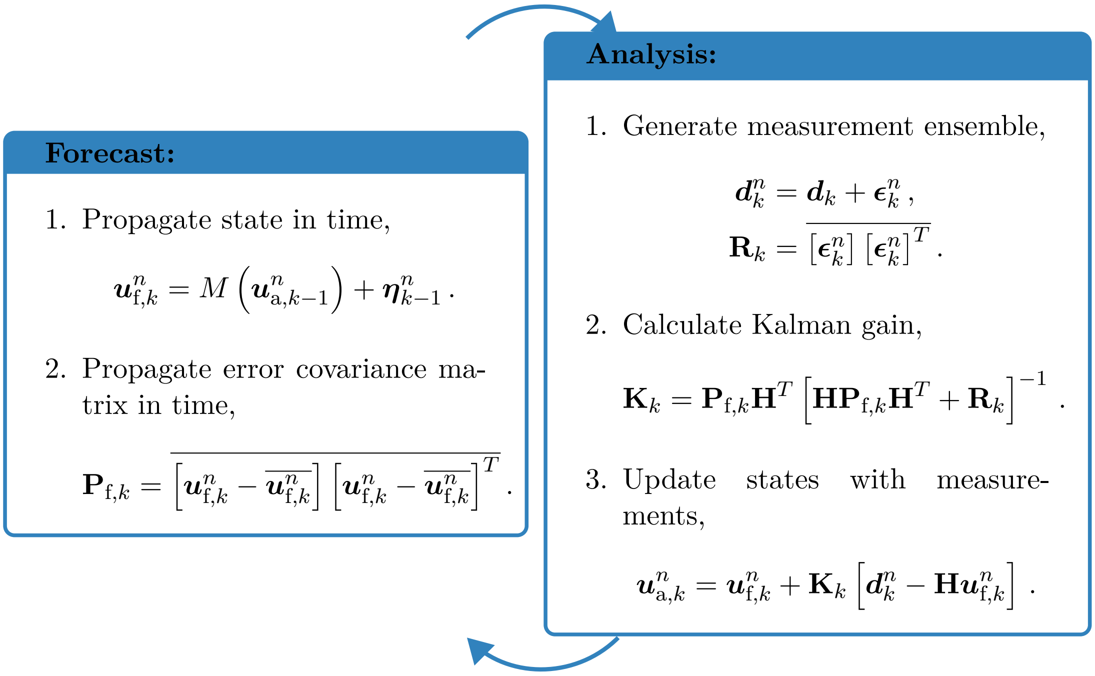

Forecast:

1. Propagate state in time,
$$\boldsymbol{u}^n_{\mathrm{f},k} = M\left(\boldsymbol{u}^n_{\mathrm{a},k-1}\right) + \boldsymbol{\eta}^n_{k-1}\,.$$
2. Propagate error covariance matrix in time,
$$\mathbf{P}_{\mathrm{f},k} = \overline{\left[\boldsymbol{u}^n_{\mathrm{f},k} - \overline{\boldsymbol{u}^n_{\mathrm{f},k}}\right]\left[\boldsymbol{u}^n_{\mathrm{f},k} - \overline{\boldsymbol{u}^n_{\mathrm{f},k}}\right]^T}\,.$$

Analysis:

1. Generate measurement ensemble,
$$\boldsymbol{d}^n_k = \boldsymbol{d}_k + \boldsymbol{\epsilon}^n_k\,,$$
$$\mathbf{R}_k = \overline{\left[\boldsymbol{\epsilon}^n_k\right]\left[\boldsymbol{\epsilon}^n_k\right]^T}\,.$$
2. Calculate Kalman gain,
$$\mathbf{K}_k = \mathbf{P}_{\mathrm{f},k}\mathbf{H}^T\left[\mathbf{H}\mathbf{P}_{\mathrm{f},k}\mathbf{H}^T + \mathbf{R}_k\right]^{-1}\,.$$
3. Update states with measurements,
$$\boldsymbol{u}^n_{\mathrm{a},k} = \boldsymbol{u}^n_{\mathrm{f},k} + \mathbf{K}_k\left[\boldsymbol{d}^n_k - \mathbf{H}\boldsymbol{u}^n_{\mathrm{f},k}\right]\,.$$

Figure 3.2: The EnKF cycle. It consists of Eq. (3.19), (3.20), (3.21), (3.22), (3.23), and (3.24). Modified from *Welch and Bishop* [2006].

measurement error covariance is diagonal [*Anderson*, 2001]; and the local ensemble transform Kalman filter (LETKF), which performs most of the analysis in the ensemble member space and is expected to be the fastest filter when the number of ensemble members is smaller than the number of measurements and the number of state dimensions [*Hunt et al.*, 2007].

Square root filters can reduce sampling error and improve the accuracy of the estimation [*Tippett et al.*, 2003]. However, this is mainly important for small ensemble sizes. For large ensembles, *Lawson and Hansen* [2004] found the stochastic EnKF to be able to handle nonlinearity in the forecast better than deterministic square root filters. The reason for this is that the stochastic filter reduces non-Gaussian higher moments, while the deterministic filters tend to maintain them.

In this work, examples are small enough so that a sufficient ensemble size can be maintained. Consequently, the stochastic EnKF is employed.

3.4 Localization

The forecast error covariance matrix in the EnKF is approximated through an ensemble. Typically, the number of state dimensions is larger than the number of ensemble members. In atmospheric sciences, the number of measurements exceeds the number of ensemble members as well. However, the ensemble can only provide $N_{\mathrm{ens}}-1$ directions in phase space. This is known as the rank problem [*Houtekamer and Zhang*, 2016]. Consequently, the signal to noise ratio between state dimensions in the covariance matrix worsens with decreasing correlations, where correlations will typically decrease with increasing physical distance [*Hamill et al.*, 2001].

One possibility to reduce this issue is localization [*Houtekamer and Mitchell*, 1998], with the idea to separate the complete setting into several local problems. For each of those the complete ensemble size is available. This can be realized by reducing covariances with distance through a correlation function ρ [*Houtekamer and Mitchell*, 2001]. This alters the calculation of the Kalman gain to

$$\mathbf{K}_k = (\rho \circ \mathbf{P}_{\mathrm{f},k})\,\mathbf{H}^T \left[\mathbf{H}\,(\rho \circ \mathbf{P}_{\mathrm{f},k})\,\mathbf{H}^T + \mathbf{R}_k\right]^{-1}\,, \tag{3.26}$$

where $\rho \circ \mathbf{P}_{\mathrm{f},k}$ denotes the entrywise product of the covariance matrix $\mathbf{P}_{\mathrm{f},k}$ with a correlation matrix $\mathbf{C}$. The entry $(\mathbf{C})_{ij}$ of the correlation matrix is determined from the correlation function ρ based on the distance between the locations of the state dimensions i and j.

A typically employed correlation function is the fifth-order piecewise rational function defined by *Gaspari and Cohn* [1999]:

$$\rho = \begin{cases} -\frac{1}{4}(|z|/c)^5 + \frac{1}{2}(|z|/c)^4 + \frac{5}{8}(|z|/c)^3 - \frac{5}{3}(|z|/c)^2 + 1\,, & 0 \le |z| \le c\,, \\ \frac{1}{12}(|z|/c)^5 - \frac{1}{2}(|z|/c)^4 + \frac{5}{8}(|z|/c)^3 + \frac{5}{3}(|z|/c)^2 & \\ \quad -5(|z|/c) + 4 - \frac{2}{3}(c/|z|)\,, & c \le |z| \le 2c\,, \\ 0\,, & 2c \le |z|\,, \end{cases} \tag{3.27}$$

where z is the distance between the dimensions and c defines a length scale. The function is similar to a Gaussian but with local support, which introduces a cutoff length at distance $2c$. The optimal choice of c depends on the problem itself, but also depends on the ensemble size.

Localization is seen as an essential extension of the EnKF that makes the approximation through an ensemble feasible for large systems. However, it is not part of the Kalman filter theory and influences details in the analysis. For example, without localization it is possible to process uncorrelated measurements sequentially without altering the results. With localization this equality does not hold any more [*Houtekamer and Zhang*, 2016].

3.5 Inflation

Localization cannot completely prevent spurious correlations, which reduce the uncertainty in the EnKF analysis too strong and cause a too small ensemble spread [*Houtekamer and Mitchell*, 1998; *van Leeuwen*, 1999]. Unrepresented errors in the forecast cause too small uncertainties as well. This effect is also called inbreeding.

It can eventually lead to filter divergence, where the model uncertainty becomes so small that the state estimation primarily trusts the forecast model and progressively underweights measurements. Thus, the state can increasingly diverge from the measurements. Inflation methods can counter this issue by increasing the ensemble spread.

3.5.1 Additive inflation

The model error considered in Eq. (3.19) is also called additive inflation. To each ensemble member n a realization $\boldsymbol{\eta}^n$ of the model error $\boldsymbol{\eta}$ is added, where $\boldsymbol{\eta}$ is assumed to be have a Gaussian distribution with zero mean. It is a possibility to directly represent model errors. In the atmospheric sciences for example, *Whitaker et al.* [2008] used a reanalysis of historical weather predictions to determine the additive model error. Generally, and particularly in soil hydrology, such detailed prior knowledge is difficult to achieve.

3.5.2 Multiplicative inflation

The spread of the forecast ensemble can be increased through multiplicative inflation. Therefore, the distance of each individual ensemble member to the mean is increased with an inflation factor λ [*Anderson and Anderson*, 1999],

$$\boldsymbol{u}^n_{\mathrm{f,inf}} = \sqrt{\lambda}\left(\boldsymbol{u}^n_{\mathrm{f}} - \overline{\boldsymbol{u}^n_{\mathrm{f}}}\right) + \overline{\boldsymbol{u}^n_{\mathrm{f}}}\,. \tag{3.28}$$

The inflation factor is applied to the complete augmented state. It increases the values in the forecast error covariance matrix with $\mathbf{P}_{\mathrm{f,inf}} = \lambda \mathbf{P}_{\mathrm{f}}$, but does not alter the mean value, $\overline{\boldsymbol{u}^n_{\mathrm{f,inf}}} = \overline{\boldsymbol{u}^n_{\mathrm{f}}}$.

The inflation factor has to be tuned for each system. It additionally depends on the ensemble size [*Hamill et al.*, 2001]. To avoid tuning, *Wang and Bishop* [2003] estimate the inflation factor based on the distance between measurements and forecast. Ideally, this distance is represented through the measurement error covariance matrix and the forecast error covariance matrix:

$$\overline{\left(\boldsymbol{d} - \mathbf{H}\overline{\boldsymbol{u}^n_{\mathrm{f}}}\right)\left(\boldsymbol{d} - \mathbf{H}\overline{\boldsymbol{u}^n_{\mathrm{f}}}\right)^T} = \mathbf{H}\mathbf{P}_{\mathrm{f,inf}}\mathbf{H}^T + \mathbf{R}\,. \tag{3.29}$$

Therefore, the authors suggest to estimate the inflation factor as

$$\lambda = \frac{\left(\boldsymbol{d} - \mathbf{H}\overline{\boldsymbol{u}^n_{\mathrm{f}}}\right)^T\left(\boldsymbol{d} - \mathbf{H}\overline{\boldsymbol{u}^n_{\mathrm{f}}}\right) - \mathrm{Tr}(\mathbf{R})}{\mathrm{Tr}(\mathbf{H}\mathbf{P}_{\mathrm{f}}\mathbf{H}^T)}\,. \tag{3.30}$$

Similarly, based on *Desroziers et al.* [2005], *Li et al.* [2009] additionally use the distance between analysis and forecast,

$$\lambda = \frac{\left(\mathbf{H}\overline{\boldsymbol{u}^n_{\mathrm{a}}} - \mathbf{H}\overline{\boldsymbol{u}^n_{\mathrm{f}}}\right)^T\left(\boldsymbol{d} - \mathbf{H}\overline{\boldsymbol{u}}_{\mathrm{f}}\right)}{\mathrm{Tr}(\mathbf{H}\mathbf{P}_{\mathrm{f}}\mathbf{H}^T)}\,. \tag{3.31}$$

However, these inflation factors estimated at one time step can vary strongly between different time steps. Thus, *Wang and Bishop* [2003] actually estimate a product of all previous inflation factors, while *Li et al.* [2009] use a Kalman filter to smooth the factors.

Anderson [2007] directly bases the estimation of an inflation factor on Bayes' theorem. For a single measurement i the distance b between measurement and forecast is

$$b = \left|(\boldsymbol{d})_i - \left(\mathbf{H}\overline{\boldsymbol{u}_\mathrm{f}^n}\right)_i\right| \,. \tag{3.32}$$

Again, this should be equal to the expected distance ϑ based on the uncertainties,

$$\vartheta = \sqrt{\lambda\left(\mathbf{H}\mathbf{P}_\mathrm{f}\mathbf{H}\right)_{ii} + \left(\mathbf{R}\right)_{ii}}\,. \tag{3.33}$$

Through the assumption that $\boldsymbol{d}$ and $\mathbf{H}\overline{\boldsymbol{u}_\mathrm{f}}$ are unbiased and normally distributed, *Anderson* [2007] assumes that b is also normally distributed with $d \sim \mathcal{N}\left(0, \vartheta^2\right)$. Note that the absolute value taken in Eq. (3.32) actually leads to a half-normal distribution. However, this only impacts a normalization constant because the distribution of b is the likelihood in Bayes theorem. Consequently, b is given and λ is the variable. Note that the likelihood is not normally distributed in λ.

The prior for lambda is assumed to be normally distributed around the previous inflation factor $\lambda \sim \mathcal{N}\left(\lambda_\mathrm{f}, \sigma_\lambda^2\right)$, with the uncertainty σ_λ. Keeping this uncertainty constant is one possibility to avoid a closure problem, where the inflation would require its own inflation. In this case, it is a tuning parameter. However, *Anderson* [2007] shows that the results do not depend on the choice in a wide range. The posterior is estimated by finding the inflation factor λ, that maximizes the product of likelihood and prior. *Anderson* [2007] shows that the likelihood is extremely flat compared to the prior. The distribution around the maximum of the posterior is assumed to be Gaussian with the constant uncertainty σ_λ. By iterating over this scheme, all measurements can be included in the estimation of the scalar λ, which is additionally constrained to $\lambda \geq 1$.

Anderson [2009] extends this method to estimate a vector $\boldsymbol{\lambda}$, where the inflation is determined for each state dimension individually based on the correlations between measurements and states. Therefore, the inflation factor λ in Eq. (3.33) is replaced by a reduced inflation factor λ' based on the correlations,

$$\lambda' = \left[1 + r_{ij}\left[\sqrt{\lambda_j} - 1\right]\right]^2 \,, \tag{3.34}$$

where λ_j is the j-th component of the inflation vector $\boldsymbol{\lambda}$ and r_{ij} is the correlation between measurement i and state dimension j. If a localization is used, it has to be included in r.

With this algorithm, when an inflation is required, the maximum likelihood is at a stronger inflation for weakly correlated state components than for strongly correlated ones. However, the likelihood is flatter for weakly correlated states and counteracts this. Thus, the adjustment speed of the corresponding inflation factor is reduced, which actually leads to – as intended – smaller inflation factors in regions with low correlations to measurements.

3.5.3 Relaxation methods

Relaxation methods attempt to increase the ensemble spread by relaxing the reduction performed in the analysis. *Zhang et al.* [2004] introduce a relaxation to prior perturbations, where the distance of an analysis ensemble member to the mean $\boldsymbol{u}_\mathrm{a}^n - \overline{\boldsymbol{u}_\mathrm{a}^n}$ is relaxed back to its forecast distance $\boldsymbol{u}_\mathrm{f}^n - \overline{\boldsymbol{u}_\mathrm{f}^n}$,

$$\boldsymbol{u}_{\mathrm{a,inf}}^n - \overline{\boldsymbol{u}_\mathrm{a}^n} = [1-\upsilon]\left[\boldsymbol{u}_\mathrm{a}^n - \overline{\boldsymbol{u}_\mathrm{a}^n}\right] + \upsilon\left[\boldsymbol{u}_\mathrm{f}^n - \overline{\boldsymbol{u}_\mathrm{f}^n}\right] , \tag{3.35}$$

where υ is a tuning parameter.

Similarly, *Whitaker and Hamill* [2012] suggest a relaxation to prior spread according to

$$\boldsymbol{\sigma}_{\mathrm{a,inf}} = [1-\upsilon]\,\boldsymbol{\sigma}_\mathrm{a} + \upsilon\boldsymbol{\sigma}_\mathrm{f}\,, \tag{3.36}$$

where $\boldsymbol{\sigma}$ is the vector of standard deviations of the ensemble. The distance to the mean of each ensemble member is then increased in each state dimension so that Eq. (3.36) holds. Again, υ is a tuning parameter.

Ying and Zhang [2015] expand this idea further and estimate the relaxation by first estimating a multiplicative inflation factor using Eq. (3.31), which is then translated into an estimate of υ. This way, the distance to measurements is considered. However, the transfer to individual state dimensions is not directly based on the measurements, but on the reduction in the analysis.

3.6 EnKF in hydrology

Data assimilation methods have their main application in weather forecasting, which is consequently the driving force behind many recent advances [*van Leeuwen et al.*, 2015]. However, hydrologic systems differ fundamentally from atmospheric systems.

In weather forecasting, data assimilation is used to estimate the initial state for the subsequent prediction. Due to the divergent nature of atmospheric systems, this is crucial, since differences to the true state lead to increasingly larger errors in the prediction. This sensitivity to the initial condition is also known as the butterfly effect.

Soil hydrologic systems have a convergent dynamics, and the initial condition will become less important over time. Instead, the state development strongly depends on the highly nonlinear material properties and the boundary conditions. This calls for altered approaches in hydrology.

3.6.1 Augmented state

The state $\boldsymbol{u}$ estimated with the EnKF can be extended to an augmented state $\boldsymbol{u}^*$. This augmented state can include further components like soil hydrologic parameters

$\boldsymbol{u}^* = [\boldsymbol{u}, \boldsymbol{\varphi}]$, where the asterisk * will be dropped from now on. This state augmentation with an EnKF was first demonstrated in atmospheric sciences [*Anderson*, 2001] but is much more common in hydrology.

An augmented state requires a forecast for each component. For the state itself this remains the dynamics, while the parameters $\boldsymbol{\varphi}$ are typically assumed to be constant in time:

$$\boldsymbol{\varphi}^n_{\mathrm{f},k} = \boldsymbol{\varphi}^n_{\mathrm{a},k-1} \,. \tag{3.37}$$

The forecast state now also depends on the corresponding parameter set $\boldsymbol{\varphi}^n_{\mathrm{a},k-1}$. This way, uncertainties in the parameters are propagated as well. The analysis is not altered by the use of an augmented state. Consequently, state and parameters can be updated jointly based on the measurements of the state. However, this analysis is linearized, whereas the relation to the parameters can be highly nonlinear.

Localization (Sect. 3.4) can be directly transferred to the augmented state. It can specify which measurement is allowed to impact the estimation of each individual parameter and gives possibilities to introduce additional knowledge into the estimation.

Inflation (Sect. 3.5) is more difficult to transfer to an augmented state. The forecast of the parameters is typically assumed to be constant. Consequently, they are only changed through the analysis - and the inflation. The dynamics is not able to compensate possible overinflation. This makes the use of inflation more delicate.

3.6.2 Damping factor

The damping factor [*Hendricks Franssen and Kinzelbach*, 2008] reduces the analysis update (Eq. 3.24) by a scalar factor $\gamma \in [0, 1]$:

$$\boldsymbol{u}^n_{\mathrm{a}} = \boldsymbol{u}^n_{\mathrm{f}} + \gamma \cdot \mathbf{K} \left[\boldsymbol{d}^n - \mathbf{H} \boldsymbol{u}^n_{\mathrm{f}} \right] \,. \tag{3.38}$$

For the usage with an augmented state, the damping factor has been extended to a vector $\boldsymbol{\gamma}$ and an entrywise multiplication [*Wu and Margulis*, 2011]. This way, different augmented state components can be treated differently. Typically, parameters are multiplied with a smaller factor than the state.

The damping factor has similarities to the relaxation methods (Sect. 3.5.3). It lowers the reduction of the uncertainty and alleviates the inbreeding problem. In contrast to the relaxation methods, it also influences the mean value. This can alleviate issues with the linearized analysis at the cost of a suboptimal best guess. This is especially useful for parameters where the forecast is assumed to be constant. Consequently, the parameter estimation is just slowed down.

3.6.3 Iterative filters

The joint update of states and parameters in the augmented state can lead to inconsistencies between parameters and states through the linearized analysis. Iterative filters try to reduce this inconsistency. Different approaches are compared for example by *Song et al.* [2014], on whom the following brief summary is based.

The confirming EnKF performs forecast and analysis twice for each time step. In the first analysis, only the parameters are updated. They are used for an improved rerun of the forecast. In the second analysis step, only the state is updated.

The restart EnKF is similar and updates only the parameters in a first analysis step as well. However, the new forecast for the state analysis starts at the beginning of the complete time interval considered and has to be calculated up to the current time. To save computation time, *Song et al.* [2014] additionally introduce a modified restart EnKF, where the second complete forecast is not performed by the full ensemble, but only by the mean. Afterwards, the full ensemble has to be rebuilt.

Through these iterative approaches, the consistency of states and parameters can be improved. For a synthetic case, *Song et al.* [2014] showed that the restart EnKF can provide the most accurate results. However, it requires a significantly larger computation time. Furthermore, this approach cannot consider model errors as well anymore, since the second forecast in the restart EnKF does not include state updates in between. Consequently, it is not clear if it improves the results in a real-world application, and to my knowledge, no improved results in a real-world case have been reported so far.

4 | Inflation for soil hydrology

Based on *Bauser et al.* [2018].

Inflation methods (Sect. 3.5) are used to compensate filter inbreeding in the EnKF, which is caused by a limited ensemble size and unrepresented model errors. Systematic model errors are common, for example, in land surface models [*Vereecken et al.*, 2015]. Additionally, in soil hydrology spatially and temporally varying model errors occur due to un- or ill-represented processes like preferential flow (through violation of the local equilibrium assumption in the Richards equation) or hysteresis. An insufficient ensemble spread in the augmented state, caused by these unrepresented errors, is especially severe for parameters, which are typically not changed through a forward propagation, and consequently cannot increase their uncertainty again. Due to the convergent dynamics in soil hydrology, the uncertainty in the state depends strongly on the parameter spread and can become too small as well.

All inflation methods presented in Sect. 3.5 are developed in an atmospheric sciences context. Their transfer to soil hydrology is not trivial, due to the spatiotemporally varying model errors and the typically employed augmented state. For groundwater research, *Kurtz et al.* [2012] reported improved results by employing the inflation method by *Anderson* [2007], and *Kurtz et al.* [2014] used the constant inflation by *Anderson and Anderson* [1999]. In soil hydrology however, adjusted methods of the multiplicative inflation (Sect. 3.5.2) have been used: For example, *Han et al.* [2014] and *Zhang et al.* [2017] apply a special case of the inflation method by *Whitaker and Hamill* [2012] and keep the parameter spread constant to ensure a sufficient ensemble spread. *Bauser et al.* [2016] used the method by *Anderson* [2009], but adjusted the inflation of parameters.

Instead of an inflation method, often a damping factor (Sect. 3.6.2), which can alleviate the issue, is employed. This is done by e.g, *Wu and Margulis* [2011]; *Song et al.* [2014]; *Erdal et al.* [2014]; *Brandhorst et al.* [2017]; *Botto et al.* [2018], where *Erdal et al.* [2014] and *Brandhorst et al.* [2017] combined this method with additive inflation. Alternatively, neither inflation nor damping is reported [e.g., *Li and Ren*, 2011; *Shi et al.*, 2015].

This chapter presents a novel multiplicative inflation method specifically designed for the needs in soil hydrology. The inflation method can vary rapidly in space and time to cope with the typically varying model errors and it is capable of a transfer of the inflation in the state to the parameters in the augmented state. The remainder of this chapter is organized as follows: Sect. 4.1 describes (i) the proposed inflation method and (ii) a soil hydrologic test case. Section 4.2 shows the results of my method applied to the test case, followed by a discussion in Sect. 4.3.

4.1 Method

4.1.1 Multiplicative inflation for soil hydrology

An inflation method for soil hydrology has to be able to work for spatiotemporally varying model errors and augmented states. *Anderson* [2009] already proposed a spatiotemporally adaptive multiplicative inflation by estimating a vector of inflation factors $\boldsymbol{\lambda}$ for the complete augmented state (Sect. 3.5.2). *Anderson* [2009] uses the correlation between measurements and augmented state dimensions and asks the question: *How much inflation is required in each dimension to explain the observed differences to the measurements? Anderson* [2009] showed that this works excellently for the actual state. However, I experienced possible over-inflation in parameters (which do not have any dynamics to compensate for this), which can lead to filter collapses.

To achieve a more conservative inflation method, I ask the question: *How much of the required change of the inflation am I allowed to transfer to the state dimensions based on the correlation information?* This can be achieved by applying a Kalman filter for the inflation within the EnKF.

In this Kalman filter, the inflation vector is treated as the state variable. As for parameters, I choose a constant model for the forecast in time:

$$\boldsymbol{\lambda}_{\mathrm{f},k} = \boldsymbol{\lambda}_{\mathrm{a},k-1} \,. \tag{4.1}$$

For convenience, the time subscript k is dropped in the following. Furthermore, I will use the same symbols as for the EnKF, but denote them with the subscript λ. The forecast error covariance matrix for lambda $\mathbf{P}_{\lambda,\mathrm{f}}$ is approximated based on the covariance matrix of the augmented state in the EnKF $\mathbf{P}_\mathrm{f}$ as the normalized absolute correlation matrix of the augmented state ensemble. The matrix component ij is determined as

$$\left(\mathbf{P}_{\lambda,\mathrm{f}}\right)_{ij} = \sigma_\lambda^2 \left|\left(\mathbf{P}_\mathrm{f}\right)_{ij}\right| \left[\left(\mathbf{P}_\mathrm{f}\right)_{ii}\left(\mathbf{P}_\mathrm{f}\right)_{jj}\right]^{-\frac{1}{2}} \,, \tag{4.2}$$

where σ_λ denotes the uncertainty of the inflation factors. It is a tuning parameter that is kept constant over time and is assigned to all state dimensions. It influences how fast the inflation factors are adjusted. This follows the idea by *Anderson* [2007, 2009] to avoid a closure problem, where the inflation estimation would require its own inflation. Instead, the uncertainty is kept constant. Furthermore, only the absolute value of the correlation is considered, since the inflation is based on differences between measurements and model, but ignores their direction. Note that this presumes that the correlations of the model state can be transferred to the inflation. In the presence of unknown model errors this assumption may or may not be correct. However, the estimation at measurement locations will remain meaningful in any case.

For the analysis, the distance $\boldsymbol{d}_\lambda$ between mean forecast and measurements is used as measurement for $\boldsymbol{\lambda}$:

$$\boldsymbol{d}_\lambda = \left| \boldsymbol{d} - \mathbf{H}\overline{\boldsymbol{u}^n_{\mathrm{f,inf}}} \right| . \tag{4.3}$$

The measurement error covariance matrix $\mathbf{R}_\lambda$ of $\boldsymbol{d}_\lambda$ can be calculated based on the error covariance matrices of $\boldsymbol{d}$ and $\mathbf{H}\overline{\boldsymbol{u}^n_{\mathrm{f,inf}}}$,

$$(\mathbf{R}_\lambda)_{ij} = \left| (\mathbf{R})_{ij} + \left(\mathbf{H} \left[\mathbf{P}_\mathrm{f} \circ \left[\sqrt{\boldsymbol{\lambda}_\mathrm{f}} \sqrt{\boldsymbol{\lambda}_\mathrm{f}}^T \right] \right] \mathbf{H}^T \right)_{ij} \right| , \tag{4.4}$$

where the current inflation $\boldsymbol{\lambda}_\mathrm{f}$ is already considered. The entrywise product is denoted by $\circ$ and the entrywise square root of $\boldsymbol{\lambda}$ by $\sqrt{\boldsymbol{\lambda}}$. Note that similar to *Anderson* [2007], a normal distribution is used instead of a half-normal distribution, because a positive realization of $\boldsymbol{d}_\lambda$ is given.

The expected distance between measurements and mean forecast, based on the current inflation is

$$(\boldsymbol{h}_\lambda(\boldsymbol{\lambda}_\mathrm{f}))_i = \left[(\mathbf{R}_\lambda)_{ii} \right]^{\frac{1}{2}} , \tag{4.5}$$

which combines the uncertainties of $\boldsymbol{d}$ and $\mathbf{H}\overline{\boldsymbol{u}^n_{\mathrm{f,inf}}}$. To be able to determine the Kalman gain, I first calculate the Jacobian matrix $\mathbf{H}_\lambda$ of partial derivatives of $\boldsymbol{h}_\lambda$ with respect to $\boldsymbol{\lambda}$ (Appendix A.2):

$$\begin{aligned}
(\mathbf{H}_\lambda)_{ij} &= \frac{\partial}{\partial \left(\boldsymbol{\lambda}_\mathrm{f} \right)_j} (\boldsymbol{h}_\lambda(\boldsymbol{\lambda}_\mathrm{f}))_i && (4.6)\\
&= \left[2 \left[(\boldsymbol{\lambda}_\mathrm{f})_j \right]^{\frac{1}{2}} (\boldsymbol{h}_\lambda(\boldsymbol{\lambda}_\mathrm{f}))_i \right]^{-1} \sum_m (\mathbf{H})_{ij} (\mathbf{H})_{im} (\mathbf{P}_\mathrm{f})_{jm} \left[(\boldsymbol{\lambda}_\mathrm{f})_m \right]^{\frac{1}{2}} . && (4.7)
\end{aligned}$$

With this approximated measurement operator $\mathbf{H}_\lambda$, the Kalman gain $\mathbf{K}_\lambda$ and the analysis state $\boldsymbol{\lambda}_\mathrm{a}$ are obtained as

$$\begin{aligned}
\mathbf{K}_\lambda &= \mathbf{P}_{\lambda,\mathrm{f}} \mathbf{H}_\lambda^T \left[\mathbf{H}_\lambda \mathbf{P}_{\lambda,\mathrm{f}} \mathbf{H}_\lambda^T + \mathbf{R}_\lambda \right]^{-1} , && (4.8)\\
\boldsymbol{\lambda}_\mathrm{a} &= \boldsymbol{\lambda}_\mathrm{f} + \mathbf{K}_\lambda \left[\boldsymbol{d}_\lambda - \boldsymbol{h}_\lambda(\boldsymbol{\lambda}_\mathrm{f}) \right] . && (4.9)
\end{aligned}$$

Note that the matrices $\mathbf{P}_{\lambda,\mathrm{f}}$ and $\mathbf{R}_\lambda$ can possibly become indefinite, due to the absolute value in Eq. (4.2) and Eq. (4.4). Consequently, the inverse in Eq. (4.8) could become unfeasible. However, I never encountered such a case. In a situation with uncorrelated measurements, the issue can be resolved by reducing σ_λ just for that single time step.

With this Kalman filter, the inflation vector is updated at each time step based on the difference of the mean forecast to the measurements. Following *Anderson* [2007], I additionally prohibit a deflation by constraining the inflation values to $(\boldsymbol{\lambda})_i \geq 1$.

4.1.2 Model

The proposed inflation method is tested on a small hydrologic test case. It is specifically constructed to require a strong inflation. This makes it possible to explore features of the inflation in detail on a rather short timescale. Due to a small ensemble size, the results vary depending on the seed of the random numbers.

For the test, I choose a one-dimensional case with a depth of 50 cm for a time of 6 days. A groundwater table is set as the lower boundary condition throughout the whole time. The initial condition is in hydraulic equilibrium. The upper boundary condition is no flux, except for a rain event with $2.0 \cdot 10^{-7}$ [$\mathrm{m\,s^{-1}}$] during the fourth day. For observations, I choose two water content measurements at a depth of 9.5 cm and 19.5 cm, as they would be available from TDR probes. The measurement uncertainty is set to a standard deviation of 0.007 [e.g., *Jaumann and Roth*, 2017].

For the material properties, the Mualem–van Genuchten parameters of sandy loam from *Carsel and Parrish* [1988] are chosen: $\theta_\mathrm{s} = 0.41$, $\theta_\mathrm{r} = 0.065$, $\alpha = -7.5\,\mathrm{m}^{-1}$, $n = 1.89$, $K_0 = 1.23 \cdot 10^{-5}\,\mathrm{m\,s^{-1}}$ and $\tau = 0.5$. To introduce heterogeneity, Miller scaling is used. A scaling factor of $\xi_1 = 0.32$ is chosen at the upper measurement position and $\xi_2 = 3.2$ at the lower measurement position. The scaling factors are linearly interpolated between the measurement positions and constantly extrapolated to the boundaries.

The forward simulations are performed with a spatial resolution of 1 cm. This corresponds to a state with 50 dimensions.

To test the inflation method, a perfect model experiment is performed. The EnKF estimates the water content state and four parameters (ξ_1, ξ_2, K_0, τ) through the augmented state $\boldsymbol{u} = [\boldsymbol{\theta}, \log_{10}(\xi_1), \log_{10}(\xi_2), \log_{10}(K_0), \tau]$. I choose to include the logarithm of ξ_1, ξ_2, and K_0, because they are expected to show a more linear relation to the water content state than the actual parameters. For the water content state, the correct initial condition is used as the mean with an uncertainty of 0.005. The uncertainty is spatially correlated using Eq. (3.27) with the length scale $c = 5$ cm. As initial guess for the parameters, I start with unknown heterogeneity $\log_{10}(\xi_1) = \log_{10}(\xi_2) = 0.0 \pm 0.25$, corresponding to two standard deviations away from the true values of $\log_{10}(\xi_1) = -0.5$ and $\log_{10}(\xi_2) = 0.5$. For the saturated hydraulic conductivity, I choose a too small value of $\log_{10}(K_0) = -5.5 \pm 0.5$, K_0 in [$\mathrm{m\,s^{-1}}$], which is about one standard deviation away from the true value of $\log_{10}(K_0) = -4.9$. The tortuosity $\tau = 0.5 \pm 0.5$ starts from the true value.

Through the unrepresented heterogeneity, a model error is mimicked, leading to a bias towards smaller values for the estimation of K_0 during times without dynamics, which may necessitate inflation. The parameter τ is expected to have a smaller influence, since the uncertainty is chosen small and it is already at the true value. This way, it can act as an indicator parameter for the inflation as it does not require inflation.

The EnKF is set up with a total of 25 ensemble members and damping factor, but without localization and without iterative approach. For the damping, a damping vector of $\boldsymbol{\gamma} = [\mathbf{1.0}, 0.3, 0.3, 0.3, 0.3]$ is used. It is also applied to the inflation to maintain consistency. For the uncertainty of the inflation factors, I choose $\sigma_\lambda = 1.0$.

4.2 Results

The water content state is estimated together with the four parameters ξ_1, ξ_2, K_0, and τ with the EnKF. The development of the water content at the two measurement locations at a depth of 9.5 cm and 19.5 cm is shown together with the inflation factor at these locations in Fig. 4.1. The inflation factor is applied to the forecast ensemble before the analysis. The standard deviation of the inflated ensemble should describe the distance of the estimated mean to the synthetic truth. Note that the inflation factor is not based on this distance and relies on the noisy measurements.

During the first three days without any dynamics, the uncertainty for the upper measurement is slightly underestimated, while the uncertainty in the lower measurement is slightly overestimated. This leads to an inflation factor of basically 1 for the lower measurement (factors smaller than 1 are not allowed), while the inflation factor for the upper measurement is larger. However, due to correlations between the measurement locations, a stronger inflation to fully explain the difference to the truth is prevented.

The deviation from the synthetic truth is induced through the initial guess of no heterogeneity and can also be seen in the systematic deviation of the inflated mean (which is equal to the forecast mean) from the analysis mean. When the infiltration front reaches the measurements, the deviations from the truth, the underestimation of the uncertainty, and the inflation factors increase rapidly. All of them are more pronounced for the upper measurement location. After the main peak, the differences and also the inflation factors decrease rapidly again.

The inflation factor for the state is shown in Fig. 4.2. It shows the strong increase of the inflation factor during the infiltration and its fast decrease afterwards. The inflation is strongest at the measurement location at a depth of 9.5 cm. The inflation factor is transferred to the other state locations through the correlations, which decrease with distance. Directly below the measurement locations, the inflation factors are increased less than above. This is due to the chosen interpolation of the Miller scaling factor, which reduces the correlations from the measurement locations to these state locations.

The development of the Miller scaling factors ξ_1 and ξ_2 at the two measurement positions (9.5 cm and 19.5 cm depth) is shown in Fig. 4.3a and b together with the estimated inflation factor for these parameters. Both initial conditions assume no heterogeneity and start at $\log_{10}(\xi_1) = \log_{10}(\xi_2) = 0.0 \pm 0.25$, corresponding to two standard deviations away from the true value. At the upper location the true value of $\log_{10}(\xi_1) = -0.5$ corresponds to a finer material. Consequently, the water content drops, as seen in Fig. 4.1, leading to a strong correlation with the scaling factor, and $\log_{10}(\xi_1)$ is adjusted rapidly to lower values. Accordingly, the inflation factor is increased quickly in the beginning and then reduced back to 1 when the estimation of $\log_{10}(\xi_1)$ reaches, and eventually underestimates, the true value. The underestimated

(a) Measurement at 9.5 cm depth

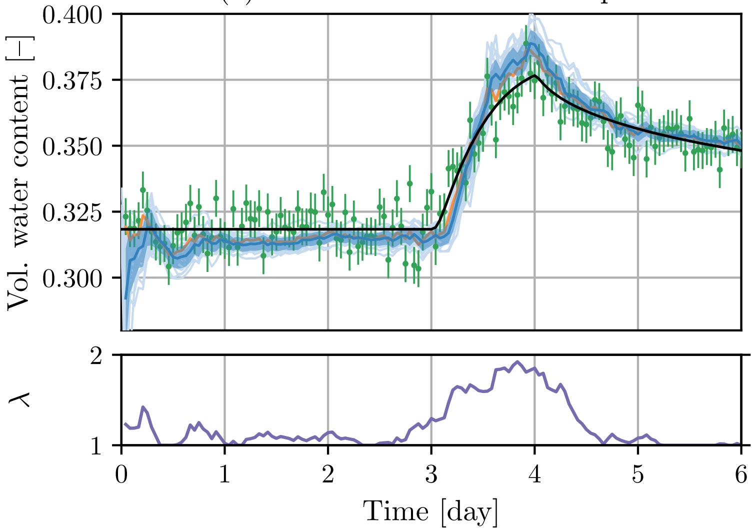

(b) Measurement at 19.5 cm depth

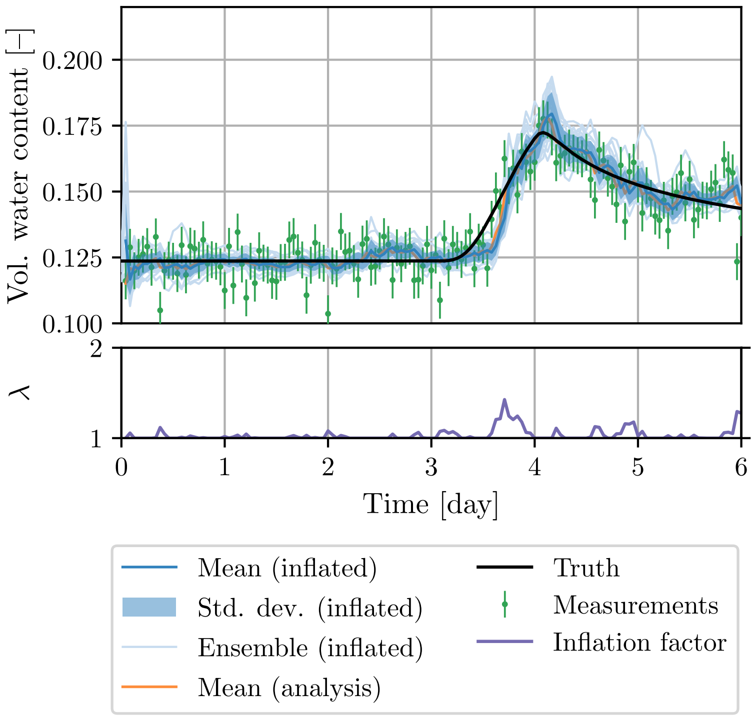

Figure 4.1: Water content estimation at the two measurement locations. The standard deviation of the inflated ensemble should be able to explain the differences between the inflated mean and the synthetic truth. The inflation factor is increased when the ensemble uncertainty is too small.

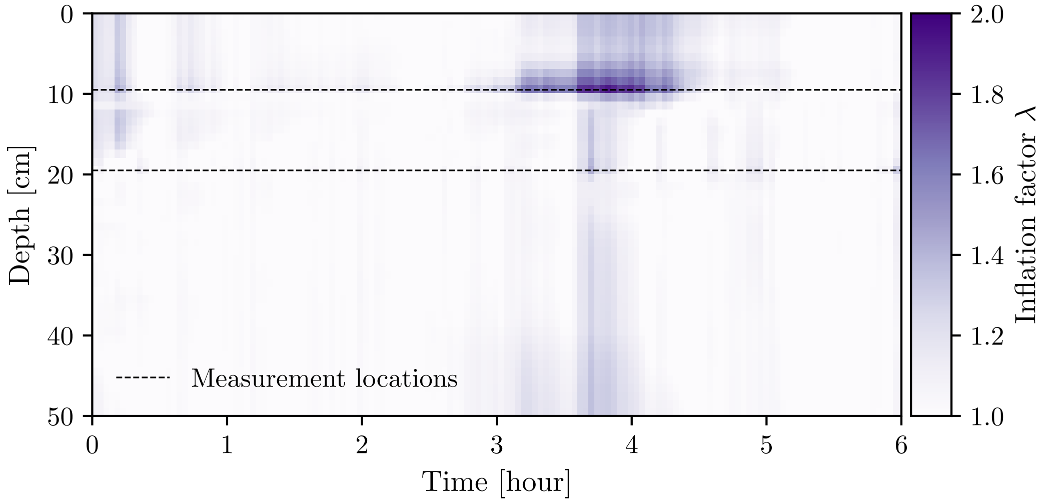

Figure 4.2: Inflation factor for the water content state. The inflation is strongest at the upper measurement location during the infiltration when the uncertainty is underestimated the most. The inflation factor is transferred to the other measurement locations through the correlations in the Kalman gain. The used interpolation of Miller scaling factors impacts these correlations and leads to the smaller inflation directly below the measurement locations.

scaling factor corresponds to a too fine material, which leads to slower changes in the water content state and therefore smaller correlations. The scaling factor is corrected during the rain event on the fourth day, which also leads to an inflation.

The initial guess for the scaling factor at the depth of 19.5 cm underestimates the scaling factor. Again, the correlations are small. The value increases slowly during the dry period in the beginning, but is inflated and adjusted strongly during the rain event.

The saturated hydraulic conductivity K_0 (Fig. 4.3c) was chosen to start a little more than one standard deviation below the true value. Due to the unrepresented heterogeneity in the beginning, the value decreases even further. The inflation remains very small due to correlations to both measurement locations. However, as soon as the infiltration event reaches the first measurement location, the value is corrected towards the true value. At the same time, the too small uncertainty causes an increase of the inflation factor. After the rain event, the inflation factor drops rapidly back to one. The hydraulic conductivity remains below the true value. Another rain event would be required to improve the estimation further.

The tortuosity τ (Fig. 4.3d) also influences the hydraulic conductivity function, but has in this case much smaller impact and consequently smaller correlations to

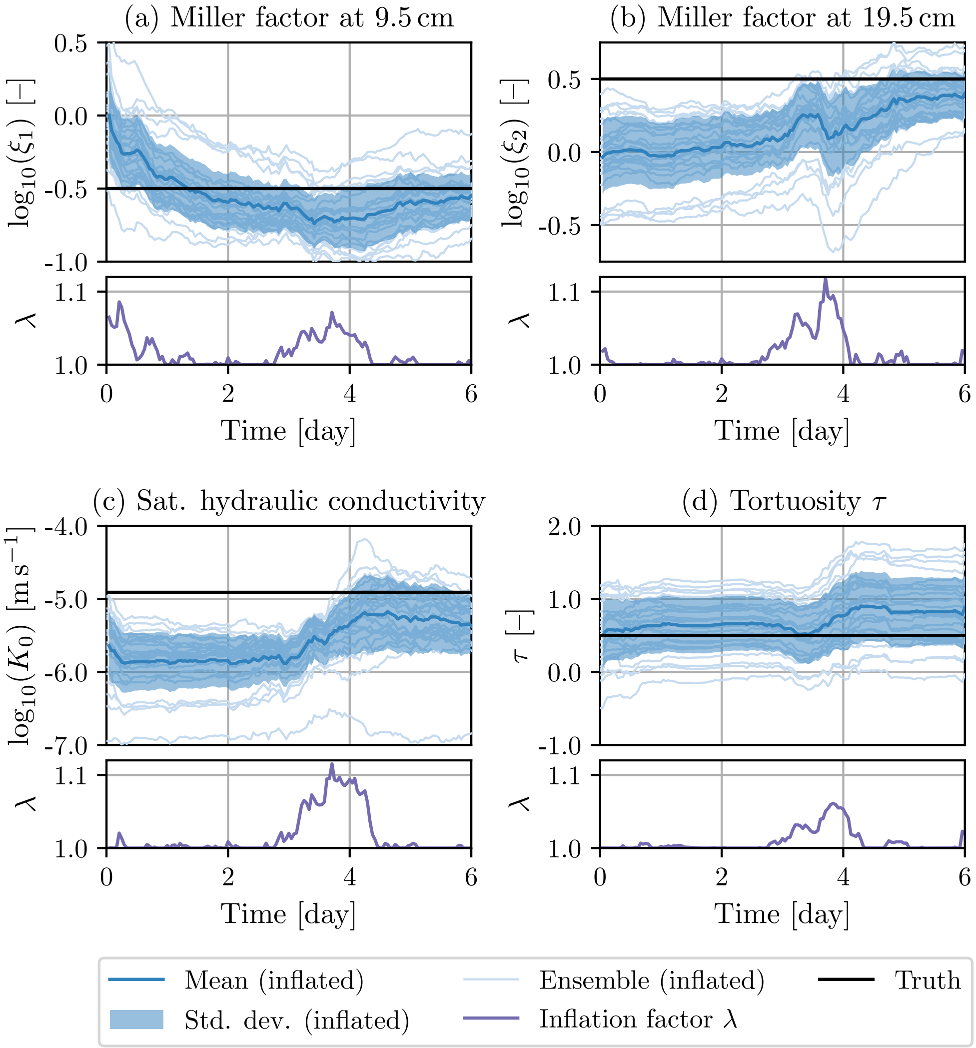

Figure 4.3: Development of Miller scaling factors ξ_1 and ξ_2, saturated hydraulic conductivity K_0, and tortuosity τ together with their corresponding inflation factors during the estimation with the EnKF.

the measurements than K_0. I use it as an indicator parameter and start at the true value. During the infiltration event, the value is changed due to its correlations. The corresponding inflation factor is increased as well, but remains small enough and drops back to 1 quickly enough to not cause any over-inflation of the parameter.

To emphasize the need of a fast adapting inflation factor, the uncertainty of the inflation factors is reduced to $\sigma_\lambda = 0.5$, to slow down their adjustment. The results are summarized in Fig. 4.4. The inflation of the water content state (Fig. 4.4a) shows that the inflation factor does not reach values as high as before (see Fig. 4.2). To compensate for this, the inflation acts over a longer period of time. The same effect is also observed in the inflation of the parameters (Fig. 4.4b and c). This leads to a smaller inflation during the rain event and consequently, a too small uncertainty. At later times, when the cause of the error is not active any more, the correlations to measurement locations are reduced, leading to a slower reduction of the inflation in the parameters. In the indicator parameter τ, the beginning of an over-inflation can be seen towards later times. This necessitates a more rapid inflation when correlations are used to update inflation information.

The results for the parameters K_0 and τ of a run without inflation (and only damping) are shown in Fig. 4.5. Again, K_0 moves further away from the true value due to the unrepresented heterogeneity and comes closer to the true value during the infiltration event. However, due to the wrong direction in the beginning, the uncertainty eventually becomes too small and in the end the mean is over 5 standard deviations away from the true value.

4.3 Summary and discussion

The proposed spatiotemporally adaptive inflation method uses a Kalman filter to estimate inflation factors within the EnKF. It is based on the difference between measurements and mean forecast state. It transfers correlations from the forecast of the augmented state in the EnKF to the inflation. Consequently, the performance will be limited if model errors are structurally not represented in the forecast error covariance matrix. The estimation of the inflation factors with a Kalman filter is, like the EnKF itself, based on a linearized analysis. The use of a damping factor can alleviate issues with estimating parameters with nonlinear relation to the measurements. To keep the inflation consistent with the analysis in the EnKF, the same damping factor is applied for both.

The inflation was explored with a small synthetic hydrologic test case. This test case mimics a model error through initially unrepresented heterogeneity. I designed the test case so that a strong temporally varying inflation is necessary, as it can occur with real data. A short time was chosen so that the details of the behavior of the inflation can be explored. The method shows that it is capable of inflating states and parameters. The inflation is adjusted fast and differentiates between parameters with strong and not so strong correlations. No over-inflation of weakly correlated parameters occurred.

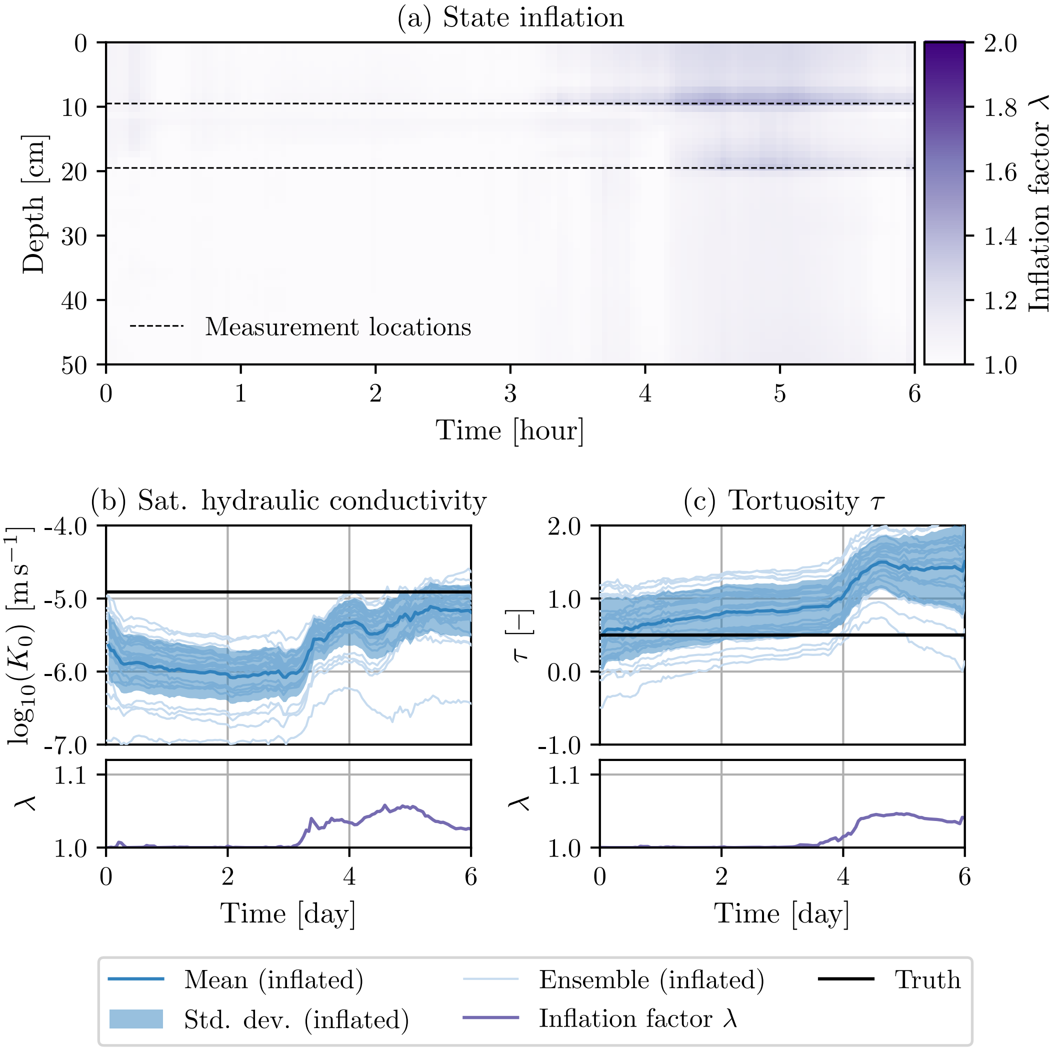

Figure 4.4: Development of the inflation factor for the water content state and saturated hydraulic conductivity K_0 and tortuosity τ together with their corresponding inflation factors for an estimation with a reduced inflation factor uncertainty of $\sigma_\lambda = 0.5$.

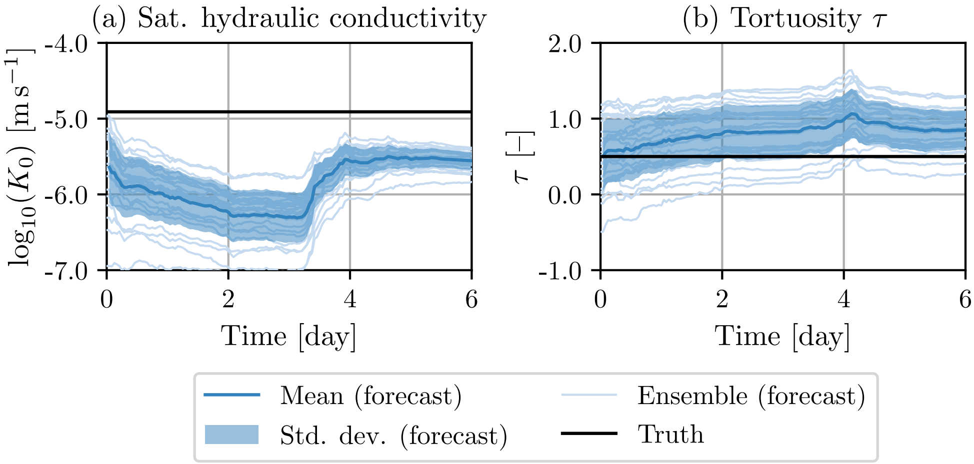

Figure 4.5: Development of saturated hydraulic conductivity K_0 and tortuosity τ for an estimation without inflation.

In this specific test case the estimation with inflation is far superior to an estimation without inflation.

The fast adjustment speed of the inflation factor is important because of the fast changing model errors and correlations to parameters. The adjustment speed is determined by the standard deviation of the inflation factor, which is set to a constant value and has to be adjusted. For all cases I explored, a value of $\sigma_\lambda = 1$ was sufficient, but larger values were possible too. The need for such a fast adjustment is shown by estimating the same case with a reduced uncertainty of $\sigma_\lambda = 0.5$, which leads to a slower adaptation of the inflation factor. This results in smaller inflation factors, which are compensated by maintaining them for a longer period of time. In this test case, this leads to inflation at times after the infiltration front has passed the measurement locations already and the model error is small again. This can cause over-inflation of weakly correlated parameters.

Fast dropping correlations between measurements and parameters are a limit for the method. An example could be a multiplicative parameter only acting on the infiltration boundary condition. After the infiltration is over, correlations to this parameter drop to zero and the inflation factor for this parameter is not changed any more. If the inflation factor is not equal to 1 at this time, the ensemble spread for this parameter will keep increasing. In such a case, when there is no correlation, the parameter should be excluded from the estimation and consequently also from the inflation.

The method is in principle capable of compensating unrepresented model errors. However, this is limited to errors that can be represented with the augmented state. If parameters are included in the estimation in the augmented state and have correlations to measurement locations with consistently underestimated forecast uncertainties, the inflation will keep increasing the parameter spread until the forecast uncertainties are increased sufficiently. This is the case when the parameters have an insufficient influence on the state uncertainty. An example are measurement uncertainties chosen too small. Then the dynamics would not be able to follow the measurement noise. A rather heuristic solution could be a decay of the inflation factor towards values of 1, as already proposed by *Anderson* [2009].

The inflation method was specifically designed for soil hydrology. It is capable of adjusting the inflation factors rapidly in space and time and proved to be stable in combination with parameters. This leads to better state and parameter estimations in soil hydrology. Nevertheless, I expect the inflation method to work in similar systems as well and to generally improve data assimilation with the EnKF.

5 | Application

In parts based on *Bauser et al.* [2016].

This chapter focuses on a real-world case to address the challenge of knowledge fusion. Section 3.1 defined knowledge fusion as the consistent aggregation of all information pertinent to some observed reality. This is exercised on a small example: a 1-D soil profile equipped with TDR probes measuring water content, during a time period of less than 2 months. For this specific situation, knowledge fusion would require the quantitatively correct description of all uncertainties in the representation and the subsequent optimal reduction of these uncertainties based on all additionally available information. For the measurement part, these are primarily the water content data from the TDR probes, but any other information, even expert knowledge, should be incorporated as well. So far, however, this goal is only partly feasible. Therefore, I focus on describing and reducing the key uncertainties with the EnKF. Nevertheless, this requires a qualitative assessment of all uncertainties.

The remainder of the chapter is organized as follows: Sect. 5.1 introduces the test site for the real-world case. The uncertainties for the representation of this specific situation and the according setup of the EnKF are described in Sect. 5.2 and Sect. 5.3. Section 5.4 introduces three stages to reduce the uncertainties: (i) improving the prior, (ii) standard EnKF and (iii) closed-eye EnKF and compares the prediction capabilities of standard and closed-eye EnKF. Sect. 5.5 discusses the results.

5.1 Test site

The Grenzhof test site is a former agricultural field located close to Heidelberg, Germany (49°25′ N, 8°37′ E). Since 2003, experiments have been conducted at the test site. In 2004, a weather station (Fig. 5.1a) was built, which measures precipitation and further atmospheric data (wind, temperature, incoming and outgoing long- and shortwave radiation, relative humidity and air temperature) in 10 min intervals. A detailed description of the test site can be found in *Wollschläger et al.* [2009].

In 2009, a soil profile was equipped with 11 TDR probes which measure water content hourly. The soil profile itself, described explicitly by *Schenk* [2011], is depicted in Fig. 5.2. It consists of four different soil layers up to the depth of 1.4 m. The top

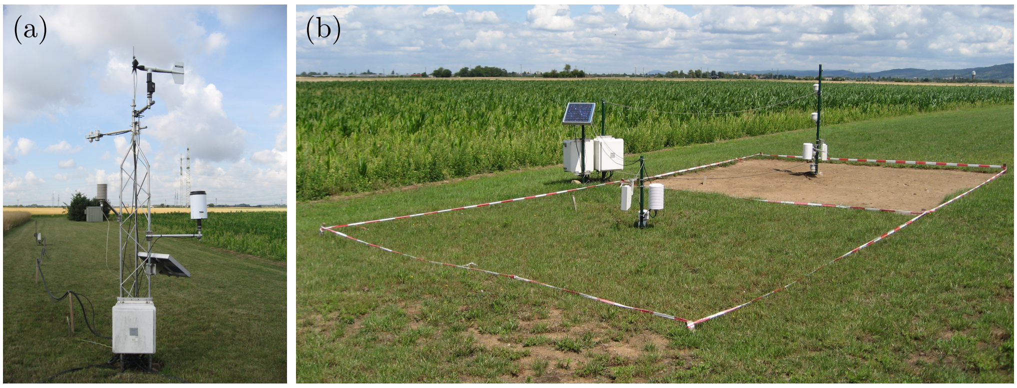

Figure 5.1: Grenzhof test site close to Heidelberg, Germany with **(a)** weather station and **(b)** water content measurements under grass and bare surface. In this work, the measurements under the bare surface are used (see Fig. 5.2).

three layers are equipped with three TDR probes each and the bottom layer with two TDR probes. The profile is kept free of vegetation at the surface (Fig. 5.1b).

The complete time period considered comprises 60 days from 1 October 2011 (day 1) until 29 November 2011 (day 60). The boundary condition, along with the water content measured by the topmost TDR, is shown in Fig. 5.3.

5.2 Representation

For this specific soil profile, I formulate the soil hydraulic representation consisting of the four components (dynamics, subscale physics, superscale physics, and response) described in chapter 2. For each I give the a priori description, as well as a qualitative assessment of the uncertainties due the corresponding assumptions.

Dynamics: The Richards equation (Eq. 2.12) describes the change of the volumetric water content. The equation itself is process-based and is expected to describe the actual physics adequately as long as its underlying assumptions are fulfilled: it assumes the soil water movement to be a single-phase process. Hence, the Richards equation is expected to fail in very dry or wet conditions. Both are not observed at the Grenzhof test site during the time period considered. The corresponding uncertainties are small. The Richards equation further assumes local equilibrium, which is assumed to be violated during strong infiltration events, e.g., during heavy rainfall leading to preferential flow. I expect local non-equilibrium at the Grenzhof test site, but it is a priori not clear how strong the forcing has to be or how to describe these cases. This creates uncertainty in the dynamics during rain events.

For this specific situation, I additionally assume that horizontal flow is negligible and that I can describe the system one-dimensionally without additional sources or

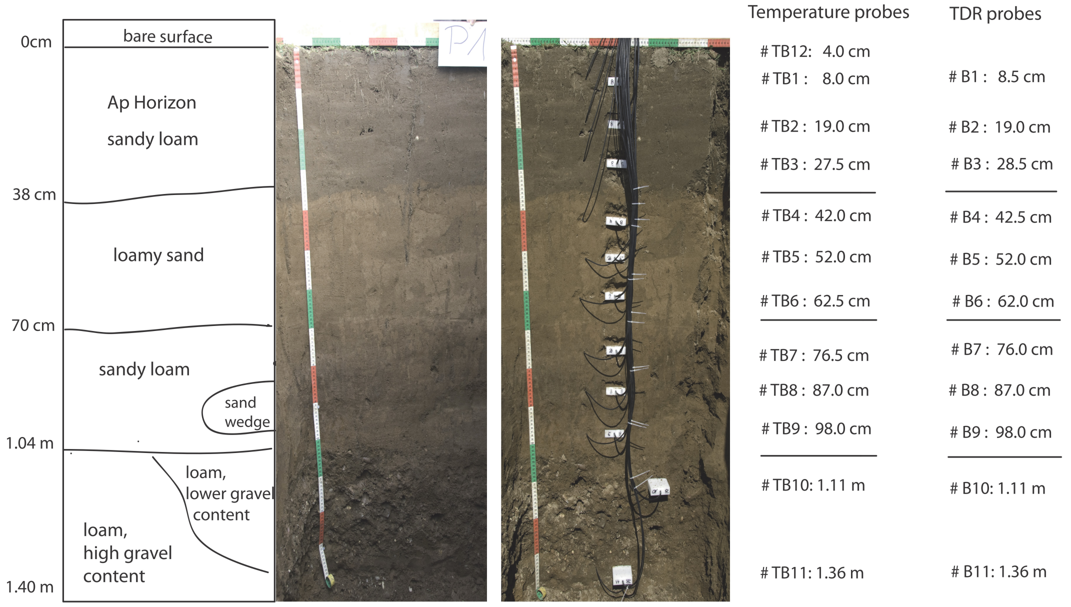

Figure 5.2: Soil profile at the Grenzhof test site [*Schenk*, 2011]. It consists of 4 different soil layers and is equipped with 12 temperature probes and 11 TDR probes. The surface is kept free of vegetation.

sinks. The flat terrain and horizontal layering at the Grenzhof test site supports this assumption. Still, heterogeneity might introduce two-dimensional flow.

Subscale physics: The Richards equation requires a description of the material properties. In this work the Mualem–van Genuchten parameterization is employed. I do not expect significant uncertainties due to assuming this particular parameterization with its specific functional forms, because the observed water contents stay in a rather small water content range.

The large-scale structure for this soil profile is made up of four soil layers. An individual parameter set is assigned to each layer. The layers were observed during the installation of the probes and corresponding uncertainties are considered small. For each of the layers, a set of parameters is required to describe the Mualem–van Genuchten parameterization. In this case, I can use the soil parameters determined by *Wollschläger et al.* [2009] through an inversion for a soil profile in close proximity. They are expected to differ from the soil hydraulic parameters at the represented soil profile due to spatial heterogeneity.

I do not include a description of hysteresis, leading to additional uncertainties connected with the parameterization. By assuming the parameters to be constant in time, wettability, density and dynamic viscosity of water are assumed constant and the soil matrix is assumed to be incompressible. Although these assumptions may

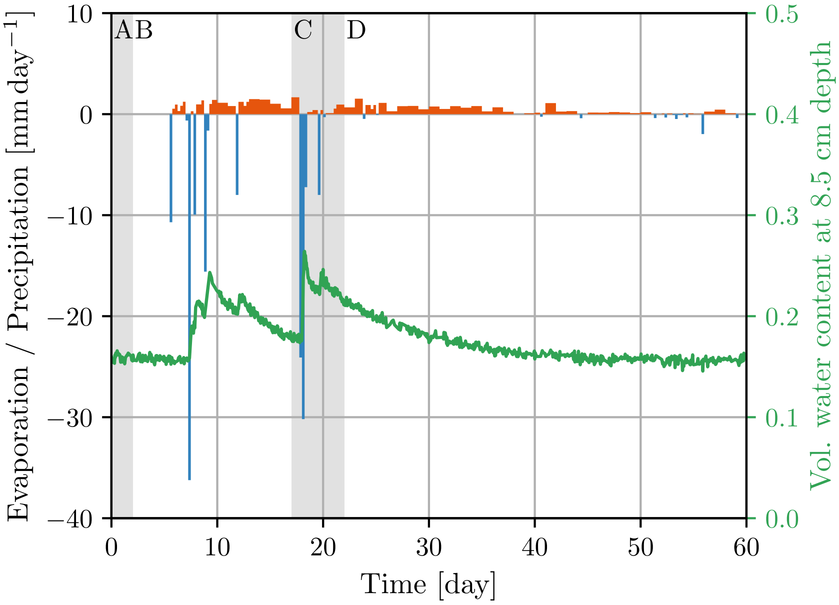

Figure 5.3: Boundary condition and topmost TDR from 1 October (day 1) until 29 November (day 60) at the Grenzhof test site. I distinguish 4 sections: A (day 1–2), B (day 3–17), C (day 18–22) and D (day 23–60). The evaporation is calculated using the reference FAO Penman–Monteith equation. Before the first rain, the evaporation is set to 0, due to a previous dry period of over a month. The precipitation is displayed with a 6 h resolution.

lead to additional uncertainties, they are justified by the short time period of less than 2 months.

The texture within the layers is described through Miller scaling. It is based on the assumption of geometric similarity, which does not necessarily hold and leads to some uncertainties. The scaling factors themselves are a priori unknown. Initially no heterogeneity (scaling factors of 1) is assumed, which is most likely wrong and introduces large uncertainties.

Superscale physics: For the upper boundary condition, the on-site weather station measures rain. Unfortunately, the rain gauge had not been calibrated during the period of consideration. Because of that, uncertainties for the precipitation are large. The further meteorological data from the weather station is used to calculate the daily mean evaporative water flux using the reference FAO Penman–Monteith equation. This estimation of the evaporation is highly uncertain. In dry conditions, the evaporation is limited by the soil, which leads to additional uncertainties. Minor moss growth was observed at the bare soil surface during the time period considered, which may influence the upper boundary condition further.

There are no measurements of the lower boundary condition at the site. However, constant water content measurements in the lowest soil layer during the observed time period indicate that the dynamics is decoupled from the groundwater table. Therefore, I follow *Wollschläger et al.* [2009] and add a fifth layer with soil parameters for sand from *Carsel and Parrish* [1988] up to a depth of 4 m in the representation. The sand layer decouples the dynamics from the groundwater table, which is kept constant at the depth of 4 m. This leads to uncertainties, which are expected to be negligible.

The initial condition is difficult to estimate. A simple approach is to use the measured water contents and interpolate them linearly with constant extrapolation to layer boundaries. This leads to large uncertainties in between.

Response: Dynamics, material properties, and forcing can be used to describe the temporal development of the states, which in this case is the water content. These states will have large uncertainties due to the uncertainties in the other components. Additionally, the assumption of local equilibrium in the Richards equation has to be met on the grid size of the numerical model as well. I choose a resolution of 1 cm. For the represented soil and boundary conditions, this resolution is sufficient to resolve the occurring fronts smoothly, so that effects caused by the numerical solver can be neglected.

Water content determined with TDR probes will be used to improve the representation. I assume an unbiased uncertainty of 0.01 for the water contents. This is the largest noise observed with the TDR probes, except for the probe in a depth of 98 cm. There the measurement noise is larger and an uncertainty of 0.015 is assumed.

The assumptions made for the representation of soil water movement at the Grenzhof test site are summarized in Table 5.1. The second column gives a qualitative assessment of the uncertainties: small – no need to represent the uncertainty explicitly; intermediate – it might be necessary to represent these uncertainties, and I decide not to but rather keep them in mind; large – uncertainties must be represented with the goal of reducing them. The findings depend on this uncertainty assessment and might be affected if it does not hold.

5.3 EnKF settings

I aim to describe and reduce the uncertainties classified as “large” in Table 5.1 with the EnKF and decided to neglect the ones classified as “intermediate” or “small”. Below, the corresponding settings of the EnKF are specified.

Uncertainties are represented and estimated directly with the EnKF, if they can be incorporated into the augmented state. I choose to include the water content state, soil hydraulic parameters, Miller scaling factors, and a scaling factor of the upper boundary condition.

Table 5.1: Prior uncertainties of the representation of soil water movement at the Grenzhof test site during October and November 2011. I assess the uncertainty caused by assumptions in a qualitative way: small – no need to represent the uncertainty explicitly; intermediate – it might be necessary to represent these uncertainties, and I decide not to but rather keep them in mind; large – uncertainties must be represented with the goal of reducing them.

Assumption	Uncertainty
Dynamics	
Single phase description (Richards equation)	small
Local equilibrium (Richards equation)	small–large
1-D, no sources and sinks	intermediate
Material properties	
Mualem–van Genuchten parameterization for material properties	small
Mualem–van Genuchten parameter values from *Wollschläger et al.* [2009]	large
Mualem–van Genuchten parameters constant in time	small
No hysteresis	intermediate
Large-scale architecture described with layers	small
Small-scale architecture described with Miller scaling	intermediate
Miller scaling factors are 1	large
Forcing	
Upper boundary condition from rain gauge and FAO Penman–Monteith equation	large
Lower boundary condition constant groundwater table decoupled with soil layer	small
Linear interpolation for initial condition	large
Response	
Numerical representation	small
Water content measurements without biases and uncertainty of 0.01 (or 0.015 respectively)	intermediate

Adding components to the augmented state increases its dimension, which in turn requires a larger number of ensemble members and leads to a higher computational effort. To minimize this effect, I keep the added components as small as possible.

Regarding the parameters to be incorporated, I choose α, n, and K_0 for each of the four layers as well as the saturated water content θ_s for layers 3 and 4. For the upper two layers, the measured water contents were far away from θ_s and θ_r estimated by *Wollschläger et al.* [2009]. Thus, they are irrelevant for the estimation, as changes in θ_s and θ_r can be compensated by the other parameters. For the bottom two layers, measurements exceeded θ_s. Thus, it has to be added in the augmented state. I do not include the tortuosity τ, since the observed water content ranges are rather small. For other situations however, incorporation of τ might improve the results. Since the EnKF assumes Gaussian distributions and linear correlations, I do not directly use K_0 and instead use the logarithm (to which the water content response behaves more linearly).

The dimensions of the Miller scaling factors are reduced as well. Only the scaling factors at measurement locations are added. The whole Miller scaling field is determined by linear interpolation between measurement locations inside a layer and a constant extrapolation towards layer boundaries. As the measurements yield only little information about the small-scale architecture away from their location, I expect that this assumption has only a slight influence on the results. Again, the logarithm of the parameter is used in the augmented state. The linear interpolation is performed in the logarithm space as well.

The upper boundary condition is not incorporated directly into the augmented state, but added as a scaling factor of the boundary condition.

The expansion to an augmented state changes the propagation in time. Each component requires an individual forward propagation. I assume the soil hydraulic parameters and Miller scaling factors to be constant in time. This is not possible for the scaling factor of the upper boundary condition, which can change over time. Therefore, it is assumed to be piecewise constant. The forward model switches the parameter about daily and at transitions between precipitation and evaporation. This means that a set of scaling factors is estimated, where the estimation of each scaling factor is restricted to a short time interval. The estimation of the boundary condition ensures that there is no global bias on the parameter estimation during the rain event.

Uncertainties, that are not explicitly represented, should be incorporated into the process noise $\boldsymbol{\eta}$, which is difficult to quantify, however. I set the process noise of all augmented state components to 0.

With this choice of augmented state and process noise, I represent and reduce all uncertainties classified as “large” in Table 5.1 directly, except for uncertainties caused by the local equilibrium assumption, which is expected to only hold outside of strong rain events. I decided to not represent “intermediate” and “small” uncertainties.

The inflation method presented in chapter 4 is employed to account for the effect of spurious correlations and the unrepresented uncertainties. Here, this is mainly the uncertainties from the local equilibrium assumption. The uncertainty of the inflation factors itself, which determines how fast it is adjusted, is chosen in accordance with chapter 4 with $\sigma_\lambda = 1.0$.

Localization (Sect. 3.4) is used to reduce spurious correlations. For the water content state, the covariances are reduced with increasing physical distance with Eq. (3.27), with a very large empirical value of $c = 75\,\mathrm{cm}$ for the length scale. The soil parameters are localized more strongly by only allowing covariances (entries of 1) between parameters and measurement locations in the respective soil layer and the first measurement locations in the neighboring layers. For the Miller scaling factors, only covariances to the corresponding measurement locations are kept, and for the scaling factor of the boundary condition only the measurements in the uppermost layer are used. All other entries are set to 0.

A damping factor (Sect. 3.6.2) is used to reduce the impact of the linearization of nonlinear dependencies. The value of the factors is a tuning parameter. *Hendricks Franssen and Kinzelbach* [2008] investigated damping factors between 0.1 and 1.0, while *Erdal et al.* [2014] employed a damping factor of 0.3 for the parameters. The smaller the value, the better a nonlinearity can be handled, but the slower the estimated value approaches the optimal value. I choose $\boldsymbol{\gamma} = [\gamma_\theta, \gamma_\varphi, \gamma_\xi, \gamma_\mathrm{bc}] = [\mathbf{1.0}, \mathbf{0.1}, \mathbf{0.1}, \mathbf{0.1}]$. This means that, based on the water content measurements, there is no damping for the update of the water content state, but a strong damping for soil hydraulic parameters, Miller scaling factors and upper boundary condition.

I additionally iterate the whole EnKF scheme and start the next iteration with the final estimation of soil parameters, Miller scaling factors and scaling factors of the upper boundary condition of the previous iteration. These iterations differ from the typically applied iterative EnKFs presented in Sect. 3.6.3. The full iterations are required to estimate constant augmented state components even with a small damping factor and a rather short time period of data. This is especially important for the upper boundary condition, where the time periods for each scaling factor are short.

The operational assumptions of the method lead to a sub-optimal estimation of the state in each time step. Furthermore, due to the nonlinear dynamics, the assumption of Gaussian distributions does not hold. It is not clear how this affects the EnKF performance in detail. The Gaussian assumption leads to a linearized state update in the analysis step. This induces erroneous updates of those augmented state components with dominant nonlinear relation between augmented states and measurements. These errors are alleviated by employing the damping factor, which reduces the update but as a consequence also reduces the incorporation of measurement information. Furthermore, I use the largest observed measurement noise to characterize the TDR uncertainties. This leads to possibly too-large measurement uncertainties, which have a similar effect as an additional damping factor.

I do not expect a strong influence from this sub-optimal state estimation on the mean value of the results for the soil hydraulic parameters, Miller scaling factors and scaling factor of the upper boundary condition. However, the final value will be approached more slowly than in an ideal estimation. This effect is handled by the iterative approach.

On the downside, incorporating the same measurement information several times will lead, together with the other limitations, to incorrect quantitative uncertainties. However, the inflation method ensures that measurements and states agree with each other within their uncertainties. This is only a partial solution, however, as the information is only propagated through the correlations to the measurement locations. Therefore, I will not interpret the uncertainties of the ensemble in a quantitative way. Nevertheless, I do expect them to hold qualitative information that can be interpreted.

5.4 Results

The complete time period considered comprises 60 days and ranges from 1 October (day 1) until 29 November (day 60). The boundary condition, along with the water content measured by the topmost TDR, is shown in Fig. 5.3. The whole time period is separated into four sections: A (day 1–2), B (3–17), C (18–22), and D (23–60).

Since soil parameters can only be estimated within the observed water content range and will not be valid outside of this range, a rather large rain event is desirable. On the other hand I do not represent uncertainties associated with the assumption of local equilibrium by the Richards equation, which is violated during strong rain events. Time period C (18–22 October 2011) combines both: a rather large total rain amount (18.2 mm) and a small maximal intensity (0.7 mm in 10 min).

I designed a three-stage approach (Fig. 5.4) to improve the representation by incorporating the information from the water content measurements of the 11 TDR probes: (i) improving the prior information during time periods A and B, (ii) a standard EnKF approach, and (iii) a closed-eye EnKF approach, both during time period C with the considered rain event. The three stages are discussed in the following sections, with results analyzed through forecasts in time periods B, C, and D.

5.4.1 Stage 1: improving the prior

Highly uncertain properties can exacerbate the performance of the EnKF. For example, *Huber et al.* [2011] showed that the state estimation with an EnKF is superior in case of properly precalibrated model parameters. For the representation at Grenzhof, there is no prior knowledge about small-scale heterogeneity, which can lead to difficulties in the estimation process: in a uniform layer, the water content is typically higher in deeper locations. Heterogeneity can reverse this and can lead to higher water contents above lower water contents inside a layer. Until the infiltration front of the rain event reaches these positions, the EnKF cannot distinguish between heterogeneity and an infiltration front propagating at very low speed. This can easily lead to too-small saturated conductivities, especially in lower soil layers that are not reached by the infiltration front. Even upper layers can require a tuned relation of the prior uncertainties of Miller scaling factors and saturated conductivity.

To avoid too-small saturated conductivities, I improve the prior of the heterogeneity using the measurements from time interval *A*. Prior to *A*, there had been 1 month

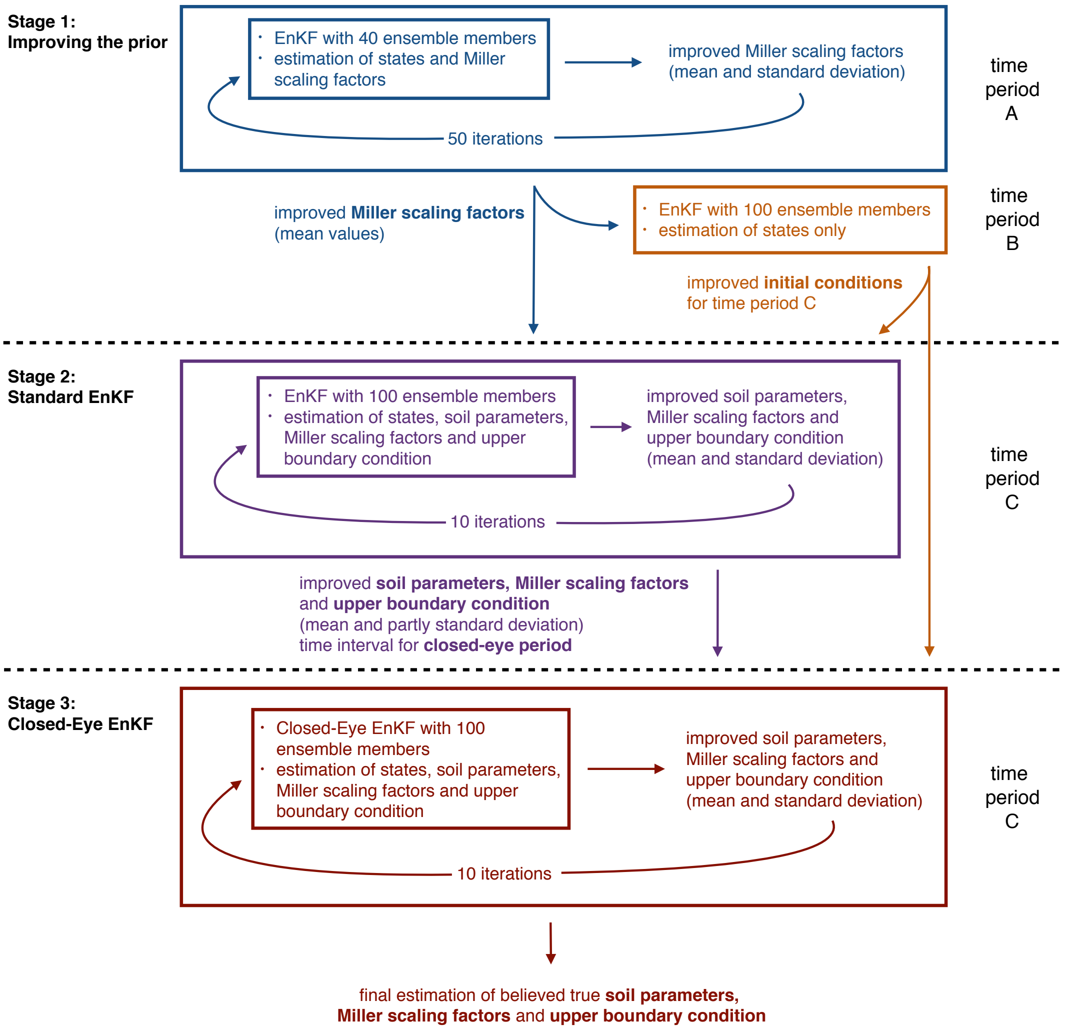

Figure 5.4: Block diagram illustrating the three-stage approach. The different time periods are shown in Fig. 5.3.

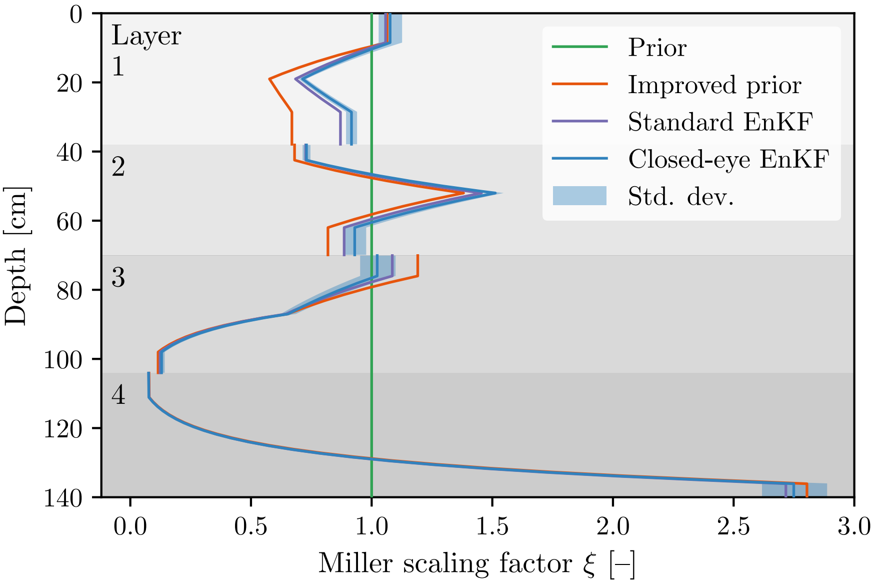

Figure 5.5: Mean values of the Miller scaling field. Soil layers are indicated by different gray scales. The heterogeneity is a priori unknown and the according prior is set to 1. The logarithm of the scaling factors is estimated at the measurement locations and interpolated linearly between (with constant extrapolation to layer boundaries). Already the improved prior can describe the main features. The further estimations with the standard and closed-eye EnKF lead to further small changes mainly in the first layer. For the closed-eye EnKF the standard deviation of the ensemble indicating the uncertainties is additionally shown.

without rainfall leading to little dynamics during A. I start with the soil parameters estimated by *Wollschläger et al.* [2009] and linearly interpolated initial condition (with constant extrapolation to layer boundaries). Parameters and boundary condition are kept constant, but states and Miller scaling factors are updated with an EnKF of 40 ensemble members, where the initial uncertainty of the logarithm of the scaling factors was chosen to be 0.2.

As time interval A is only a 2-day period, the filter is not able to reach constant Miller scaling values during this short time. Therefore, I iterate 50 times over this period, which then does lead to constant scaling factors. The resulting scaling field of the improved prior (Fig. 5.5) shows that there is heterogeneity within each layer that requires a representation. Layer 4 in particular exhibits a strong heterogeneity, which is already observable in Fig. 5.2.

Additionally, a good initial state can improve the estimation. Therefore, I guide the state with an EnKF (only state estimation) with 100 ensemble members through time period B, and achieve a better representation for the initial state for time period C

Table 5.2: Soil hydraulic parameters as estimated by *Wollschläger et al.* [2009] and the initial uncertainties for the standard EnKF.

Layer	α $[\mathrm{m}^{-1}]$	$\log_{10}(K_0)$ $[\mathrm{m\,s}^{-1}]$	n	θ_s	θ_r	τ
1	-4.8 ± 2.0	-4.6 ± 1.0	1.61 ± 0.20	0.39	0.020	0.5
2	-11.0 ± 2.0	-5.3 ± 1.0	1.80 ± 0.20	0.40	0.070	0.5
3	-7.4 ± 2.0	-6.0 ± 1.0	1.43 ± 0.20	0.40 ± 0.02	0.090	0.5
4	-2.9 ± 2.0	-5.4 ± 1.0	1.36 ± 0.10	0.41 ± 0.02	0.100	0.5
5	-14.5	-4.1	2.68	0.43	0.045	0.5

Parameters without uncertainty are not included in the augmented state and are not estimated. The saturated water contents θ_s of the layers 3 and 4 were already estimated during the prior estimation in time period A, because measurement values exceeded the value of 0.36 determined by *Wollschläger et al.* [2009].

than interpolating between the measurements there.

5.4.2 Stage 2: standard EnKF

During time period C, I improve the representation with the following uncertain components: improved initial condition, soil hydraulic parameters estimated by *Wollschläger et al.* [2009], improved Miller scaling factors, and scaling factor of 1 of the upper boundary condition from precipitation measurements and estimated with the reference FAO Penman–Monteith equation. I improve soil parameters, Miller scaling factors, and upper boundary condition along with the states. The estimated mean values and standard deviations of soil parameters, Miller scaling factors, and scaling factor of the upper boundary condition are used to generate the ensemble for the next iterations. The initial condition is kept the same. I iterate 10 times over time period C. This estimation is performed with an ensemble size of 100 members and will be referred to as the standard EnKF.

The initial ensembles of initial condition and Miller scaling are determined as described in stage 1. For the Miller scaling factors the uncertainty is increased again compared to the estimations in the prior, since they were estimated under the assumption of fixed soil parameters. Now, they have to be able to adapt to changing parameters. The uncertainty of the logarithm of the scaling factors is chosen to be 0.05. For the scaling factor of the boundary condition shown in Fig. 5.3, an uncertainty of 20 % is assumed. The initial soil hydraulic parameters and their uncertainties are summarized in Table 5.2.

In order to check the improved results, I do not show the states from the last iteration but actually run another iteration, however, this time without incorporating the measurement information. This corresponds to an ensemble of forward runs during time period C. It is a much more strict test for the quality and objectivity of the

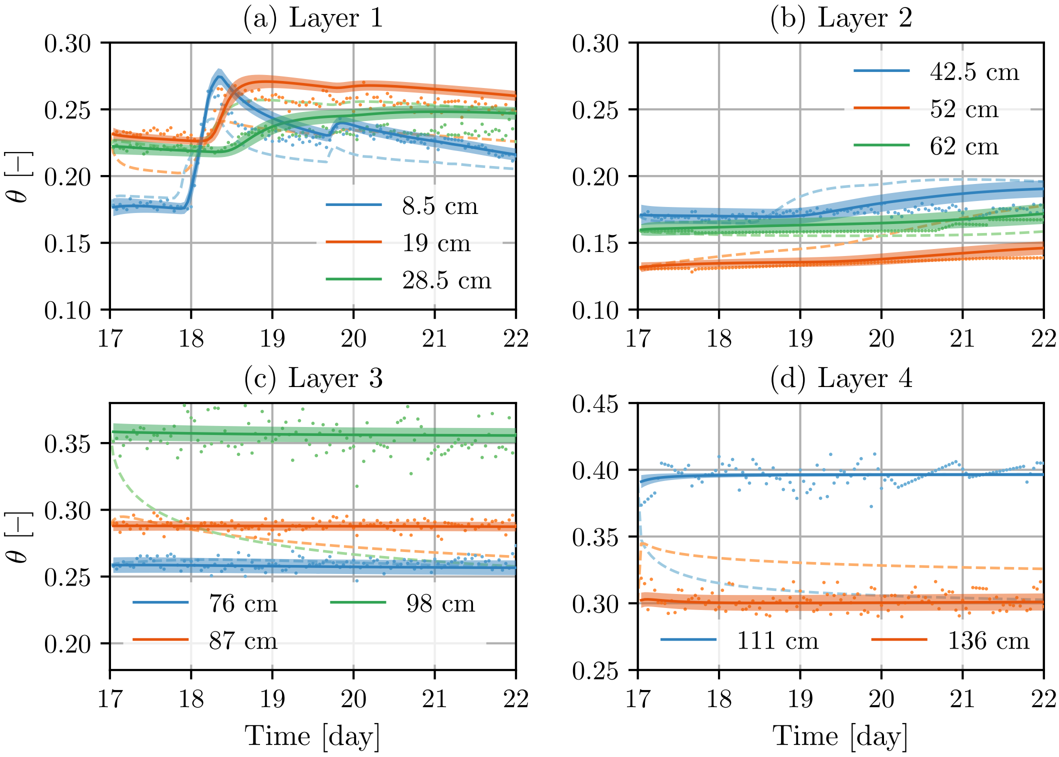

Figure 5.6: Forecast at the measurement positions of the four different layers during time period C. The solid lines show mean and standard deviation of a total of 100 different forecasts, with soil parameters, Miller scaling parameters, and boundary condition sampled from the distributions estimated with the standard EnKF and the initial condition, which was actually used for the estimation itself. The dashed lines show results from the original soil parameters by *Wollschläger et al.* [2009]. The dots show the measurements, which were recorded hourly. Occurring data gaps were interpolated linearly.

Table 5.3: Results for the soil hydraulic parameters estimated with the standard EnKF.

Layer	α [m^{-1}]	$\log_{10}(K_0)$ [$\mathrm{m\,s}^{-1}$]	n	θ_s	θ_r	τ
1	-5.0 ± 0.3	-5.21 ± 0.05	1.46 ± 0.02	0.39	0.02	0.5
2	-11.0 ± 0.8	-4.37 ± 0.17	1.70 ± 0.03	0.40	0.07	0.5
3	-8.1 ± 1.1	-6.72 ± 0.29	1.38 ± 0.02	0.39 ± 0.01	0.09	0.5
4	-2.2 ± 0.4	-5.93 ± 0.32	1.34 ± 0.02	0.40 ± 0.01	0.10	0.5

Parameters without uncertainty are not included in the augmented state and are consequently not estimated.

assimilation, because the states now cannot be adjusted. In fact, allowing incorporation of measurements leads to a much better agreement with the measurements. The results for all four layers are shown in Fig. 5.6. The graphs show that the measurements can be represented well by the ensemble, but deviations occur, mainly during the infiltration.

There is heterogeneity inside the layers. For example, in the first layer, the middle TDR shows the highest water content. This effect is strongest in layer 4. Here, the water content of the TDR about 25 cm above the next has a water content almost 0.1 larger. The results calculated with soil parameters by *Wollschläger et al.* [2009] with the assumption of homogeneous soil layers are not able to describe the measured water content.

The results for the estimated Miller scaling factors are shown in Fig. 5.5. The Miller scaling factors were adjusted along with the hydraulic parameters during this standard EnKF approach. This is necessary, because changing parameters require adjusted Miller scaling factors as well. The largest changes occur in layer 1, where information is introduced by the water content changes during the infiltration.

The estimated soil parameters, including their uncertainties, are summarized in Table 5.3. Although the uncertainties are quantitatively incorrect, they still indicate how much information about each parameter is in the measurements. This can be seen especially well for K_0. The estimation of K_0 requires dynamics. Therefore, the smallest uncertainty is observed in layer 1 and increases with the layers. In layer 4 the uncertainty of $\log_{10}(K_0)$ was reduced least, but still from 1.0 to 0.32. This shows the difficulties of the EnKF and the necessity of inflation methods. As no change in water content was observed, it is unlikely that any flux was introduced during the rain event. Nevertheless, the uncertainty was reduced, which can lead to difficulties when there actually is information.

The development of the parameters K_0, α, and n of the first layer are shown in Fig. 5.7. Towards later iterations, all three show the same feature: the value increases during the rain event and decreases before and after, but does not change significantly between initial and final values. Since I added the boundary condition into the estimation, effects due to a bias in the precipitation to cause this parameter shift can be

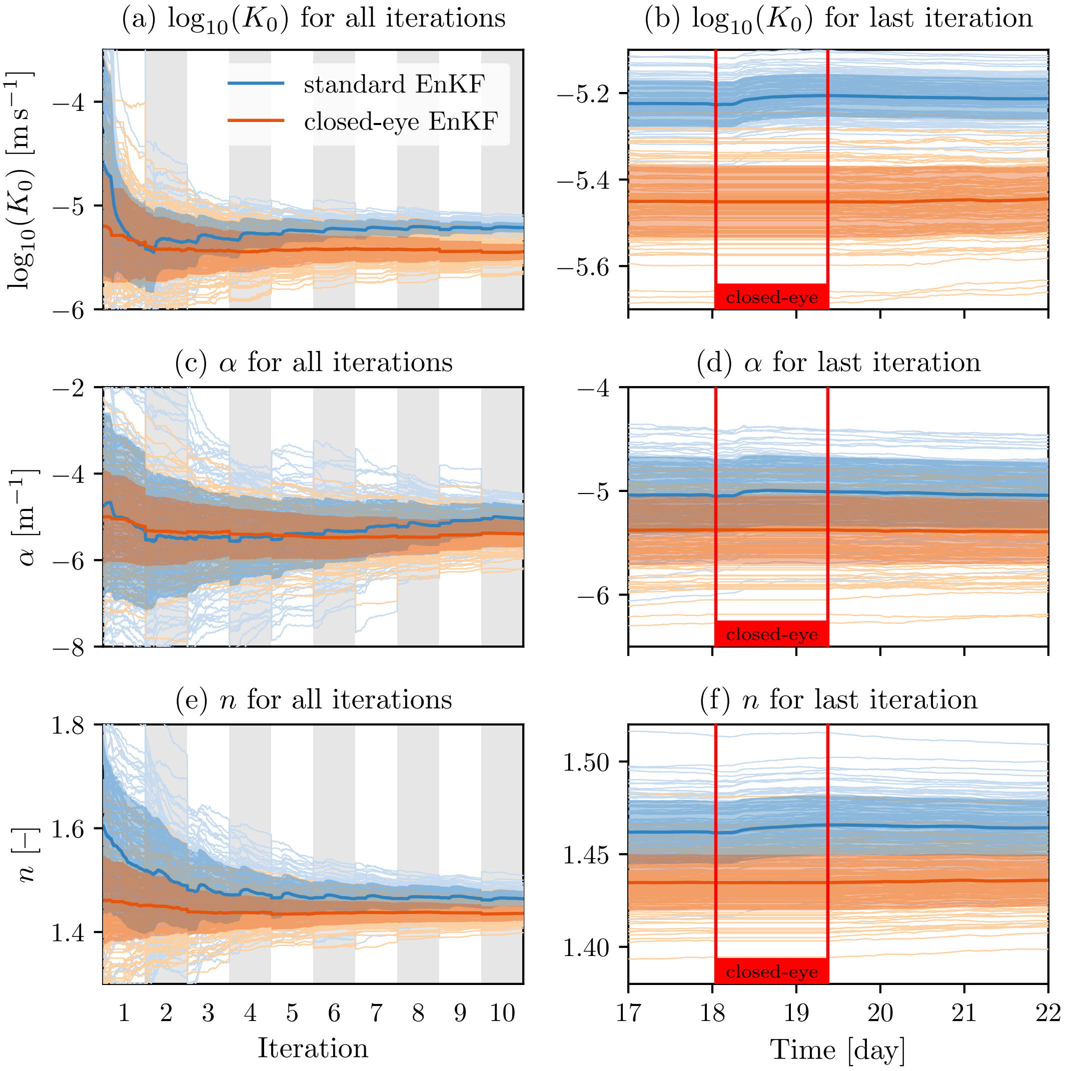

Figure 5.7: Development of mean, standard deviation, and ensemble of the parameters K_0, α, and n of the first layer during the estimation with standard EnKF and the closed-eye EnKF for all iterations **(a, c, e)** and the last iteration **(b, d, f)**.

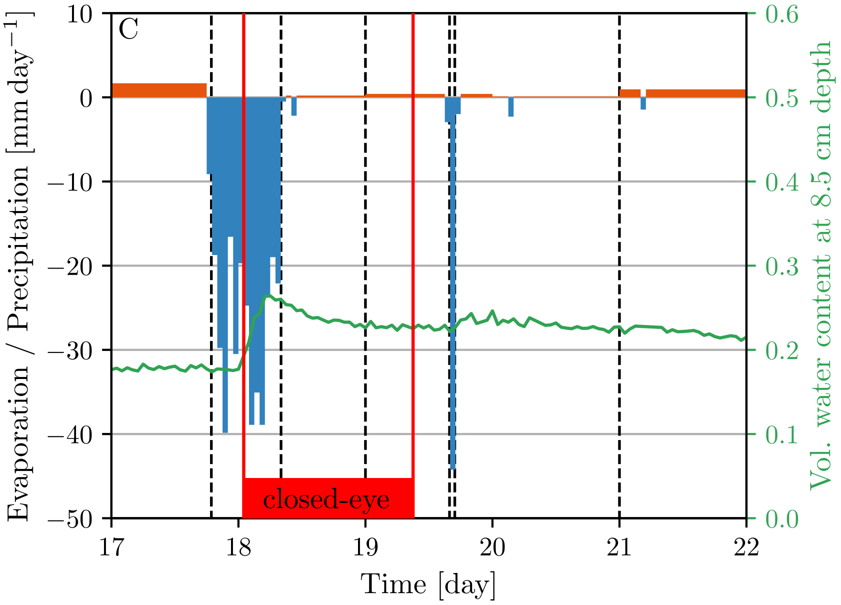

Figure 5.8: Boundary condition along with the topmost TDR water content measurements during time period C. The closed-eye time period was determined based on the changes in parameter K_0 (Fig. 5.7). During this time the dynamics cannot describe the water content measurements any more, most likely because of the violation of the local equilibrium assumption. The dashed, vertical lines indicate the time intervals for the scaling factor of the boundary condition. During each interval an individual factor is estimated.

excluded.

I interpret the parameter shift during the rain event as follows: the assumption of local equilibrium during the rain event is wrong, which leads to preferential flow. The infiltration is thus too fast for the actual parameters (Fig. 5.6). The preferential flow leads to an apparent increase in the saturated hydraulic conductivity during the rain event, which is reduced again afterwards.

The apparent increase of the parameters starts slow at around day 18 and becomes stronger a few hours later. This detail is in agreement with the assumed violation of the local equilibrium assumption. Preferential flow requires local saturation to set in. In the beginning of the rain event, the soil is at a more negative matric head and is capable of a stronger water uptake. Additionally, the rain intensity is smaller during the first 2 hours (Fig. 5.8) and can be further decreased through interception by the moss at the surface. The strongest apparent increase of the parameters occurs, when the infiltration reaches the second measurement location only a short time after it has reached the topmost measurement.

The observed preferential flow is not represented in the dynamics. This shows that

Table 5.4: Results for the soil hydraulic parameters estimated with the closed-eye EnKF.

Layer	α [m^{-1}]	$\log_{10}(K_0)$ [$\mathrm{m\,s}^{-1}$]	n	θ_s	θ_r	τ
1	-5.4 ± 0.3	-5.44 ± 0.08	1.44 ± 0.01	0.39	0.02	0.5
2	-11.0 ± 0.5	-4.31 ± 0.07	1.69 ± 0.01	0.40	0.07	0.5
3	-8.3 ± 0.7	-6.76 ± 0.18	1.37 ± 0.01	0.38 ± 0.01	0.09	0.5
4	-2.1 ± 0.3	-5.89 ± 0.18	1.33 ± 0.01	0.40 ± 0.01	0.10	0.5

Parameters without uncertainty are not included in the augmented state and are consequently not estimated.

the initial assumption of zero process noise is wrong. The uncertainty introduced by the dynamics is not represented.

5.4.3 Stage 3: closed-eye EnKF

The EnKF is enhanced with a closed-eye period during times when the local equilibrium assumption of the Richards equation does not hold. During this time, soil hydraulic parameters and Miller scaling factors are not adjusted but kept constant. In contrast, the water content state is continuously updated. In this way, the state is guided on the basis of measurements through times with uncertain dynamics without incorporating the dynamics uncertainties into the parameter estimation. The estimation of soil hydraulic parameters is only performed before and after this closed-eye period.

I use an identified non-constant parameter to define the closed-eye period. I choose K_0, because it shows the changes in the parameter value most prominently and it can be directly related to observed physics. The closed-eye period is defined as the time period between the minimum and the maximum value of K_0 during the last iteration with the standard EnKF. It begins at the same time as the infiltration front reaches the first measurement location (Fig. 5.8).

To perform the closed-eye EnKF estimation, I add another 10 iterations to the previous standard EnKF iterations, but with the closed-eye period for the first layer. I continue with the previously estimated mean values, but increase the uncertainty for the first layer again (to half the initial uncertainty) to allow the new values to deviate from the standard EnKF results. The closed-eye period is not applied to the layers 2 to 4, since no significant deviations to the measurements and no preferential flow occurred there.

The additional iterations result in new soil parameters and Miller scaling factors. The Miller scaling factors changed only marginally compared to their regular estimates (Fig. 5.5). Changes in the parameters of the first layer are larger (Fig. 5.7). Two features can be recognized: first, the values differ from each other. For n and α the changes are rather small, but for K_0 the difference is significant. The closed-eye

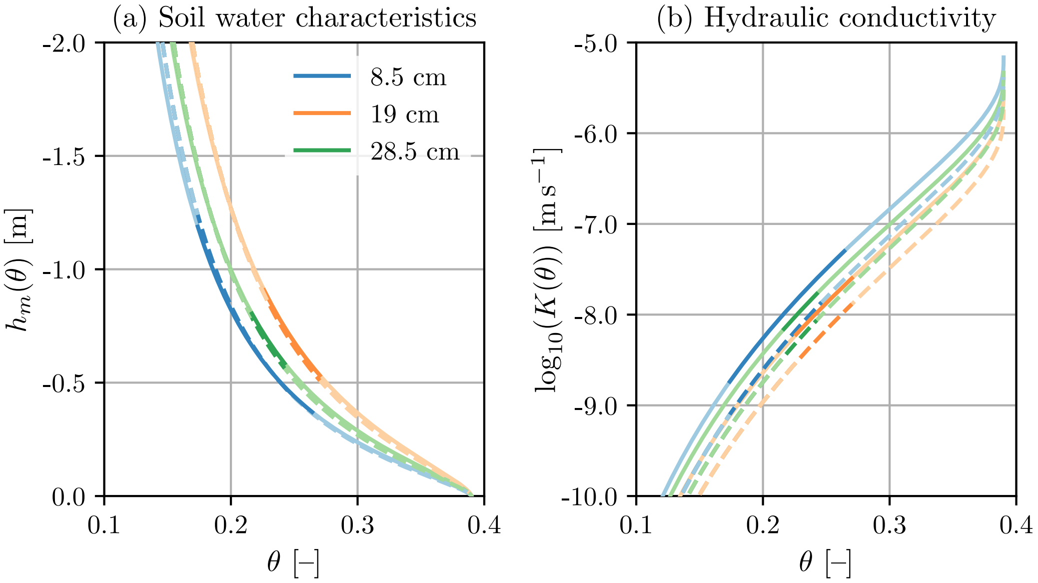

Figure 5.9: Material properties at the three measurement locations in the first layer for the soil hydraulic parameters and Miller scaling factors estimated with the standard EnKF (solid lines) and closed-eye EnKF (dashed lines). The dark colors indicated the observed water content range during the estimation at each location, for which the estimated material properties are deemed valid.

estimation yields approximately half the hydraulic conductivity as before. Second, the parameters now are constant over time and do not show fluctuations any more.

This indicates that it was possible to extract times when the Richards equation is actually valid and to determine soil hydraulic parameters that resemble the believed true material properties. This means, I believe, that if the parameters are constant in time, the parameters can represent reality in the observed water content range during times when the underlying assumptions hold. There is an apparent downside, though. The measurements during the closed-eye period cannot be used to estimate the parameters. This leads to a smaller observed water content range, limiting the parameter estimation possibilities. I call this “apparent”, because the corresponding interval does not contain valid information about the modeled system in the first place.

As a related aspect, the estimation of the scaling factor of the upper boundary condition is not meaningful during the closed-eye period any more. Consequently only an estimation of the evaporation before and after the rain event is possible. Due to the short time interval and small evaporation flux, in this case the effect is negligible.

The soil hydraulic parameters estimated with the closed-eye EnKF are summarized in Table 5.4. The changes for mean values estimated for the layers 2 to 4 are small compared to the standard EnKF (Table 5.3). However, the uncertainties are

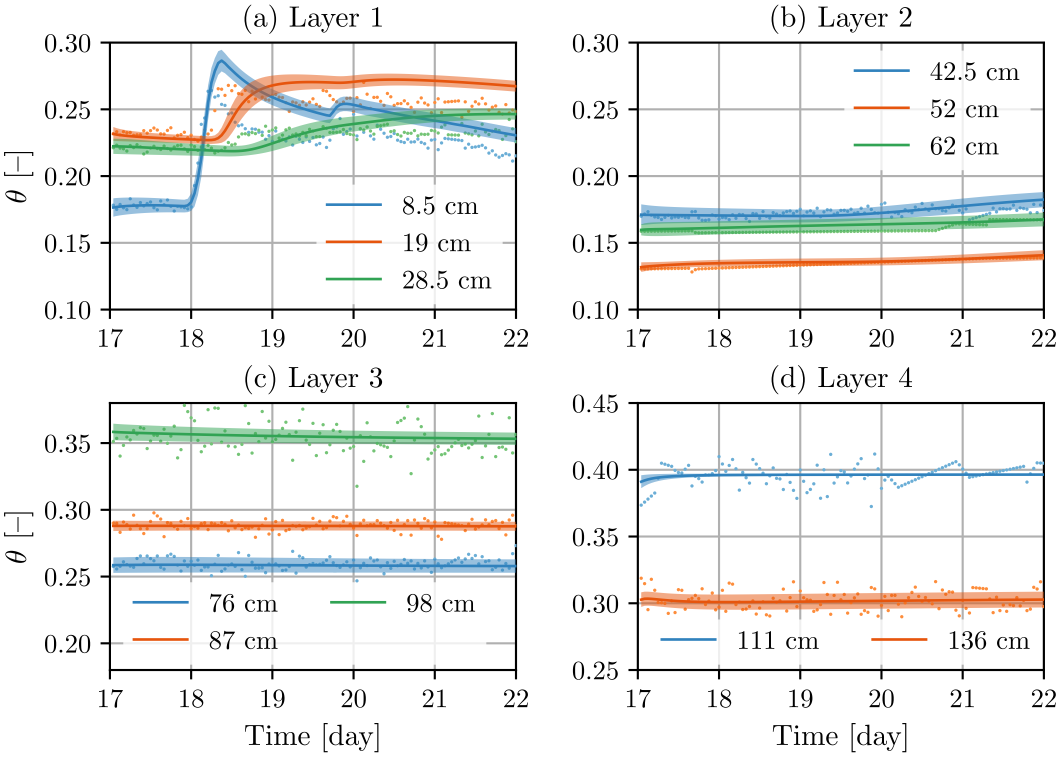

Figure 5.10: Forecast at the measurement positions of the four different layers during time period C with the results from the closed-eye EnKF. The solid lines show mean and standard deviation of a total of 100 different forecasts, with soil parameters, Miller scaling parameters, and boundary condition sampled from the distributions estimated with the closed-eye EnKF and the initial condition, which was actually used for the estimation itself. The dots show the measurements, which were recorded hourly. Occurring data gaps were interpolated linearly.

reduced further. For the first layer, the resulting material properties from soil hydraulic parameters and Miller scaling factors at the three measurement locations for the standard EnKF and the closed-eye EnKF are shown in Fig. 5.9. They show only small differences in the soil water characteristics, but significant ones for the hydraulic conductivity function.

The forecast during time period C (analogous to the standard EnKF) is shown in Fig. 5.10. The performance is acceptable, but worse than the standard EnKF (Fig. 5.6). This is exactly what is expected. The standard EnKF incorporates errors in the dynamics partly into the parameters, e.g., by estimating a too-large hydraulic conductivity, which can represent preferential flow up to a point. By introducing the closed-eye period, these errors are not incorporated into the parameters any more. The parameters are thus believed to be closer to the believed true material properties. Obviously, however, these parameters fail to describe rain events that lead to hydraulic non-equilibrium.

Guiding the states through the closed-eye period is a challenge. A representation of the dynamics' uncertainty would be required to estimate optimal states. I did not do this. The covariance inflation (chapter 4) reduces the issue by increasing the ensemble spread when measurements cannot be explained by combined measurement and ensemble uncertainty (Fig. 5.11). It was designed to follow rapid changes and is able to adjust the inflation factor fast to larger values during the closed-eye period. Still, it cannot solve the problem completely, since it is based on the correlations in the ensemble. These correlations are not necessarily valid any more, when a major, spatially structured uncertainty is not represented. In cases with stronger rain (and stronger non-equilibrium) and larger deviations of representation and measurements, a description of the dynamics uncertainties could possibly become mandatory.

5.4.4 Prediction capabilities

I investigate the predictive capabilities of the standard EnKF and closed-eye EnKF during the combined time period of B and C as well as time period D. As the closed-eye EnKF added another 10 iterations for the estimation, I compare it to standard EnKF results with additional 10 iterations as well.

During time period B the total amount of rain was 23.2 mm with a maximal flux of 2.5 mm in 10 min (compared to a total of 18.2 mm with a maximal flux of 0.7 mm in 10 min for time period C). As I already assume local non-equilibrium during the rain event in time period C, I expect an even stronger effect during time period B.

The forecast results for time period B and C for soil parameters and Miller scaling parameters from the standard EnKF and closed-eye EnKF are depicted in Fig. 5.12a and b (there is no improved estimation of the upper boundary condition during time period B and I did not use the improved boundary condition from time period C). I performed a spin-up with an EnKF with state estimation during time period A to achieve a good initial condition. Neither standard EnKF nor closed-eye EnKF is able to predict the water contents during the rain event in time period B in detail. However,

(a) Standard EnKF

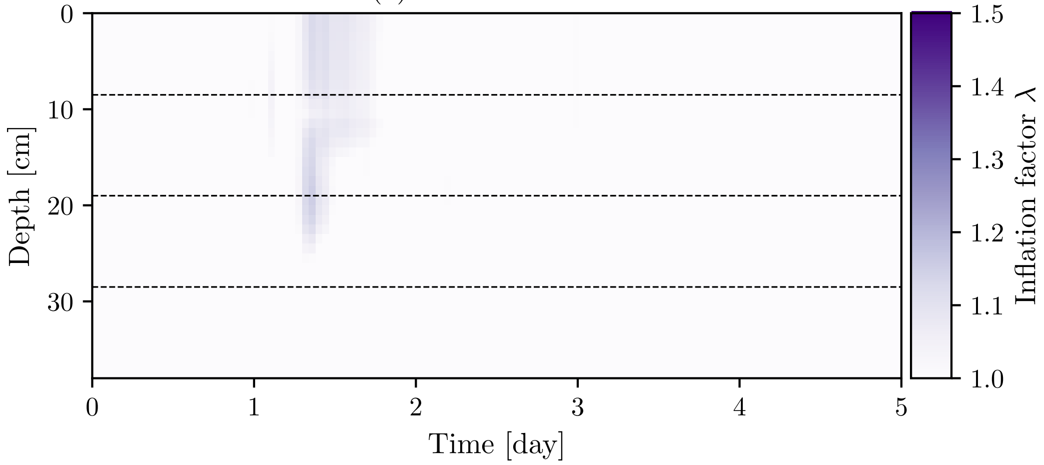

(b) Closed-eye EnKF

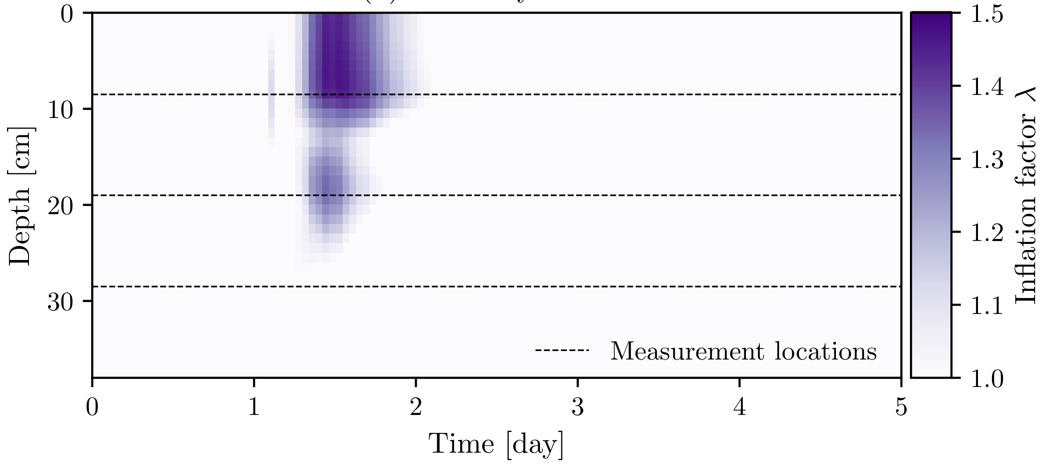

Figure 5.11: Inflation factor λ in the first layer during the last iteration of the standard EnKF and closed-eye EnKF. The covariance inflation increases the inflation factor around a measurement location when the deviations due to the infiltration reach the corresponding TDR. The deviations and consequently the inflation are stronger for the closed-eye EnKF, as the preferential flow is not incorporated into the parameters any more.

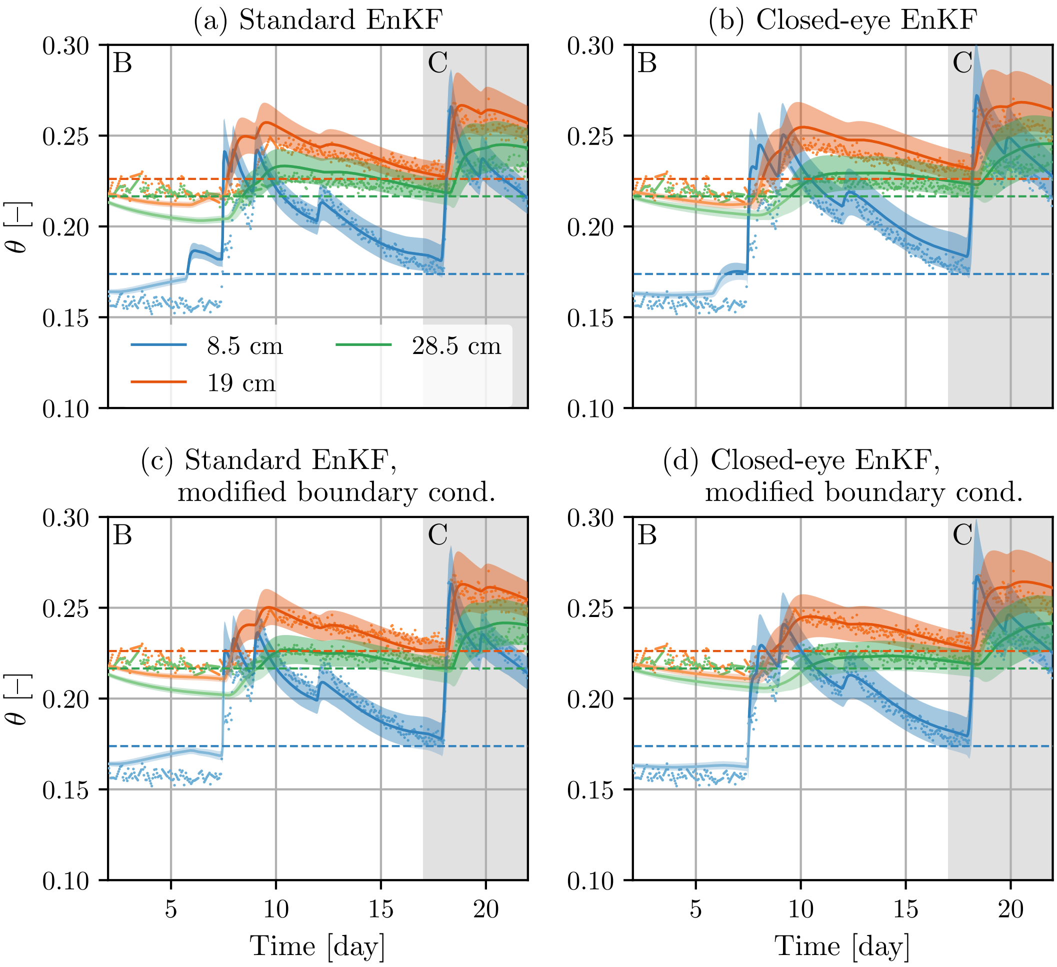

Figure 5.12: Forecast at the measurement positions of the first layer during time period B and C for the measurement based boundary condition **(a, b)** as well as a modified boundary condition **(c, d)**, where a rainfall on day 6 is removed, since it is not observed in the measurements. The solid lines show mean and standard deviation of a total of 100 different forecasts, with soil parameters and Miller scaling parameters sampled from the distributions estimated with the standard EnKF **(a, c)** and closed-eye EnKF **(b, d)**. The dots show the measurements, the dashed line the lowest water content measured during time period C, indicating the lower limit of the water content range, for which the parameters are deemed valid.

the standard EnKF describes the rain event in time period C better. The closed-eye EnKF is not able to predict the water contents during rain events as, for both, local non-equilibrium is expected, which is not incorporated into the parameter estimation. For the standard EnKF only the rain event from time period C is partly incorporated into the parameters and it predicts this rain event better. However, it fails to predict the stronger rain event in time period B showing that the local non-equilibrium in different rain events affects the dynamics differently. Hence, their effects should not be incorporated into parameters, but rather considered separately. The uncertainties are large for both EnKFs. The reason for this is the large uncertainty in the boundary conditions.

Both predictions, with the standard EnKF and closed-eye EnKF, show an increase in the water content for the topmost measurement location after a rainfall on day 6. This increase is not observed in the actual water content measurements. It is an indication, that the assumption of constant parameters is actually violated at this time. A possible explanation is the formation of a surface crust at the bare surface during the previous dry period. Such a crust can lead to surface runoff and prevent infiltration. To investigate a possible effect on the predictive capabilities, I perform another forecast for time period B and C, where this rainfall is removed from the boundary condition (Fig. 5.12c and d). The altered boundary condition changes the predictions quantitatively and the constant water content after the rainfall on day 6 is described better, especially by the closed-eye EnKF. However, the water content is below the observed water contents in time period C. Consequently, the estimated, heuristic material properties cannot be expected to hold in this range. The qualitative statements about the predictive capabilities for the rain events, found in Fig. 5.12a and b, are not altered through the modified boundary condition, though.

I emphasize that the standard EnKF excels if the goal is to guide some partly flawed representation with a stream of data. However, if the additional goal to estimate objective parameters for the representation within its range of applicability, then the closed-eye EnKF must be used, at the cost of a lower heuristic performance.

The forecast during the dry time period D is depicted in Fig. 5.13a and b. Here, I used the final state of the last iteration in the standard EnKF and closed-eye EnKF estimation as the initial condition. In the observed water content range both perform well, but the closed-eye EnKF performs better than the standard EnKF. This is the result that I expected. The closed-eye EnKF was able to estimate the believed true material properties in the observed water content range and can make predictions in this range as long as the basic assumptions of the Richards equation are met.

Both EnKFs can describe the topmost TDR better than the lower TDRs. This is expected as well, since the first TDR measures the strongest dynamics and hence dominates the parameter estimation. The small deviations in the other TDR sensors show that the assumption of Miller similarity, including the linear interpolation in between, is capable of improving the representation. It cannot represent heterogeneity completely, however.

Below the observed soil water content I do not expect predictive capabilities, since

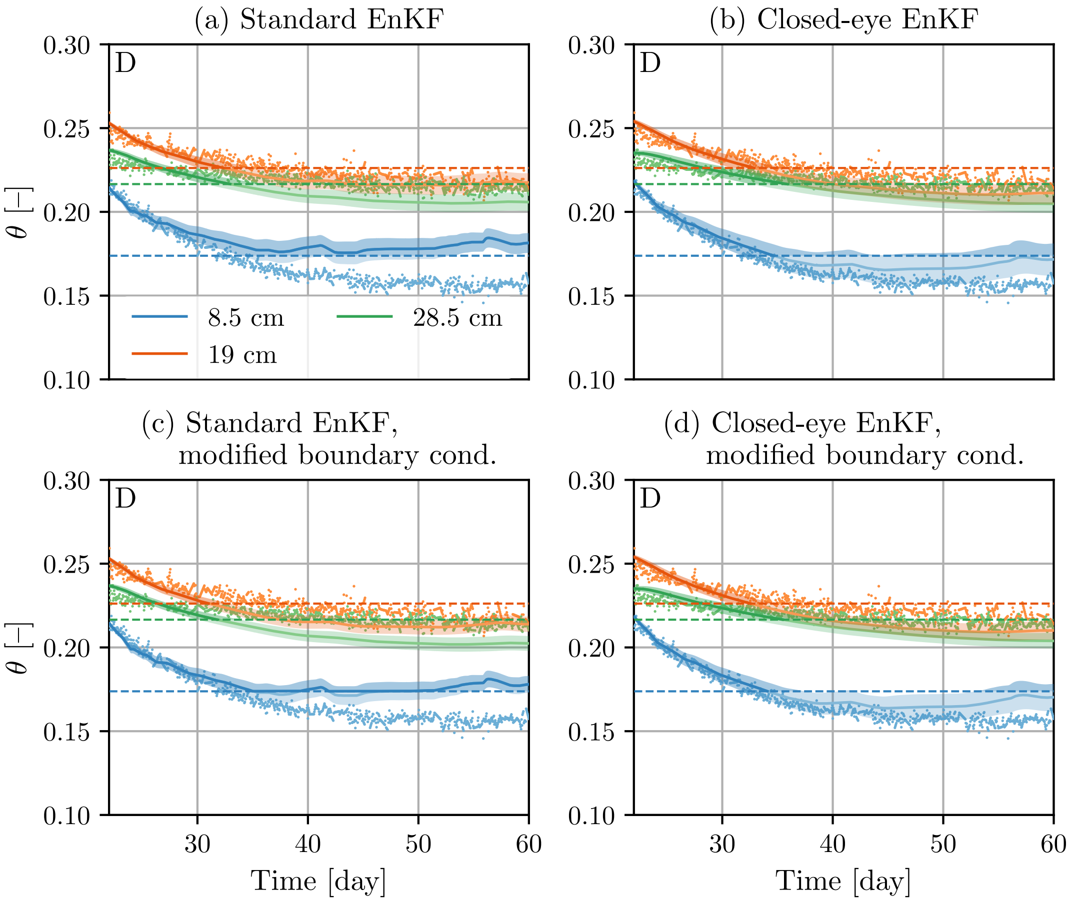

Figure 5.13: Forecast at the measurement positions of the first layer during time period B and C for the measurement based boundary condition **(a, b)** as well as a modified boundary condition **(c, d)**, where a single scaling factor is estimated for the evaporation. The solid lines show mean and standard deviation of a total of 100 different forecasts, with soil parameters and Miller scaling parameters sampled from the distributions estimated with the standard EnKF **(a, c)** and closed-eye EnKF **(b, d)**. The dots show the measurements, the dashed line the lowest water content measured during time period C, indicating the lower limit of the water content range, for which the parameters are deemed valid.

the material properties are heuristic and hence cannot be applied outside of the calibrated range. Nevertheless, the closed-eye EnKF does describe the topmost TDR acceptably. Again, there are deviations in the two lower TDR sensors, this time even stronger. Again, I attribute this to the limited description of the heterogeneity with Miller scaling.

I investigate the possibility of improving the results by estimating a single multiplicative factor to the uncertain evaporation in (Fig. 5.13c and d). This factor improves the estimation of the topmost TDR towards later times, but does not change the qualitative results above.

5.5 Summary and discussion

In this chapter, I improved the representation of soil water movement in a 1-D soil profile at the Grenzhof test site close to Heidelberg, Germany with an EnKF based on water content measurements from TDR probes.

I assessed key uncertainties of this specific representation. These are initial condition, soil hydraulic parameters, Miller scaling factors (describing small-scale heterogeneity), upper boundary condition, and the local equilibrium assumption by the Richards equation. These are accounted for in the process. Other components are deemed to be of lesser importance and are neglected. The most noteworthy neglected uncertainties are hysteresis, violations of the 1-D assumption, and measurement biases, which might affect the results.

A three-stage approach enabled the direct representation and estimation of all key uncertainties, except for errors caused by the local hydraulic equilibrium assumption. These intermittent errors were handled by introducing a closed-eye period. Through an iterative approach within each stage the estimation could be performed on a single rain event.

The first stage improves the prior. In the specific situation this is the initial water content distribution and Miller scaling factors. A good prior for the Miller scaling proved particularly beneficial, because during phases without dynamics, water content distributions generated by heterogeneity cannot be distinguished from low hydraulic conductivities.

The second stage iteratively applies a standard EnKF with an augmented state to improve the representation. This augmented state consists of soil water contents, soil hydraulic parameters, Miller scaling factors, and the upper boundary condition. This approach partly incorporates possible errors in the dynamics into the augmented state components. Due to the iterative approach, an intermittent violation the local equilibrium assumption in the dynamics can be detected from fluctuations of parameters which are assumed constant: during later iterations, the variations of the parameters within an iteration are larger than the change from initial to final value. The changes in the direction of the parameter update determine the closed-eye period.

The third stage applies a closed-eye EnKF that only estimates the full augmented states outside of the closed-eye period, when and where I assume the dynamics to be correctly represented. Within the period, I "close an eye" and do not estimate the previously varying parameters. In this way, the state is guided through this ill-represented phase and the full estimation is picked up afterwards again.

The study shows that assuming diagnostic soil layers to be homogeneous is not sufficient to represent heterogeneity. I was forced to also assume small-scale heterogeneity by observations of consistently higher water contents at probes that are located higher up within a soil layer. This emphasizes the role of heterogeneity, which must be considered more extensively in studies that rely on local measurements like the used TDR measurements.

The simplified representation of heterogeneity by estimating Miller scaling factors at measurement locations and interpolation between them was able to capture the main features in this work. Miller scaling is not capable of representing the heterogeneity completely, however. Predictions for the first layer show that measurements from the topmost TDR can be predicted better than the measurements of the second and third TDR probes. I attribute this to limitations of the Miller scaling. The parameter estimation is primarily influenced by the topmost TDR, where the largest water content changes occur. Describing the other measurements within the same layer with the same parameter set scaled by the Miller factor cannot fully describe the material properties.

The iterative standard EnKF successfully estimated soil parameters, Miller scaling parameters and upper boundary condition. It was capable of predicting the rain event that was used for its calibration well. However, it fails at the prediction of a different rain event. The reason is the violation of the local equilibrium assumption by the Richards equation during strong rain events. Non-represented errors are incorporated into the parameters. Since these errors are different for different rain events (with different strengths and different local non-equilibrium), they cannot be predicted.

The closed-eye EnKF prevents the incorporation of the model structural errors in the parameters and is a generally applicable concept. In the presented study, it yields better predictions during periods when the underlying assumptions are fulfilled: the drying period after a rain event when there is local equilibrium, showing the strength of the Richards equation there. As a consequence, however, its predictions are worse during rain events, that violate the local equilibrium assumption.

During the closed-eye phase, a description of these uncertainties caused by the non-equilibrium is desirable to be able to optimally guide the states through this phase. In the presented case, the method performed well without such a description, as the errors were small enough to be compensated by the covariance inflation.

The approach is capable of finding parameters closer to the believed true material properties of the soil than a standard EnKF. Predictions during rain events would require an additional representation of the fast dynamics during the event, though. Still, the approach shows a way to limit the incorporation of errors into parameters and is one step towards the goal of knowledge fusion.

6 | Summary and outlook

Soil water movement is a key process in several provisioning and regulating ecosystem services. The representation of soil water movement exhibits uncertainties in all model components. Soil hydraulic parameters describing the material properties in the subscale physics are considered to have the largest uncertainties. Furthermore, e.g., the violation of the local equilibrium assumption of the Richards equation, hysteresis, or unrepresented heterogeneity cause spatially and temporally varying model errors, which are difficult to describe. Nevertheless, information about each model component is available. This calls for knowledge fusion, the consistent aggregation of all available information pertinent to some observed reality.

Data assimilation methods combine information from models and measurements into an improved representation. They can – at least in principle – account for all uncertainties, but require a quantitative description of these uncertainties. Data assimilation methods are designed for state estimation, but have been extended to estimate further components, like parameters through an augmented state. A popular and powerful data assimilation method is the ensemble Kalman filter (EnKF).

Unrepresented model errors and a limited ensemble size can cause filter inbreeding, which deteriorates the performance of the EnKF. Inflation methods can compensate the unrepresented errors and prevent filter inbreeding. In this work, I proposed a spatiotemporally adaptive inflation method, specifically designed for soil hydrology. The inflation method is based on a Kalman filter acting within the EnKF. The method is capable of rapid adjustments of inflation factors, treating each augmented state dimension individually. This rapid adjustment is required due to temporally varying model errors.

The use of the inflation method was demonstrated in combination with a damping factor on a synthetic hydrologic example. The inflation method proved to be stable in combination with parameter estimation. The performance of the estimation improved and parameter uncertainty remained consistent. The method requires that model errors can be represented through the augmented state. The example demonstrated that the inflation even works for only weakly correlated parameters. I expect the inflation method to generally improve data assimilation with the EnKF and to thus, lead to better state and parameter estimations in soil hydrology.

With the goal of knowledge fusion, the EnKF was applied to a real world example.

I assessed the key uncertainties for the specific hydraulic situation of a 1-D soil profile with TDR-measured water contents. These key uncertainties are: initial condition, soil hydraulic parameters, small-scale heterogeneity, upper boundary condition, and the local equilibrium assumption by the Richards equation.

The EnKF with an augmented state was employed in three stages to directly represent and estimate all key uncertainties, except for the intermittent violation of the local equilibrium assumption, which was bridged by introducing a closed-eye period. First, prior uncertainties of initial condition and small-scale heterogeneity were reduced. Second, with a standard EnKF, water content states, soil hydraulic parameters, small-scale heterogeneity and upper boundary condition were estimated based on the TDR measurements during a single rain event. This was possible due to an iterative approach within each stage. Based on the development of soil hydraulic parameters during the estimation, times when the local equilibrium assumption did not hold could be identified. Third, a closed-eye period was introduced to bridge these times. The EnKF guides the water content states through this phase. The full estimation is only performed outside of the closed-eye period.

Introducing the closed-eye period ensured constant parameters, suggesting that they resemble the believed true material properties. This improves predictions during periods when the local equilibrium assumption is met, but consequently worsens predictions when the assumption is violated. A description of the dynamics during local non-equilibrium phases remains an open challenge.

The situation of partial knowledge about each component in a representation is typical in geosciences. I expect that the presented approach to use data assimilation methods with the goal of knowledge fusion can be transferred to other representations, for example a more complete description of interlinked processes in soils. However, I also expect the closed-eye period to become predominant when underlying assumptions are decreasingly met due to increasing complexity of the described processes. With limited training data availability as a major challenge, machine learning could present a possibility to improve the closed-eye period through: (i) identification of the closed-eye period, (ii) an improved estimate of the uncertainties and (iii) eventually the prediction of the response during the closed-eye period.

A | Derivations and calculations

A.1 Analysis equations in the Kalman filter

This section shows the calculation to reach the analysis equations for the Kalman filter in Sect. 3.2:

$$
\begin{aligned}
p(\boldsymbol{u}|\boldsymbol{d}) &\propto \exp\left[-\frac{1}{2}\left[\boldsymbol{u}-\boldsymbol{u}_\mathrm{f}\right]^T \mathbf{P}_\mathrm{f}^{-1}\left[\boldsymbol{u}-\boldsymbol{u}_\mathrm{f}\right]-\frac{1}{2}\left[\boldsymbol{d}-\mathbf{H}\boldsymbol{u}\right]^T \mathbf{R}^{-1}\left[\boldsymbol{d}-\mathbf{H}\boldsymbol{u}\right]\right] && \text{(A.1)}\\
&\propto \exp\left[-\frac{1}{2}\left[\boldsymbol{u}-\boldsymbol{u}_\mathrm{a}\right]^T \mathbf{P}_\mathrm{a}^{-1}\left[\boldsymbol{u}-\boldsymbol{u}_\mathrm{a}\right]\right], && \text{(A.2)}
\end{aligned}
$$

with

$$
\begin{aligned}
\boldsymbol{u}_\mathrm{a} &= \boldsymbol{u}_\mathrm{f} + \mathbf{K}\left[\boldsymbol{d}-\mathbf{H}\boldsymbol{u}_\mathrm{f}\right], && \text{(A.3)}\\
\mathbf{P}_\mathrm{a} &= \left[\mathbf{1}-\mathbf{K}\mathbf{H}\right]\mathbf{P}_\mathrm{f}, && \text{(A.4)}
\end{aligned}
$$

and

$$
\mathbf{K} = \mathbf{P}_\mathrm{f}\mathbf{H}^T\left[\mathbf{H}\mathbf{P}_\mathrm{f}\mathbf{H}^T+\mathbf{R}\right]^{-1}. \tag{A.5}
$$

To show the step from Eq. (A.1) to Eq. (A.2) some preparatory steps are useful. First, the Kalman gain (Eq. A.5) is rephrased:

$$
\begin{aligned}
\mathbf{K} &= \mathbf{P}_\mathrm{f}\mathbf{H}^T\left[\mathbf{H}\mathbf{P}_\mathrm{f}\mathbf{H}^T+\mathbf{R}\right]^{-1}\\
&= \left[\mathbf{P}_\mathrm{f}^{-1}+\mathbf{H}^T\mathbf{R}^{-1}\mathbf{H}\right]^{-1}\left[\mathbf{P}_\mathrm{f}^{-1}+\mathbf{H}^T\mathbf{R}^{-1}\mathbf{H}\right]\mathbf{P}_\mathrm{f}\mathbf{H}^T\left[\mathbf{H}\mathbf{P}_\mathrm{f}\mathbf{H}^T+\mathbf{R}\right]^{-1}\\
&= \left[\mathbf{P}_\mathrm{f}^{-1}+\mathbf{H}^T\mathbf{R}^{-1}\mathbf{H}\right]^{-1}\left[\mathbf{H}^T\mathbf{R}^{-1}\mathbf{H}\mathbf{P}_\mathrm{f}\mathbf{H}^T+\mathbf{H}^T\mathbf{R}^{-1}\mathbf{R}\right]\left[\mathbf{H}\mathbf{P}_\mathrm{f}\mathbf{H}^T+\mathbf{R}\right]^{-1}\\
&= \left[\mathbf{P}_\mathrm{f}^{-1}+\mathbf{H}^T\mathbf{R}^{-1}\mathbf{H}\right]^{-1}\mathbf{H}^T\mathbf{R}^{-1}. && \text{(A.6)}
\end{aligned}
$$

The analysis error covariance matrix (Eq. A.4) is rephrased as well:

$$
\begin{aligned}
\mathbf{P}_\mathrm{a} &= \left[\mathbf{1}-\mathbf{K}\mathbf{H}\right]\mathbf{P}_\mathrm{f}\\
&\overset{\text{(A.6)}}{=} \mathbf{P}_\mathrm{f}-\left[\mathbf{P}_\mathrm{f}^{-1}+\mathbf{H}^T\mathbf{R}^{-1}\mathbf{H}\right]^{-1}\mathbf{H}^T\mathbf{R}^{-1}\mathbf{H}\mathbf{P}_\mathrm{f}\\
&= \left[\mathbf{P}_\mathrm{f}^{-1}+\mathbf{H}^T\mathbf{R}^{-1}\mathbf{H}\right]^{-1}\left[\left[\mathbf{P}_\mathrm{f}^{-1}+\mathbf{H}^T\mathbf{R}^{-1}\mathbf{H}\right]\mathbf{P}_\mathrm{f}-\mathbf{H}^T\mathbf{R}^{-1}\mathbf{H}\mathbf{P}_\mathrm{f}\right]\\
&= \left[\mathbf{P}_\mathrm{f}^{-1}+\mathbf{H}^T\mathbf{R}^{-1}\mathbf{H}\right]^{-1}. && \text{(A.7)}
\end{aligned}
$$

Inserting Eq. (A.7) into Eq. (A.6) yields,

$$\mathbf{K} = \mathbf{P}_\mathrm{a}\mathbf{H}^T\mathbf{R}^{-1}\,. \tag{A.8}$$

Note that, since $\mathbf{P}_\mathrm{a}$ is symmetric, $\mathbf{K}^T = \mathbf{R}^{-1}\mathbf{H}\mathbf{P}_\mathrm{a}$.
In a next preparation step, $\boldsymbol{u}_\mathrm{f}\mathbf{P}_\mathrm{f}^{-1} + \boldsymbol{d}^T\mathbf{R}^{-1}\mathbf{H}$ is expressed with $\boldsymbol{u}_\mathrm{a}$ and $\mathbf{P}_\mathrm{a}$:

$$\begin{aligned}
\boldsymbol{u}_\mathrm{f}\mathbf{P}_\mathrm{f}^{-1} + \boldsymbol{d}^T\mathbf{R}^{-1}\mathbf{H} &= \boldsymbol{u}_\mathrm{f}\mathbf{P}_\mathrm{f}^{-1} + \boldsymbol{d}^T\mathbf{R}^{-1}\mathbf{H}\mathbf{P}_\mathrm{a}\mathbf{P}_\mathrm{a}^{-1}\\
&\overset{(A.8)}{=} \boldsymbol{u}_\mathrm{f}\mathbf{P}_\mathrm{f}^{-1} + \boldsymbol{d}^T\mathbf{K}^T\mathbf{P}_\mathrm{a}^{-1}\\
&\overset{(A.7)}{=} \boldsymbol{u}_\mathrm{f}\mathbf{P}_\mathrm{f}^{-1} + \boldsymbol{d}^T\mathbf{K}^T\mathbf{P}_\mathrm{f}^{-1} + \boldsymbol{d}^T\mathbf{K}^T\mathbf{H}^T\mathbf{R}^{-1}\mathbf{H}\\
&= \boldsymbol{u}_\mathrm{f}\mathbf{P}_\mathrm{f}^{-1} + \boldsymbol{d}^T\mathbf{K}^T\mathbf{P}_\mathrm{f}^{-1} + \boldsymbol{d}^T\mathbf{K}^T\mathbf{H}^T\mathbf{R}^{-1}\mathbf{H} + \boldsymbol{u}_\mathrm{f}^T\mathbf{H}^T\left[\mathbf{R}^{-1}\mathbf{H} - \mathbf{R}^{-1}\mathbf{H}\mathbf{P}_\mathrm{a}\mathbf{P}_\mathrm{a}^{-1}\right]\\
&\overset{(A.8)}{=} \boldsymbol{u}_\mathrm{f}\mathbf{P}_\mathrm{f}^{-1} + \boldsymbol{d}^T\mathbf{K}^T\mathbf{P}_\mathrm{f}^{-1} + \boldsymbol{d}^T\mathbf{K}^T\mathbf{H}^T\mathbf{R}^{-1}\mathbf{H} + \boldsymbol{u}_\mathrm{f}^T\mathbf{H}^T\left[\mathbf{R}^{-1}\mathbf{H} - \mathbf{K}^T\mathbf{P}_\mathrm{a}^{-1}\right]\\
&\overset{(A.7)}{=} \boldsymbol{u}_\mathrm{f}\mathbf{P}_\mathrm{f}^{-1} + \boldsymbol{d}^T\mathbf{K}^T\mathbf{P}_\mathrm{f}^{-1} + \boldsymbol{d}^T\mathbf{K}^T\mathbf{H}^T\mathbf{R}^{-1}\mathbf{H} +\\
&\qquad \boldsymbol{u}_\mathrm{f}^T\mathbf{H}^T\mathbf{R}^{-1}\mathbf{H} + \boldsymbol{u}_\mathrm{f}^T\mathbf{H}^T\mathbf{K}^T\mathbf{P}_\mathrm{f}^{-1} + \boldsymbol{u}_\mathrm{f}^T\mathbf{H}^T\mathbf{K}^T\mathbf{H}^T\mathbf{R}^{-1}\mathbf{H}\\
&= \boldsymbol{u}_\mathrm{f}\mathbf{P}_\mathrm{f}^{-1} + \boldsymbol{u}_\mathrm{f}^T\mathbf{H}^T\mathbf{R}^{-1}\mathbf{H} + \left[\boldsymbol{d} - \boldsymbol{u}_\mathrm{f}\mathbf{H}\right]^T\mathbf{K}^T\mathbf{P}_\mathrm{f}^{-1} + \left[\boldsymbol{d} - \boldsymbol{u}_\mathrm{f}\mathbf{H}\right]^T\mathbf{K}^T\mathbf{H}^T\mathbf{R}^{-1}\mathbf{H}\\
&= \left[\boldsymbol{u}_\mathrm{f}^T + \left[\mathbf{K}\left[\boldsymbol{d} - \boldsymbol{u}_\mathrm{f}\mathbf{H}\right]\right]^T\right]\left[\mathbf{P}_\mathrm{f}^{-1} + \mathbf{H}^T\mathbf{R}^{-1}\mathbf{H}\right]\\
&\overset{(A.3)}{=} \boldsymbol{u}_\mathrm{a}^T\left[\mathbf{P}_\mathrm{f}^{-1} + \mathbf{H}^T\mathbf{R}^{-1}\mathbf{H}\right]\\
&\overset{(A.7)}{=} \boldsymbol{u}_\mathrm{a}^T\mathbf{P}_\mathrm{a}^{-1}\,.
\end{aligned} \tag{A.9}$$

We can now transform Eq. (A.1) to Eq. (A.2),

$$\begin{aligned}
p(\boldsymbol{u}|\boldsymbol{d}) &\propto \exp\left[-\frac{1}{2}\left[\boldsymbol{u} - \boldsymbol{u}_\mathrm{f}\right]^T\mathbf{P}_\mathrm{f}^{-1}\left[\boldsymbol{u} - \boldsymbol{u}_\mathrm{f}\right] - \frac{1}{2}\left[\boldsymbol{d} - \mathbf{H}\boldsymbol{u}\right]^T\mathbf{R}^{-1}\left[\boldsymbol{d} - \mathbf{H}\boldsymbol{u}\right]\right]\,,\\
&\qquad \text{with}\ \boldsymbol{u}^T\mathbf{P}_\mathrm{f}^{-1}\boldsymbol{u}_\mathrm{f} = \boldsymbol{u}_\mathrm{f}^T\mathbf{P}_\mathrm{f}^{-1}\boldsymbol{u}\\
&\propto \exp\left[-\frac{1}{2}\boldsymbol{u}^T\left[\mathbf{P}_\mathrm{f}^{-1} + \mathbf{H}^T\mathbf{R}^{-1}\mathbf{H}\right]\boldsymbol{u} + \left[\boldsymbol{u}_\mathrm{f}^T\mathbf{P}_\mathrm{f}^{-1} + \boldsymbol{d}^T\mathbf{R}^{-1}\mathbf{H}\right]\boldsymbol{u} - \right.\\
&\qquad\qquad \left.\frac{1}{2}\boldsymbol{u}_\mathrm{f}^T\mathbf{P}_\mathrm{f}^{-1}\boldsymbol{u}_\mathrm{f} - \frac{1}{2}\boldsymbol{d}^T\mathbf{R}^{-1}\boldsymbol{d}\right]\\
&\propto \exp\left[-\frac{1}{2}\boldsymbol{u}^T\left[\mathbf{P}_\mathrm{f}^{-1} + \mathbf{H}^T\mathbf{R}^{-1}\mathbf{H}\right]\boldsymbol{u} + \left[\boldsymbol{u}_\mathrm{f}^T\mathbf{P}_\mathrm{f}^{-1} + \boldsymbol{d}^T\mathbf{R}^{-1}\mathbf{H}\right]\boldsymbol{u} + \text{const}\right]\\
&\overset{(A.7)}{\propto} \exp\left[-\frac{1}{2}\boldsymbol{u}^T\mathbf{P}_\mathrm{a}\boldsymbol{u} + \left[\boldsymbol{u}_\mathrm{f}^T\mathbf{P}_\mathrm{f}^{-1} + \boldsymbol{d}^T\mathbf{R}^{-1}\mathbf{H}\right]\boldsymbol{u} + \text{const}\right]\\
&\overset{(A.9)}{\propto} \exp\left[-\frac{1}{2}\boldsymbol{u}^T\mathbf{P}_\mathrm{a}\boldsymbol{u} + \boldsymbol{u}_\mathrm{a}^T\mathbf{P}_\mathrm{a}^{-1}\boldsymbol{u} + \text{const}\right]\\
&\propto \exp\left[-\frac{1}{2}\boldsymbol{u}^T\mathbf{P}_\mathrm{a}\boldsymbol{u} + \boldsymbol{u}_\mathrm{a}^T\mathbf{P}_\mathrm{a}^{-1}\boldsymbol{u} - \frac{1}{2}\boldsymbol{u}_\mathrm{a}^T\mathbf{P}_\mathrm{a}^{-1}\boldsymbol{u}_\mathrm{a} + \text{const}\right]\\
&\propto \exp\left[-\frac{1}{2}\left[\boldsymbol{u} - \boldsymbol{u}_\mathrm{a}\right]^T\mathbf{P}_\mathrm{a}^{-1}\left[\boldsymbol{u} - \boldsymbol{u}_\mathrm{a}\right]\right]\,.
\end{aligned} \tag{A.10}$$

A.2 Jacobian matrix in the inflation method

This section briefly shows the derivation of the Jacobian matrix $\mathbf{H}_\lambda$ for the inflation developed in this work (Sect. 4.1.1). Again, the entrywise product is denoted by $\circ$ and the entrywise square root of $\boldsymbol{\lambda}$ by $\sqrt{\boldsymbol{\lambda}}$:

$$
\begin{aligned}
(\mathbf{H}_\lambda)_{ij} &= \frac{\partial}{\partial\left(\boldsymbol{\lambda}_\mathrm{f}\right)_j}\left(\boldsymbol{h}_\lambda(\boldsymbol{\lambda}_\mathrm{f})\right)_i \\
&= \frac{\partial}{\partial\left(\boldsymbol{\lambda}_\mathrm{f}\right)_j}\left[(\mathbf{R})_{ii} + \left(\mathbf{H}\left[\mathbf{P}_\mathrm{f}\circ\left[\sqrt{\boldsymbol{\lambda}_\mathrm{f}}\sqrt{\boldsymbol{\lambda}_\mathrm{f}}^T\right]\right]\mathbf{H}^T\right)_{ii}\right]^{\frac{1}{2}} \text{ , with } \mathbf{P}_\mathrm{f} \text{ symmetric} \\
&= \frac{\partial}{\partial\left(\boldsymbol{\lambda}_\mathrm{f}\right)_j}\left[(\mathbf{R})_{ii} + \sum_m\sum_k (\mathbf{H})_{im}(\mathbf{H})_{ik}(\mathbf{P}_\mathrm{f})_{km}\left[(\boldsymbol{\lambda}_\mathrm{f})_m\right]^{\frac{1}{2}}\left[(\boldsymbol{\lambda}_\mathrm{f})_k\right]^{\frac{1}{2}}\right]^{\frac{1}{2}} \\
&= \left[2\left(\boldsymbol{h}_\lambda(\boldsymbol{\lambda}_\mathrm{f})\right)_i\right]^{-1}\sum_m\sum_k (\mathbf{H})_{im}(\mathbf{H})_{ik}(\mathbf{P}_\mathrm{f})_{km}\frac{\partial}{\partial\left(\boldsymbol{\lambda}_\mathrm{f}\right)_j}\left[\left[(\boldsymbol{\lambda}_\mathrm{f})_m\right]^{\frac{1}{2}}\left[(\boldsymbol{\lambda}_\mathrm{f})_k\right]^{\frac{1}{2}}\right] \\
&= \left[2\left(\boldsymbol{h}_\lambda(\boldsymbol{\lambda}_\mathrm{f})\right)_i\right]^{-1}\sum_m\sum_k (\mathbf{H})_{im}(\mathbf{H})_{ik}(\mathbf{P}_\mathrm{f})_{km}\frac{1}{2}\left[\delta_{mj}\frac{\left[(\boldsymbol{\lambda}_\mathrm{f})_k\right]^{\frac{1}{2}}}{\left[(\boldsymbol{\lambda}_\mathrm{f})_m\right]^{\frac{1}{2}}} + \delta_{kj}\frac{\left[(\boldsymbol{\lambda}_\mathrm{f})_m\right]^{\frac{1}{2}}}{\left[(\boldsymbol{\lambda}_\mathrm{f})_k\right]^{\frac{1}{2}}}\right] \\
&= \left[2\left[(\boldsymbol{\lambda}_\mathrm{f})_j\right]^{\frac{1}{2}}\left(\boldsymbol{h}_\lambda(\boldsymbol{\lambda}_\mathrm{f})\right)_i\right]^{-1}\sum_m (\mathbf{H})_{ij}(\mathbf{H})_{im}(\mathbf{P}_\mathrm{f})_{jm}\left[(\boldsymbol{\lambda}_\mathrm{f})_m\right]^{\frac{1}{2}} \ .
\end{aligned}
\tag{A.11}
$$

Acknowledgments

First of all, I would like to thank my advisor, Prof. Dr. Kurt Roth. Thank you for your inspiration, for productive discussions and for always challenging my concepts. Thank you for your motivation and enthusiasm.

I would like to thank Prof. Dr. Peter Bastian, the co-advisor of my work, and Prof. Dr. Carsten Rother, who immediately agreed to be available as second referee.

My sincere thanks to my mentors Dr. Ole Klein and Dr. Ute Wollschläger for your support and guidance.

Many thanks to the whole TS-CCEES work group for inspiring debates and recreational afternoon breaks and to my office colleagues for the great atmosphere.

I also thank Angelika Gassama for your continuous effort at Grenzhof test site and for always being in for a chat.

Special thanks to Daniel Berg, Lisa Hantschel, Philipp Kreyenberg, Lukas Riedel, Megan Siefker, Jule Thome and Crystal Wang for your discussions and comments, especially when finishing this thesis.

Finally, I would like to thank my girlfriend Irene, my family, and my friends for supporting me, not only during this thesis, but throughout my whole life.

Bibliography of own publications

Parts of the results presented in this dissertation have already been published. The publications are listed below. I wrote these publications as first author and identical wording occurs in this work.

Bauser, H. H., S. Jaumann, D. Berg, and K. Roth, EnKF with closed-eye period – towards a consistent aggregation of information in soil hydrology, *Hydrology and Earth System Sciences, 20*(12), 4999–5014, doi:10.5194/hess-20-4999-2016, 2016.

Bauser, H. H., D. Berg, O. Klein, and K. Roth, Inflation method for ensemble Kalman filter in soil hydrology, *Hydrology and Earth System Sciences Discussions*, doi:10.5194/hess-2018-74, in review, 2018.

I participated as coauthor in the following publication. It is neither used nor cited in this dissertation.

Berg, D., H. H. Bauser, and K. Roth, Covariance resampling for particle filter – state and parameter estimation for soil hydrology, *Hydrology and Earth System Sciences Discussions*, in review, 2018.

References

Adhikari, K., and A. E. Hartemink, Linking soils to ecosystem services – a global review, *Geoderma*, *262*, 101–111, doi:10.1016/j.geoderma.2015.08.009, 2016.

Allen, R. G., L. S. Pereira, D. Raes, and M. Smith, Crop evapotranspiration: Guidelines for computing crop requirements, *FAO Irrigation and Drainage Paper No. 56, FAO – Food and Agriculture Organization of the United Nations, Rome, Italy*, 1998.

Anderson, J. L., An ensemble adjustment Kalman filter for data assimilation, *Monthly Weather Review*, *129*(12), 2884–2903, doi:10.1175/1520-0493(2001)129<2884:AEAKFF>2.0.CO;2, 2001.

Anderson, J. L., An adaptive covariance inflation error correction algorithm for ensemble filters, *Tellus A*, *59*(2), 210–224, doi:10.1111/j.1600-0870.2006.00216.x, 2007.

Anderson, J. L., Spatially and temporally varying adaptive covariance inflation for ensemble filters, *Tellus A*, *61*(1), 72–83, doi:10.1111/j.1600-0870.2008.00361.x, 2009.

Anderson, J. L., and S. L. Anderson, A Monte Carlo implementation of the nonlinear filtering problem to produce ensemble assimilations and forecasts, *Monthly Weather Review*, *127*(12), 2741–2758, doi:10.1175/1520-0493(1999)127<2741:AMCIOT>2.0.CO;2, 1999.

Baram, S., V. Couvreur, T. Harter, M. Read, P. H. Brown, M. Kandelous, D. R. Smart, and J. W. Hopmans, Estimating nitrate leaching to groundwater from orchards: Comparing crop nitrogen excess, deep vadose zone data-driven estimates, and HYDRUS modeling, *Vadose Zone Journal*, *15*(11), doi:10.2136/vzj2016.07.0061, 2016.

Bateni, S. M., and D. Entekhabi, Surface heat flux estimation with the ensemble Kalman smoother: Joint estimation of state and parameters, *Water Resources Research*, *48*(8), doi:10.1029/2011WR011542, w08521, 2012.

Bauser, H. H., S. Jaumann, D. Berg, and K. Roth, EnKF with closed-eye period – towards a consistent aggregation of information in soil hydrology, *Hydrology and Earth System Sciences*, *20*(12), 4999–5014, doi:10.5194/hess-20-4999-2016, 2016.

Bauser, H. H., D. Berg, O. Klein, and K. Roth, Inflation method for ensemble Kalman filter in soil hydrology, *Hydrology and Earth System Sciences Discussions*, doi:10.5194/hess-2018-74, in review, 2018.

Berg, D., Particle filters for nonlinear data assimilation, Ph.D. thesis, Ruperto-Carola University Heidelberg, Germany, 2018.

Botto, A., E. Belluco, and M. Camporese, Multi-source data assimilation for physically-based hydrological modeling of an experimental hillslope, *Hydrology and Earth System Sciences Discussions*, *2018*, 1–26, doi:10.5194/hess-2018-18, 2018.

Brandhorst, N., D. Erdal, and I. Neuweiler, Soil moisture prediction with the ensemble Kalman filter: Handling uncertainty of soil hydraulic parameters, *Advances in Water Resources*, *110*, 360–370, doi:10.1016/j.advwatres.2017.10.022, 2017.

Burgers, G., P. J. van Leeuwen, and G. Evensen, Analysis scheme in the ensemble Kalman filter, *Monthly Weather Review*, *126*(6), 1719–1724, doi:10.1175/1520-0493(1998)126<1719:ASITEK>2.0.CO;2, 1998.

Camporese, M., C. Paniconi, M. Putti, and P. Salandin, Ensemble Kalman filter data assimilation for a process-based catchment scale model of surface and subsurface flow, *Water Resources Research*, *45*(10), doi:10.1029/2008WR007031, 2009.

Carsel, R. F., and R. S. Parrish, Developing joint probability distributions of soil water retention characteristics, *Water Resources Research*, *24*(5), 755–769, doi:10.1029/WR024i005p00755, 1988.

Chen, Y., and D. Zhang, Data assimilation for transient flow in geologic formations via ensemble Kalman filter, *Advances in Water Resources*, *29*(8), 1107–1122, doi:10.1016/j.advwatres.2005.09.007, 2006.

Crestani, E., M. Camporese, D. Baú, and P. Salandin, Ensemble Kalman filter versus ensemble smoother for assessing hydraulic conductivity via tracer test data assimilation, *Hydrology and Earth System Sciences*, *17*(4), 1517–1531, doi:10.5194/hess-17-1517-2013, 2013.

Crow, W. T., and E. Van Loon, Impact of incorrect model error assumptions on the sequential assimilation of remotely sensed surface soil moisture, *Journal of Hydrometeorology*, *7*(3), 421–432, doi:10.1175/JHM499.1, 2006.

De Lannoy, G. J. M., P. R. Houser, V. R. N. Pauwels, and N. E. C. Verhoest, State and bias estimation for soil moisture profiles by an ensemble Kalman filter: Effect of assimilation depth and frequency, *Water Resources Research*, *43*(6), doi:10.1029/2006WR005100, w06401, 2007.

De Lannoy, G. J. M., P. R. Houser, N. E. C. Verhoest, and V. R. N. Pauwels, Adaptive soil moisture profile filtering for horizontal information propagation in the independent column-based CLM2.0, *Journal of Hydrometeorology*, *10*(3), 766–779, doi:10.1175/2008JHM1037.1, 2009.

Desroziers, G., L. Berre, B. Chapnik, and P. Poli, Diagnosis of observation, background and analysis-error statistics in observation space, *Quarterly Journal of the Royal Meteorological Society*, *131*(613), 3385–3396, doi:10.1256/qj.05.108, 2005.

Dominati, E., M. Patterson, and A. Mackay, A framework for classifying and quantifying the natural capital and ecosystem services of soils, *Ecological Economics*, *69*(9), 1858–1868, doi:10.1016/j.ecolecon.2010.05.002, 2010.

Erdal, D., and O. A. Cirpka, Joint inference of groundwater-recharge and hydraulic-conductivity fields from head data using the ensemble Kalman filter, *Hydrology and Earth System Sciences*, *20*(1), 555–569, doi:10.5194/hess-20-555-2016, 2016.

Erdal, D., I. Neuweiler, and U. Wollschläger, Using a bias aware EnKF to account for unresolved structure in an unsaturated zone model, *Water Resources Research*, *50*(1), 132–147, doi:10.1002/2012WR013443, 2014.

Erdal, D., M. Rahman, and I. Neuweiler, The importance of state transformations when using the ensemble Kalman filter for unsaturated flow modeling: Dealing with strong nonlinearities, *Advances in Water Resources*, *86*(Part B), 354–365, doi:10.1016/j.advwatres.2015.09.008, 2015.

Evensen, G., Sequential data assimilation with a nonlinear quasi-geostrophic model using Monte Carlo methods to forecast error statistics, *Journal of Geophysical Research: Oceans*, *99*(C5), 10,143–10,162, doi:10.1029/94JC00572, 1994.

Evensen, G., The ensemble Kalman filter: theoretical formulation and practical implementation, *Ocean Dynamics*, *53*(4), 343–367, doi:10.1007/s10236-003-0036-9, 2003.

Foken, T., *Angewandte Meteorologie: Mikrometeorologische Methoden*, Springer, Berlin, Heidelberg, 2006.

Gaspari, G., and S. E. Cohn, Construction of correlation functions in two and three dimensions, *Quarterly Journal of the Royal Meteorological Society*, *125*(554), 723–757, doi:10.1002/qj.49712555417, 1999.

Hamill, T. M., J. S. Whitaker, and C. Snyder, Distance-dependent filtering of background error covariance estimates in an ensemble Kalman filter, *Monthly Weather Review*, *129*(11), 2776–2790, doi:10.1175/1520-0493(2001)129<2776:DDFOBE>2.0.CO;2, 2001.

Han, X., H.-J. Hendricks Franssen, C. Montzka, and H. Vereecken, Soil moisture and soil properties estimation in the Community Land Model with synthetic brightness temperature observations, *Water Resources Research*, *50*(7), 6081–6105, doi:10.1002/2013WR014586, 2014.

Hendricks Franssen, H. J., and W. Kinzelbach, Real-time groundwater flow modeling with the ensemble Kalman filter: Joint estimation of states and parameters and the filter inbreeding problem, *Water Resources Research*, *44*(9), doi:10.1029/2007WR006505, w09408, 2008.

Hopmans, J. W., J. Šimůnek, N. Romano, and W. Durner, Simultaneous determination of water transmission and retention properties. Inverse Methods, *in: Methods of Soil Analysis. Part 4. Physical Methods, edited by: Dane, J. H. and Topp, G. H., Soil Science Society of America Book Series No. 5.*, pp. 963–1008, 2002.

Houtekamer, P. L., and H. L. Mitchell, Data assimilation using an ensemble Kalman filter technique, *Monthly Weather Review*, *126*(3), 796–811, doi:10.1175/1520-0493(1998)126<0796:DAUAEK>2.0.CO;2, 1998.

Houtekamer, P. L., and H. L. Mitchell, A sequential ensemble Kalman filter for atmospheric data assimilation, *Monthly Weather Review*, *129*(1), 123–137, doi:10.1175/1520-0493(2001)129<0123:ASEKFF>2.0.CO;2, 2001.

Houtekamer, P. L., and F. Zhang, Review of the ensemble Kalman filter for atmospheric data assimilation, *Monthly Weather Review*, *144*(12), 4489–4532, doi:10.1175/MWR-D-15-0440.1, 2016.

Huber, E., H. J. Hendricks Franssen, H. P. Kaiser, and F. Stauffer, The role of prior model calibration on predictions with ensemble Kalman filter, *Groundwater*, *49*(6), 845–858, doi:10.1111/j.1745-6584.2010.00784.x, 2011.

Hunt, B. R., E. J. Kostelich, and I. Szunyogh, Efficient data assimilation for spatiotemporal chaos: A local ensemble transform Kalman filter, *Physica D: Nonlinear Phenomena*, *230*(1), 112–126, doi:10.1016/j.physd.2006.11.008, 2007.

Ippisch, O., H.-J. Vogel, and P. Bastian, Validity limits for the van Genuchten–Mualem model and implications for parameter estimation and numerical simulation, *Advances in Water Resources*, *29*(12), 1780–1789, doi:10.1016/j.advwatres.2005.12.011, 2006.

Jaumann, S., and K. Roth, Effect of unrepresented model errors on estimated soil hydraulic material properties, *Hydrology and Earth System Sciences*, *21*(9), 4301–4322, doi:10.5194/hess-21-4301-2017, 2017.

Kaatze, U., Complex permittivity of water as a function of frequency and temperature, *Journal of Chemical & Engineering Data*, *34*(4), 371–374, doi:10.1021/je00058a001, 1989.

Kurtz, W., H.-J. Hendricks Franssen, and H. Vereecken, Identification of time-variant river bed properties with the ensemble Kalman filter, *Water Resources Research*, *48*(10), doi:10.1029/2011WR011743, w10534, 2012.

Kurtz, W., H.-J. Hendricks Franssen, H.-P. Kaiser, and H. Vereecken, Joint assimilation of piezometric heads and groundwater temperatures for improved modeling of river-aquifer interactions, *Water Resources Research*, *50*(2), 1665–1688, doi:10.1002/2013WR014823, 2014.

Lawson, W. G., and J. A. Hansen, Implications of stochastic and deterministic filters as ensemble-based data assimilation methods in varying regimes of error growth, *Monthly Weather Review*, *132*(8), 1966–1981, doi:10.1175/1520-0493(2004)132<1966:IOSADF>2.0.CO;2, 2004.

Li, C., and L. Ren, Estimation of unsaturated soil hydraulic parameters using the ensemble Kalman filter, *Vadose Zone Journal*, *10*(4), 1205–1227, doi:10.2136/vzj2010.0159, 2011.

Li, H., E. Kalnay, and T. Miyoshi, Simultaneous estimation of covariance inflation and observation errors within an ensemble Kalman filter, *Quarterly Journal of the Royal Meteorological Society*, *135*(639), 523–533, doi:10.1002/qj.371, 2009.

Liu, Y., and H. V. Gupta, Uncertainty in hydrologic modeling: Toward an integrated data assimilation framework, *Water Resources Research*, *43*(7), doi:10.1029/2006WR005756, w07401, 2007.

Liu, Y., et al., Advancing data assimilation in operational hydrologic forecasting: progresses, challenges, and emerging opportunities, *Hydrology and Earth System Sciences*, *16*(10), 3863–3887, doi:10.5194/hess-16-3863-2012, 2012.

May, W., M. Rummukainen, F. Chéruy, S. Hagemann, and A. Meier, Contributions of soil moisture interactions to future precipitation changes in the GLACE-CMIP5 experiment, *Climate Dynamics*, *49*(5), 1681–1704, doi:10.1007/s00382-016-3408-9, 2017.

Moradkhani, H., S. Sorooshian, H. V. Gupta, and P. R. Houser, Dual state–parameter estimation of hydrological models using ensemble Kalman filter, *Advances in Water Resources*, *28*(2), 135–147, doi:10.1016/j.advwatres.2004.09.002, 2005.

Mualem, Y., A new model for predicting the hydraulic conductivity of unsaturated porous media, *Water Resources Research*, *12*(3), 513–522, doi:10.1029/WR012i003p00513, 1976.

Reichle, R. H., Data assimilation methods in the earth sciences, *Advances in Water Resources*, *31*(11), 1411–1418, doi:10.1016/j.advwatres.2008.01.001, 2008.

Reichle, R. H., D. B. McLaughlin, and D. Entekhabi, Hydrologic data assimilation with the ensemble Kalman filter, *Monthly Weather Review*, *130*(1), 103–114, doi:10.1175/1520-0493(2002)130<0103:HDAWTE>2.0.CO;2, 2002.

Robinson, D. A., S. B. Jones, J. M. Wraith, D. Or, and S. P. Friedman, A review of advances in dielectric and electrical conductivity measurement in soils using time domain reflectometry, *Vadose Zone Journal*, *2*, 444–475, doi:10.2136/vzj2003.4440, 2003.

Roth, K., Physics of terrestrial systems. Lecture notes, v0.2., *Institute of Environmental Physics, Heidelberg University, Germany.*, 2017.

Roth, K., R. Schulin, H. Flühler, and W. Attinger, Calibration of time domain reflectometry for water content measurement using a composite dielectric approach, *Water Resources Research*, *26*(10), 2267–2273, doi:10.1029/WR026i010p02267, 1990.

Schenk, G. U., Soil-atmosphere coupling: Looking from within the soil towards the surface, Ph.D. thesis, Ruperto-Carola University Heidelberg, Germany, 2011.

Shi, L., X. Song, J. Tong, Y. Zhu, and Q. Zhang, Impacts of different types of measurements on estimating unsaturated flow parameters, *Journal of Hydrology*, *524*, 549–561, doi:10.1016/j.jhydrol.2015.01.078, 2015.

Silber, A., Y. Israeli, I. Elingold, M. Levi, I. Levkovitch, D. Russo, and S. Assouline, Irrigation with desalinated water: A step toward increasing water saving and crop yields, *Water Resources Research*, *51*(1), 450–464, doi:10.1002/2014WR016398, 2015.

Song, X., L. Shi, M. Ye, J. Yang, and I. M. Navon, Numerical comparison of iterative ensemble Kalman filters for unsaturated flow inverse modeling, *Vadose Zone Journal*, *13*(2), doi:10.2136/vzj2013.05.0083, 2014.

Tippett, M. K., J. L. Anderson, C. H. Bishop, T. M. Hamill, and J. S. Whitaker, Ensemble square root filters, *Monthly Weather Review*, *131*(7), 1485–1490, doi:10.1175/1520-0493(2003)131<1485:ESRF>2.0.CO;2, 2003.

van Genuchten, M. T., A closed-form equation for predicting the hydraulic conductivity of unsaturated soils, *Soil Science Society of America Journal*, *44*(5), 892–898, doi:10.2136/sssaj1980.03615995004400050002x, 1980.

van Leeuwen, P. J., Comment on “Data assimilation using an ensemble Kalman filter technique”, *Monthly Weather Review*, *127*(6), 1374–1377, doi:10.1175/1520-0493(1999)127<1374:CODAUA>2.0.CO;2, 1999.

van Leeuwen, P. J., Compact course on data assimilation, Heidelberg Graduate School of Mathematical and Computational Methods for the Sciences, October 5-9, 2015.

van Leeuwen, P. J., Y. Cheng, and S. Reich, *Nonlinear data assimilation*, vol. 2, Springer, doi:10.1007/978-3-319-18347-3, 2015.

Vereecken, H., J. A. Huisman, H. J. Hendricks Franssen, N. Brüggemann, H. R. Bogena, S. Kollet, M. Javaux, J. van der Kruk, and J. Vanderborght, Soil hydrology: Recent methodological advances, challenges, and perspectives, *Water Resources Research*, *51*(4), 2616–2633, doi:10.1002/2014WR016852, 2015.

Vereecken, H., et al., Modeling soil processes: Review, key challenges, and new perspectives, *Vadose Zone Journal*, *15*(5), doi:10.2136/vzj2015.09.0131, 2016.

Vrugt, J. A., C. G. H. Diks, H. V. Gupta, W. Bouten, and J. M. Verstraten, Improved treatment of uncertainty in hydrologic modeling: Combining the strengths of global optimization and data assimilation, *Water Resources Research*, *41*(1), doi:10.1029/2004WR003059, w01017, 2005.

Vrugt, J. A., P. H. Stauffer, T. Wöhling, B. A. Robinson, and V. V. Vesselinov, Inverse modeling of subsurface flow and transport properties: A review with new developments, *Vadose Zone Journal*, *7*(2), 843–864, doi:10.2136/vzj2007.0078, 2008.

Wang, X., and C. H. Bishop, A comparison of breeding and ensemble transform Kalman filter ensemble forecast schemes, *Journal of the Atmospheric Sciences*, *60*(9), 1140–1158, doi:10.1175/1520-0469(2003)060<1140:ACOBAE>2.0.CO;2, 2003.

Welch, G., and G. Bishop, An introduction to the Kalman filter, *University of North Carolina at Chapel Hill, Department of Computer Science*, *TR 95-041*, 2006.

Whitaker, J. S., and T. M. Hamill, Ensemble data assimilation without perturbed observations, *Monthly Weather Review*, *130*(7), 1913–1924, doi:10.1175/1520-0493(2002)130<1913:EDAWPO>2.0.CO;2, 2002.

Whitaker, J. S., and T. M. Hamill, Evaluating methods to account for system errors in ensemble data assimilation, *Monthly Weather Review*, *140*(9), 3078–3089, doi:10.1175/MWR-D-11-00276.1, 2012.

Whitaker, J. S., T. M. Hamill, X. Wei, Y. Song, and Z. Toth, Ensemble data assimilation with the NCEP global forecast system, *Monthly Weather Review*, *136*(2), 463–482, doi:10.1175/2007MWR2018.1, 2008.

Wollschläger, U., T. Pfaff, and K. Roth, Field-scale apparent hydraulic parameterisation obtained from TDR time series and inverse modelling, *Hydrology and Earth System Sciences*, *13*(10), 1953–1966, doi:10.5194/hess-13-1953-2009, 2009.

Wu, C.-C., and S. A. Margulis, Feasibility of real-time soil state and flux characterization for wastewater reuse using an embedded sensor network data assimilation approach, *Journal of Hydrology*, *399*(3), 313–325, doi:10.1016/j.jhydrol.2011.01.011, 2011.

Wu, C.-C., and S. A. Margulis, Real-time soil moisture and salinity profile estimation using assimilation of embedded sensor datastreams, *Vadose Zone Journal*, *12*(1), doi:10.2136/vzj2011.0176, 2013.

Ying, Y., and F. Zhang, An adaptive covariance relaxation method for ensemble data assimilation, *Quarterly Journal of the Royal Meteorological Society*, *141*(692), 2898–2906, doi:10.1002/qj.2576, 2015.

Zhang, F., C. Snyder, and J. Sun, Impacts of initial estimate and observation availability on convective-scale data assimilation with an ensemble Kalman filter, *Monthly Weather Review*, *132*(5), 1238–1253, doi:10.1175/1520-0493(2004)132<1238:IOIEAO>2.0.CO;2, 2004.

Zhang, H., H.-J. Hendricks Franssen, X. Han, J. A. Vrugt, and H. Vereecken, State and parameter estimation of two land surface models using the ensemble Kalman filter and the particle filter, *Hydrology and Earth System Sciences*, *21*(9), 4927–4958, doi:10.5194/hess-21-4927-2017, 2017.